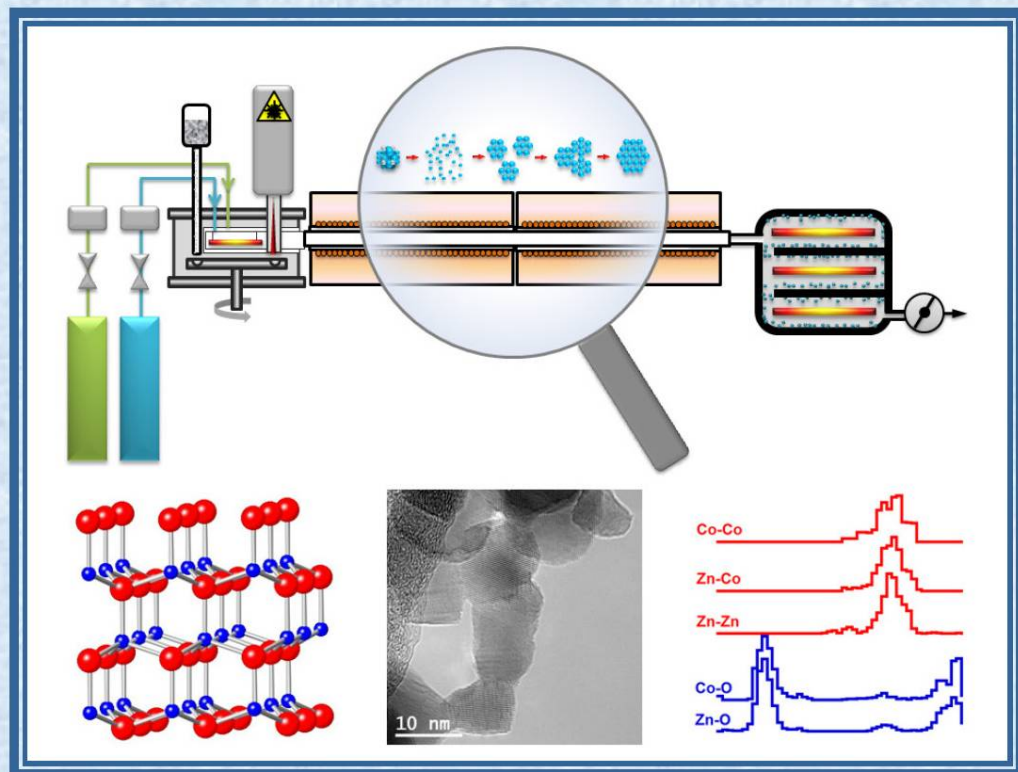


Ruzica Djenadic

Optimization of Chemical Vapor Synthesis of Oxide Nanoparticles



Cuvillier Verlag Göttingen
Internationaler wissenschaftlicher Fachverlag

Optimization of Chemical Vapor Synthesis of Oxide Nanoparticles

Von der Fakultät für Ingenieurwissenschaften, Abteilung Maschinenbau der
Universität Duisburg-Essen
zur Erlangung des akademischen Grades

DOKTOR-INGENIEURIN

genehmigte Dissertation

von

Ruzica Djenadic
aus
Sabac, Serbien

Referent: Univ.-Prof. Dr. rer. nat. Markus Winterer
Korreferent: Prof. Dr. Wayne Gladfelter
Tag der mündlichen Prüfung: 13.05.2011

Bibliografische Information der Deutschen Nationalbibliothek

Die Deutsche Nationalbibliothek verzeichnet diese Publikation in der Deutschen Nationalbibliografie; detaillierte bibliografische Daten sind im Internet über <http://dnb.d-nb.de> abrufbar.

1. Aufl. - Göttingen : Cuvillier, 2011

Zugl.: Duisburg-Essen, Univ., Diss., 2011

978-3-86955-778-6

© CUVILLIER VERLAG, Göttingen 2011

Nonnenstieg 8, 37075 Göttingen

Telefon: 0551-54724-0

Telefax: 0551-54724-21

www.cuvillier.de

Alle Rechte vorbehalten. Ohne ausdrückliche Genehmigung des Verlages ist es nicht gestattet, das Buch oder Teile daraus auf fotomechanischem Weg (Fotokopie, Mikrokopie) zu vervielfältigen.

1. Auflage, 2011

Gedruckt auf säurefreiem Papier

978-3-86955-778-6

*Dedicated to my parents, sister and brother
for their endless love and support*

Acknowledgments

One great and unforgettable journey came to an end and I would like to express my gratitude to many people for being (directly or indirectly) part of it:

- Prof. Markus Winterer, my thesis supervisor, for giving me the opportunity to work in his group and to explore the amazing world of nanoparticles. I am deeply grateful for his guidance, valuable advices, ‘crazy’ ideas and patience, without which this work would not be as it is now. I enjoyed working with him and I am glad that I had a chance to witness his great non-professional side on our group dinners, birthday parties, bike rides, museum tours, and so many other occasions;
- Prof. Vladimir V. Srdic from University of Novi Sad (Serbia) who was the one that gave me a chance to sail into science waters and to meet Prof. Markus Winterer. I am immensely thankful for all those years that he was with me. Without you this journey would never happened;
- Erdal Akyildiz for his warm welcome to Duisburg on September 26th at 2 p.m. (not a.m. as he thought at that time ☺), for being my interpreter and real estate agent, for taking care of all problems I encountered, for making my first technical drawings, but most of all for being a very good friend and making me to feel like I had a second brother. Thank you for everything listed and many other not listed things;
- Moazzam Ali for introducing me to Indian cuisine and teaching me how to use properly Indian spices, for chats and chit-chats (scientific and non-scientific) with coffee or tea prepared in the Indian way (1 tea bag of black tee, ½ cup of milk and ½ cup of sugar), and for his tolerance and friendship;
- Ulf Spengler, our lab engineer, for tolerating my numerous knocking on his door and solving many technical problems that I encountered in the lab, and tolerating or better to say accepting my frequent jokes;
- Frau Monika Lünsmann, our secretary, for being patient with my German and for all orders that she made. Liebe Frau Lünsmann Vielen Dank für Ihre Freundlichkeit, Chats und Verständnis;
- My colleagues Udo Dörfler, Devendraprakash Gautam, Christian Notthoff, Alexander Kompch, Martin Busch, Malte Heine, Yong Sang Cho, ‘my’ ladies Carolin Schilling and Alice Sandmann for the friendly atmosphere and for tolerating my ‘moments’;
- The students Farzin Tabary (Iran), Samer Suleiman (Germany), Cao Qing (China), Emmanuel Flores (USA) and Donna Deng (USA) for their help during the experiments.

- Dr. Klaus Attenkofer (ANL) for the EXAFS measurements, Dr. Marina Spasova, Dr. Zi-An Li, Dr. Ralf Theissmann, and Anoop Gupta for hours and hours on the TEM, Sonja Hartner for the UV-Vis spectroscopy, Andreas Gondorf for the FT-IR spectroscopy and Prof. Mehmet Acet for the SQUID measurements and for sharing his knowledge on magnetism with me;
- Herr Ulrich Visser from machine shop and his team of people without whom I would not have many parts of my experimental setup;
- My faraway friends Zeljkić, Marijanče and Nina, Tamarica, Srki, Ljubičica, Sneška, Maki, Agi, Sanjica, Maja and Nenad, Markos and Venia, Nikolina, Marija, Cuni and Prof. Ljubica Nikolić for their calls and e-mails which were my oasis. Thank you for staying so close even though you were so far;
- My “German” friends Seda (Turkey), Vadim and Zhenya (Russia), Miguel (Spain), Lieke (Holland), little Christina and Christina (Italy), Ning (Indonesia) and Özlem (Turkey) for sharing their time and parting with me. Special thanks to Seda for her small surprises, for listening, for friendship and being my second sister;
- And last but not least to my parents for teaching me important things in life, for their love that I didn’t lack all those years even being so far from them, to my brother for his silent love and kilograms and kilograms of my favorite Serbian sweets (krem bananice) and finally to my sister for her visits, for her wonderful words which brought me so many time to tears but knowing that my parents gave me the biggest treasure in my life. Najdraži moji hvala vam za sve.

Ruzica Djenadic
 Duisburg, May 2011

Contents

List of Abbreviations, Acronyms and Symbols	v
Abstract	xi
1 Introduction and Motivation	1
1.1 Review of Relevant Literature	2
1.1.1 Titanium Dioxide (TiO ₂) and Control of Particle Characteristics.....	2
1.1.2 Zinc Oxide (ZnO) and Control of Composition	3
2 Theoretical Background	5
2.1 Chemical Vapor Synthesis (CVS).....	5
2.2 Particle Formation and Growth (CVSSIN Model).....	6
2.3 Materials.....	10
2.3.1 Titanium Dioxide, TiO ₂	10
2.3.2 Zinc Oxide, ZnO.....	10
2.4 Particle Characteristics.....	11
2.4.1 Particle Agglomeration and Size Distribution	11
2.4.2 Magnetic Properties.....	14
3 Experimental Methodologies	17
3.1 Unit Operations of CVS	17
3.1.1 Precursor Delivery.....	17
3.1.2 Hot-Wall Reactors as Heat Sources.....	18
3.1.3 Particle Collection	21
3.2 Reactor Temperature Measurement	21
3.3 Synthesis of Nanoparticles	22
3.3.1 TiO ₂ Nanoparticles	22

3.3.1.1 The Influence of the Time-Temperature Profiles on Particle Characteristics	23
3.3.1.2 The Influence of the Particle Number Concentration on Width of the Particle Size Distribution	24
3.3.2 Co-doped and Co,Li-doped ZnO Nanoparticles	26
3.4 Particle Characterization	26
3.4.1 X-Ray Diffraction (XRD) and Rietveld Refinement	26
3.4.2 Low-Temperature Nitrogen Adsorption	29
3.4.3 Transmission Electron Microscopy (TEM)	30
3.4.4 Photon Correlation Spectroscopy (PCS)	30
3.4.5 Atomic Absorption Spectroscopy (AAS)	31
3.4.6 Ultraviolet-Visible Spectroscopy (UV-Vis)	31
3.4.7 X-Ray Absorption Spectroscopy (XANES and EXAFS)	32
3.4.8 Superconducting Quantum Interference Device (SQUID) Measurements	35
4 Results and Discussion	37
4.1 Particle Size and Degree of Agglomeration	37
4.1.1 Results of the CVSIN Model	37
4.1.2 The Experimental Results	44
4.1.2.1 The 'Flat' Time-Temperature Profiles	44
4.1.2.2 The 'Up' Time-Temperature Profiles	52
4.1.2.3 Comparison of Different Time-Temperature Profiles	53
4.1.3 Comparison of the CVSSIN Model with Experimental Data	55
4.1.4 Conclusion	59
4.2 Particle Size and Size Distribution by Pulsed Precursor Delivery	60
4.2.1 Influence of Laser Pulse Repetition Frequency	61
4.2.2 Influence of Laser Duty Cycle	63
4.2.3 Conclusion	66
4.3 Structure and Properties of Doped ZnO Nanoparticles	67
4.3.1 Chemical Composition	67

4.3.2 Crystal Structure	69
4.3.3 Local Structure	75
4.3.4 Magnetic Properties	81
4.3.5 Conclusion	88
5 Conclusions	89
6 References	91
7 Appendix	97

List of Abbreviations, Acronyms and Symbols

a	surface area of a single agglomerate particle (p. 8)
A	absorption multiplier (p. 27)
A	area covered by absorption of one gas molecule (p. 29)
a	lattice parameter (p. 75)
AAS	atomic absorption spectroscopy (p. 31)
a_s	surface area of a completely sintered particle (p. 8)
B	XRD peak background (p. 28)
BET	Brunauer-Emmett-Teller theory (p. 29)
$bk g_i$	background (polynomial) function (p. 27)
BMP	bound magnetic polaron (p. 3)
c	(molecular) particle velocity (p. 7)
c	particle concentration (p. 13)
C	Curie constant (p. 15)
C	BET constant (p. 29)
c	concentration of analyte element (p. 31)
c	lattice constant (p. 72)
c_0	initial precursor concentration (p. 9)
C_M	Curie constant per molecule (p. 81)
c_p	specific heat capacity of the gas at constant pressure (p. 9)
CVD	chemical vapor deposition (p. 5)
CVS	chemical vapor synthesis (p. vi)
CVSSIN	software for CVS process modeling (p. 6)
d	spacing between the lattice planes (p. 27)
d	crystallite diameter (p. 28)
D	diffusion coefficient (p. 31)
D_0	pre-exponential constant (p. 9)
d_0	initial particle diameter (p. 71)
D_a	axial dispersion coefficient (p. 13)
d_{BET}	particle size determined from BET specific surface area
d_c	collision diameter (p. 7)
DC	duty cycle (p. 24)
D_f	mass fractal dimension (p. 8)
d_g	geometric mean diameter (p. 28)
D_{gb}	grain boundary diffusion coefficient (p. 9)
d_h	hydrodynamic radius (p. 31)
d_n	number weighted particle size (p. 48)
D_p	particle diffusion coefficient (p. 7)

d_p	primary particle diameter (p. 7)
d_v	volume weighted particle size (p. 48)
E	energy (p. 22)
E	X-ray photon energy (p. 33)
E_0	absorption edge energy (p. 33)
E_D	activation enthalpy of diffusion (p. 9)
EXAFS	extended X-ray absorption fine structure (p. 32, p. 33)
f	frequency (p. 24)
FC	field-cooled (p. 35)
FEFF8	software for the ab initio computation of EXAFS spectra (p. 34)
f_j	atomic scattering factor (p. 27)
$f_i(k)$	backscattering amplitude (p. 33)
F_k	structure factor (p. 27)
$FT(R)$	Fourier transformation (p. 34)
F_{th}	thermophoretic force (p. 21)
g	transition parameter (p. 7)
$GofF$	goodness of fit (p. 28)
H	magnetic field strength molecular weight (p. 35)
\hbar	Planck's constant (p. 33)
h, k, l	Miller indices (p. 27)
I	current (p. 19)
I	XRD peak intensity (p. 28)
I	incoming light intensity (p. 31, p. 32)
I_0	absorbed/transmitted light intensity (p. 31, p. 32)
k	reaction constant (p. 7)
k	wave number of the photoelectron (p. 33)
k_0	pre-exponential factor (p. 7)
k_B	Boltzman constant (p. 7)
Kn	Knudsen number (p. 7)
L	diameter of the reactor tube (p. 9)
L	reactor length (p. 13)
l	length of the absorption path (p. 31)
l	Zn-O bond length (p. 75)
L_k	Lorentz-polarization (p. 27)
M	molecular weight (p. 29, p. 35)
m	mass of the solid material (p. 29)
m	electron mass (p. 33)
MAUD	software for Rietveld refinement of XRD data (p. 28)
n	integer (p. 27)
n	number of data points (p. 28)
N_0	initial particle number concentration (p. 71)
N_a	number density of agglomerates (p. 7)
N_A	Avogadro's constant (p. 29)
\dot{n}_{He}	molar flow of carrier gas (p. 18)
N_j	occupation factor of the j th atom (p. 27)

N_j	coordination number of the j th atom (p. 33)
NNN	next nearest neighbor (p. 83)
N_p	number density of precursor molecules (p. 7)
\dot{n}_{prec}	molar flow of precursor (p. 18)
$N_{surface}$	number of atoms at the particle surface (p. 72)
\dot{n}_{tot}	total molar flow of gases (p. 20)
Nu	Nusselt number (p. 9)
N_{volume}	number of atoms in the particle volume (p. 72)
p	pressure (p. 18)
P	period (p. 24)
p	number of free least squares parameters (p. 28)
p	equilibrium experimental pressure (p. 29)
P	probability (p. 83)
p_0	vapor pressure of the adsorbate gas (p. 29)
PCS	photon correlation spectroscopy (p. 30)
P_k	preferred orientation function (p. 27)
p_{prec}	precursor vapor pressure (p. 18)
Q	heat (p. 19)
R	electrical resistance (p. 19)
R	gas constant (p.
r	radius (p. 72)
R_{exp}	expected profile residual (p. 28)
R_j, R	distance to the neighboring atom (p. 33, 34)
RMC	Reverse Monte Carlo (p. 34)
R_{wp}	weighted profile residual (p. 28)
s	scale factor (p. 27)
SQUID	superconducting quantum interference device (p. 35)
S_s	specific surface area (p. 29)
S_s	specific surface area
T	temperature (p. 7)
t	time (p. 7)
T_C	Curie temperature (p. 15)
TEM	transmission electron microscopy (p. 30)
T_g	gas temperature (p. 9)
t_j	temperature (Debye-Waller) factor (p. 27)
TM	transition metal (p. 3)
T_N	Néel temperature (p. 16)
TTIP	titanium tetra-isopropoxide (p. 6)
T_w	wall (process) temperature
u	velocity (p. 13)
u	oxygen positional parameter in c -direction (p. 75)
UV-Vis	ultraviolet-visible spectroscopy (p. 31)
v	volume of a single agglomerate (p. 8)
V	reactor volume (p. 20)
v_p	volume of primary particle (p. 8)

V_{th}	velocity of thermophoresis (p. 219)
w	grain boundary (interface) width (p. 9)
W	adsorbed weight (p. 29)
w	mass of sample (p. 35)
w_i	wighting factor
W_m	monolayer weight (p. 29)
WSS	weighted sum of squares (p. 27)
x	sample thickness (p. 32)
x	nominal cobalt content (p. 67)
x_a	actual cobalt content (p. 67)
$xafsX$	software to analyze XAS spectra (p. 34)
XANES	X-ray absorption near-edge structure (p. 32, p. 33)
XAS	X-ray absorption spectroscopy (p. 32)
x_j, y_j, z_j	atom position parameters (p. 27)
x_p	cation percolation threshold (p. 3)
XRD	X-ray diffraction (p. 26)
Y_{ci}	calculated intensity at i^{th} step (p. 27)
Y_{oi}	observed intensity (p. 27)
ZFC	zero-field-cooled (p. 35)
∇T	temperature gradient (p. 21)
ΔH_{ads}	heat of adsorption (p. 29)
ΔH_{cond}	latent heat of condensation (p. 29)
ΔH_R	reaction enthalpy (p. 9)
σ	sintering constant (p. 9)
Ω	volume of diffusing species (p. 9)
γ	interfacial enthalpy (p. 9)
σ	variance (p. 13)
μ	magnetic moment (p. 14)
χ	magnetic susceptibility (p. 15)
η	gas viscosity (p. 21)
σ	Stefan-Boltzmann constant (p. 22)
ε	emissivity (p. 22)
ϕ	reflection profile function (p. 27)
ε	absorption coefficient (p. 31)
μ	absorption coefficient (p. 32)
λ	mean free path of photoelectron (p. 33)
σ	specific magnetization (p. 35)
χ	molar magnetic susceptibility (p. 35)
$\chi(k)$	EXAFS signal (p. 33)
μ_B	Bohr magneton (p. 81)
τ_c	collision time (p. 8)
μ_{eff}	effective (net) magnetic moment (p. 81)
σ_g	geometric standard deviation (p. 12)
$\delta_i(k)$	phase-shift (p. 33)

σ_j^2	disorder in the interatomic distance (p. 33)
μ_l	orbital moment (p. 14)
δ_p	polaron percolation threshold (p. 3)
ρ_p	particle density (p. 8)
τ_r	residence time (p. 20)
τ_s	sintering time (p. 8)
μ_s	spin moment (p. 14)

Abstract

The quality and application of nanostructured materials are strongly related to particle and powder characteristics. Powders of small particle size, narrow size distribution, low degree of agglomeration and high purity are typically required for the fabrication of solid nanocrystalline materials and the exploitation of size effects in applications. Chemical vapor synthesis (CVS) is a method for the generation of nanoparticles in the gas phase. Process parameters (temperature, pressure, residence time, precursor concentration, etc.) play an important role.

In this work it is shown for TiO_2 that the way in which energy is supplied to the reactor and the time-temperature history which the particles experience have substantial influence on the particle generation and powder characteristics. The degree of agglomeration can be decreased by using high process temperatures and high quenching rates. A novel method, pulsed precursor delivery using a laser flash evaporator, was developed to feed precursors into a CVS reactor. The degree of particle agglomeration can be significantly reduced by pulsed precursor delivery. The volatility of precursors used in CVS can limit the number of possible material systems which can be produced as well as their production rate. It is shown that these limitations can be overcome by the use of a laser flash evaporator, which enables the production of complex oxides such as Co-doped and Co, Li-doped ZnO. A high solubility of Co in ZnO, where Co is substituting Zn in the wurtzite lattice is achieved. This is the key requirement for the development of dilute magnetic semiconductors based on Co-doped ZnO.

1 Introduction and Motivation

Materials can be considered as ‘substances with properties that turn them into products, parts, devices or machines developed by mankind to fulfill physical, social, aesthetic and safety needs’ [Silva 1994]. Among the various classes of materials, metal oxides are the most common and most diverse material systems in terms of physical, chemical, and structural properties with applications as optical, magnetic, electronic, thermal, electrochemical, mechanical, and catalytic materials. Origin of this diversity is related to the variety of oxidation states, coordination number, symmetry, ligand-field stabilization of the metal ions, density, and stoichiometry of the oxide compounds [Vayssieres 2007]. Metal oxides exhibit insulating, semiconducting, conducting, or magnetic behavior.

Nanocrystalline oxide materials have significant technological advantages over traditional materials in terms of their properties due to size and interfacial effect. The control of a nanoparticle size, shape, composition and structure is necessary to ensure that the nanoparticles will meet the requirements specified by commercial applications. Consequently, existing synthesis and processing techniques are being continuously refined while at the same time novel methods are being developed. Many efforts are being made to synthesize nanocrystalline materials using a large number of methods based on solid, liquid or gas phase processes [Rodriguez and Fernandez-Garcia 2007]. Each technique has its own advantages and disadvantages. Gas phase processes allow the particle generation with unique combination of properties that in many cases cannot be obtained by other processes. In comparison to liquid phase methods, gas phase synthesis has the advantage that the particles are formed at high temperatures, which allows the formation of highly crystalline materials [Kodas and Hampden-Smith 1999] and particle contamination by byproducts is much lower. For the production of nanocrystalline materials from nanopowders produced by gas phase methods it is not only important to control the grain size but also, i.e. the particle morphology or agglomeration [Flagan and Lunden 1995]. The quality and application of nanostructured materials are strongly related to the particle and powder characteristics. Powders of small grain size, narrow size distribution, low degree of agglomeration and high purity are required for the fabrication of solid nanocrystalline materials and the exploitation of size effects in commercial applications.

The objective of this thesis is to optimize chemical vapor synthesis (CVS) for the production of high quality oxide particles (TiO_2 and ZnO) with controlled properties.

The first part of this thesis is focused on modeling of the CVS process to acquire insight into the particle formation and influence of time-temperature history

on particle characteristics, and to optimize the CVS process in order to obtain particles with low degree of agglomeration and high crystallinity. Additionally, it was studied how the particle number concentration has influence on the particle characteristics (size, degree of agglomeration and consequently width of particle size distribution). Titanium dioxide (TiO_2) was selected as a model material because it is widely experimentally and theoretically studied as an important material used in photocatalysis and dye-sensitized solar cells [O'Regan and Grätzel 1991] and detailed model description of the CVS process is feasible.

The second part of the thesis is focused on study of the nanoparticle structure (crystal and local) as one of the important factors that defines material property. Zinc oxide (ZnO) was used as a study system because it is very interesting non-magnetic semiconductor material which, according to the theoretical prediction, shows interesting magnetic properties upon zinc (Zn) substitution by cobalt (Co). The ability to precisely control the arrangements of dopant elements (here Co) and phase composition, is of great importance.

1.1 Review of Relevant Literature

1.1.1 Titanium Dioxide (TiO_2) and Control of Particle Characteristics

Titanium dioxide (TiO_2) is a semiconducting material used in a wide variety of technological applications as a photocatalyst, electrolyte in solar cells, gas sensor, white pigment, corrosion protective coating, optical coating, in memory devices, and in Li-based batteries [Chen and Mao 2007]. Because much experimental and theoretical information is available and the product of the CVS process is typically crystalline, consisting mostly of anatase, TiO_2 was chosen as a model material. This enables not only a detailed model description of the CVS process but also an extensive characterization of the as-synthesized particles.

Practical application of nanoparticles often involves the preparation of a colloidal suspension in order to deposit films. The microstructure of the resulting nanomaterial as well as its properties can be affected by the particle agglomeration [Maira et al. 2000]. Therefore, it is important to search for new ways or to improve already existing methods to obtain particles with a minimum degree of (hard) agglomeration.

The production of nanoparticles using flame synthesis is the gas phase method well theoretically and experimentally studied. In flame reactors the powder characteristics are mostly determined by the flame temperature and the particle residence time [Kammler et al. 2001]. The particle size, as well as the width of the particle size distribution, increases as the particles move up the flame. Coagulation becomes more pronounced at longer residence times [Tsantilis et al. 2002]. As a result, a distribution of time-temperature histories may be stored in the samples. Grass et al. [Grass et al. 2006] studied the evolution of hard- and soft-

agglomerates of TiO₂ particles made by gas phase and surface oxidation of titanium isopropoxide. They have found that particles with low degree of agglomeration or even non-agglomerated particles could be produced at low precursor feed, high maximum process temperature and at high cooling rates.

It has been shown that the width of particle size distribution has a strong influence on the sintering process of compacts. Studies by [Chappell et al. 1986, Ting and Lin 1995, e.g.] showed that the sintering ability (densification rate) of compacts decreases as the width of particle size distribution of the starting powder increases. For the liquid phase it has been shown that the droplet size distribution can be narrowed using an oscillating reactor [Pereira and Ni 2001] or segmented liquid flows [Jongen et al. 2003]. So far there are no reports on the influence of pulsed precursor flow in the gas phase on the particle size distribution.

1.1.2 Zinc Oxide (ZnO) and Control of Particle Composition

Zinc oxide (ZnO) is a semiconducting material with interesting optical, electrical (piezoelectric) and chemical (sensing) properties and is used in numerous applications [Schmidt-Mende and MacManus-Driscoll 2007] such as gas sensors, light emitting diodes, cantilevers, solar cells. Inspired by optimistic predictions, at first by Dietl [Dietl et al. 2000] later by Sato [Sato and Katayama-Yoshida 2001], extensive research effort have been performed by many groups on searching for room temperature ferromagnetism in transition metal (TM) doped ZnO. At first, the focus was only on films [Ueda et al. 2001], then the effort was directed toward the synthesis of nanocrystalline powders [Sharma et al. 2003, Lakshmi et al. 2009] with potential use in ferrofluids, opto-magneto-electronics, and biomedical applications. In many studies on ZnO doped with cobalt [Kim et al. 2007, Bouloude-nine et al. 2005, Chambers et al. 2006] or other TM elements [Jin et al. 2007, Kolesnik et al. 2004, Cong et al. 2006] contradictory results on magnetic properties have been reported. In the case of Co-doped ZnO paramagnetism [Martinez et al. 2005, Ney et al. 2008] or ferromagnetism at low [Yang et al. 2009], room [Lakshmi et al. 2009] or even high temperatures [Deka et al. 2004] was found. The ferromagnetism observed in several studies [Park et al. 2004, Norton et al. 2003, Blasco et al. 2006, Deka et al. 2006] had the origin in the second phases, but often the existence of second phases was not investigated [Behan et al. 2008]. The origin of the magnetic properties of TM-doped ZnO complex is still not well understood.

There are several concepts proposed to stabilize the ferromagnetism in ZnO. Table 1.1 gives an overview of these concepts. One proposal is based on bound magnetic polaron (BMP) [Coey et al. 2005] according to which ferromagnetism can be established only when the concentration of magnetic cations is lower than the percolation threshold in wurtzite structure ($x_p = 0.18$) and the concentration of polarons is higher than percolation threshold ($\delta_p = 0.0015$). Opposite to the BMP approach, several authors [Lee and Chang 2004, Sandratskii and Bruno 2006,

Nayak et al. 2008] reported that due to the short range nature of the ferromagnetic coupling, a heavy incorporation of dopant atoms is required to stabilize the ferromagnetic states. Codoping (simultaneous presence of two dopant elements) with acceptor and/or donor elements has also been proposed as a potential means to establish the ferromagnetic coupling of TM ions (“carrier mediated ferromagnetism”) [Sluiter et al. 2005, Gopal and Spaldin 2006]. Most recently, study on Mn-doped ZnO system, suggest that ferromagnetic ordering can be stabilized by presence of grain-boundaries and vacancies (“grain-boundary foam”) [Straumal et al. 2009A]. Experimentally, the most challenging approach is the substitutional incorporation of higher quantities of dopant atoms into the ZnO wurtzite lattice due to their thermodynamic solubility limit [Straumal et al. 2008]. Not only is a high quantity of dopant atoms required, but also their homogeneous distribution on Zn (substitutional) sites inside of the lattice.

Table. 1.1. Reported concepts for the stabilization of ferromagnetic ordering in ZnO

Mechanism	Reference
Bound magnetic polaron ($x_p < 0.18$)	Coey et al. 2005
Heavy incorporation of dopant atoms ($x_p > 0.18$)	Lee et al. 2004, Sandratskii et al. 2006, Nayak et al. 2008
Additional free carriers (codoping e.g. Co,Li)	Sluiter et al. 2005, Gopal and Spaldin 2006
Grain-boundary foam (defects)	Straumal et al. 2009A

2 Theoretical Background

2.1 Chemical Vapor Synthesis (CVS)

Chemical vapor synthesis (CVS) is one of the techniques where nanoparticles are synthesized in gas phase by a chemical reaction. CVS is essentially a modification of chemical vapor deposition (CVD) where process parameters (temperature, supersaturation, residence time) are adjusted to form particles instead of films [Winterer 2002]. The advantages of reaction in the gas phase are very short residence times and nanoscaled powders of high purity, crystallinity and a narrow particle size distribution can be obtained. The biggest disadvantage of the gas-phase methods is that particles are in most cases highly agglomerated once particles are collected as powder.

For nucleation of particles from the gas phase it is necessary to create a supersaturated vapor of a gaseous species. The supersaturated vapor is formed either as a result of chemical reactions (e.g. pyrolysis) or as a result of physical processes (e.g. rapid cooling that reduces the vapor pressure of condensable species), Fig. 2.1. The supersaturated vapor consists of atoms or molecules of species that are present at a partial pressure higher than the vapor pressure of that species [Kodas and Hampden-Smith 1999]. At sufficiently high supersaturation, particles form by homogeneous nucleation. After nucleation, particle growth can proceed in two different ways: via condensation or coagulation [Hinds 1999]. Growth via condensation occurs at low particle concentrations where few possible particle collisions occur and monomers condense onto already existing particles [Kodas and Hampden-Smith 1999]. At high particle concentrations, particles grow via coagulation as they collide and coalesce. Parallel to coagulation, sintering can oc-

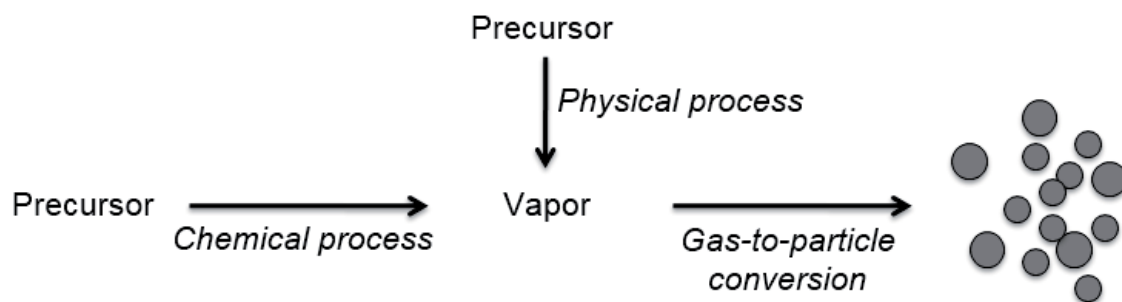


Fig. 2.1. Particle formation from supersaturated vapors [reproduced from Kodas and Hampden-Smith 1999]

cur to form a single particle. This usually happens at high temperatures. In most of cases, the formation of isolated single particles is rare and the final powder is composed of groups of particles which can be loosely linked by Wan der Waals forces (soft agglomerates) or strongly bond by sinter necks by (hard agglomerates) [Friedlander 2000].

2.2 Particle Formation and Growth (CVSSIN Model)

Particle generation in the gas phase involves a variety of physicochemical processes [Kodas and Hamden-Smith 1999]. The formation and growth of particles during chemical vapor synthesis can be modeled using reaction-coagulation-sintering model (CVSSIN) written by Winterer [Winterer 2002]. The model assumes a stationary, ideal, one-dimensional plug flow, without axial dispersion. Several processes, which influence the formation of particles from molecular precursors and the particle and powder characteristics such as particle microstructure, morphology, size distribution, and crystallinity are included in the model. These processes are:

1. Conversion of the precursor into monomers (growth species)
2. Formation of clusters (primary particles or grains) from monomers
3. Coagulation of primary particles and formation of agglomerates
4. Sintering of the primary particles within the agglomerates
5. Heat exchange (with the hot wall) and heat production by the processes 1-4.

Processes 1-4 are described by a system of differential equations and numerically solved using a fifth order Runge Kutta solver. Figure 2.2 schematically shows the particle formation (processes 1-4) in the CVS system.



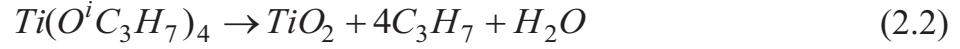
Fig. 2.2. Particle formation in the CVS process [after Winterer 2002]

Precursor decomposition and particle formation (processes 1-2)

In the CVS process the TiO_2 particle are formed through the oxidation of titanium tetra-isopropoxide (TTIP) as precursor (reactant):



Due to the lack of kinetic data for the oxidation, kinetic data for the thermal decompositions were used. The precursor decomposition is described by a first order irreversible reaction:



which can be described by:

$$\frac{dN_p}{dt} = -k \cdot N_p \quad (2.3)$$

where N_p is the number density of the precursor molecules, and k is the reaction constant [Okuyama et al. 1990]:

$$k = k_0 \cdot \exp\left(-\frac{E_a}{k_B \cdot T}\right) \quad (2.4)$$

where k_0 is the pre-exponential factor, E_a is the activation enthalpy, k_B is the Boltzman constant, and T is the process temperature.

Particle coagulation and sintering (processes 3-4)

After the first particles are formed, they collide and form agglomerate particles through coagulation. For particles smaller than 0.1 μm , the Brownian motion (random motion due to collisions with gas molecules) is the main collision mechanism [Hinds 1999]. Particle collision and coagulation lead to a reduction in the total number of particles and an increase in the average size. The rate of change of the number density of the agglomerates (N_a) due to coagulation is:

$$\frac{dN_a}{dt} = -\frac{1}{2} \beta \cdot N_a^2 \quad (2.5)$$

where β is the frequency function for collision between agglomerates calculated according to the Fuchs interpolation formula for coagulation of monodisperse particles:

$$\beta = 4\pi \cdot D_p \cdot d_c \cdot \left(\frac{d_c}{2d_c + 2\sqrt{2} \cdot g} + \frac{2\sqrt{2} \cdot D_p}{c \cdot d_c} \right)^{-1} \quad (2.6)$$

where D_p is the particle diffusion coefficient, d_c is the collision diameter of the agglomerate, c is the (molecular) particle velocity, g is the transition parameter which describes transition from the free molecular ($Kn^1 \gg 1$) to the continuum regime ($Kn \ll 1$). If the particle diameter, d_p is much smaller than the mean free path of the gas ($d_p \ll \lambda_{gas}$) the transition parameter, g will be large compared to

¹ Knudsen number, $Kn = \lambda/d_p$ [-].

the collision diameter and collision frequency function can be described by the form for free molecular regime:

$$\beta = 4 \cdot \left(\frac{6k_B \cdot T \cdot d_c}{\rho_p} \right)^{1/2} \quad (2.7)$$

where ρ_p is the particle density (here taken for anatase $3.895 \cdot 10^3 \text{ kg/m}^3$), k_B is the Boltzman constant, and T is the process temperature (K). The collision diameter of an agglomerate, d_c , is given by:

$$d_c = d_p \cdot \left(\frac{a^3}{36\pi \cdot v^2} \right)^{1/D_f} \quad (2.8)$$

where d_p is the primary particle diameter, v is the volume of a single agglomerate, a is the surface area, and D_f is the mass fractal dimension of the agglomerate. For $D_f = 3$ the collision diameter and the agglomerate diameter are identical. For SiO_2 particles collision $D_f = 2.9$ was used [Winterer 2002].

The collision time, τ_c , or the time needed for the average volume of an agglomerate to double can be calculated from [Winterer 2002]:

$$\tau_c = \frac{1}{N_a \cdot \beta} \quad (2.9)$$

The primary particle diameter, d_p , can be calculated from the volume, v , and the surface area, a , of a single agglomerate particle:

$$d_p = \frac{6v}{a} \quad (2.10)$$

The degree of agglomeration (number of primary particles in an agglomerate), n_p , is expressed by:

$$n_p = \frac{v}{v_p} \quad (2.11)$$

where v_p is the volume of a primary particle.

Parallel to the coagulation process, sintering takes place. The driving force for sintering is the minimization of the particle surface area caused by decreasing the vapor-solid interface. The completion of the sintering depends on the solid state diffusion in the material and time-temperature profile of the process. The rate of decrease of the surface area of an agglomerate particle, a is

$$\frac{da}{dt} = -\frac{1}{\tau_s} \cdot (a - a_s) \quad (2.12)$$

where a_s is the surface area of a completely sintered particle (sphere), and $1/\tau_s$ is the sintering rate (or inverse coalescence time) which in case of grain boundary diffusion, as rate limiting mechanism, can be described by

$$\frac{1}{\tau_s} = \frac{16\sigma \cdot w \cdot \Omega \cdot \gamma \cdot D_{gb}}{k_B \cdot T \cdot d_p^4} \quad (2.13)$$

where σ is the sintering constant, w is the grain boundary (interface) width, Ω is the volume of diffusing species, γ is the interfacial enthalpy, d_p is the primary particle size, and D_{gb} is the grain boundary diffusion coefficient:

$$D_{gb} = D_0 \cdot \exp\left(-\frac{E_D}{k_B \cdot T}\right) \quad (2.14)$$

with D_0 as the pre-exponential constant, E_D as the activation enthalpy of diffusion, and T as the process temperature. As discussed later, sintering rate plays an important role in the final particle morphology.

Table 2.1 summarizes the reaction parameters used in CVSSIN to model formation and growth of TiO₂ particles.

Table 2.1. Reaction parameters used in the CVSSIN model

	Parameter		Reference
Decomposition kinetics	pre-exponential constant, k_0 [1/s]	$3.96 \cdot 10^5$	Okuyama et al. 1990
	activation enthalpy, E_d/k_B [K]	8479	
Sintering	sintering constant, σ [-]	32	Kruis et al. 1993
	grain boundary width, w [m]	$0.5 \cdot 10^{-9}$	Tsureka 1992
	diffusion volume, Ω [m ³]	$1.56 \cdot 10^{-29}$	Liao et al. 1997
	mass fractal dimension, D_f [-]	2.9	this work
	interfacial enthalpy, γ [J/m ²]	0.35	Liao et al. 1997
	pre-exponential constant, D_0 [m ² /s]	$1.5 \cdot 10^{-7}$	§
	activation enthalpy, E_D/k_B [K]	29909	§

§ pre-exponential constant of diffusion and the activation enthalpy were obtained by Arrhenius fit of the data reported by Chiang et al. [Chiang et al. 1997]

Heat balance (process 5)

The heat balance for a stationary, one-dimensional plug flow can be crudely approximated by two terms: (i) the heat exchange between flowing gas and hot wall and (ii) the heat production of the chemical formation reaction (Eq. 2.1):

$$\frac{dT}{dt} = \frac{4\alpha}{c_p \cdot \rho_g \cdot L} \cdot (T_w - T_g) - \frac{\Delta H_R \cdot c_0 \cdot k \cdot \exp(-k \cdot t)}{c_p \cdot \rho_g} \quad (2.15)$$

where α is the convective heat exchange coefficient estimated from the heat conductivity of the gas, κ and the Nusselt number, Nu ($\alpha = \kappa \cdot Nu/L$), L is the diame-

ter of the reactor, ρ_g is the gas density, c_p is the specific heat capacity of the gas (mixture) at constant pressure, T_w is the wall temperature, T is the gas temperature, ΔH_R is the reaction enthalpy, c_0 is the initial precursor concentration, and k is the reaction constant (Eq. 2.4).

2.3 Materials

2.3.1 Titanium Dioxide, TiO₂

Titanium dioxide, TiO₂ exists in three common modifications: rutile (tetragonal), anatase (tetragonal), and brookite (orthorhombic) (Fig. 2.4). Under ambient conditions, macrocrystalline rutile is thermodynamically stable relative to macrocrystalline anatase and brookite. However, at particle diameters below ~ 14 nm, anatase is more stable than rutile [Gibb and Banfield 1997, Zhang and Banfield 1998] due to the lower surface enthalpy [Ranade et al. 2002]. This explains why the anatase phase is mostly observed in the nanoparticles. There is still debate in the literature over the exact mechanism of the corresponding phase transformation(s).

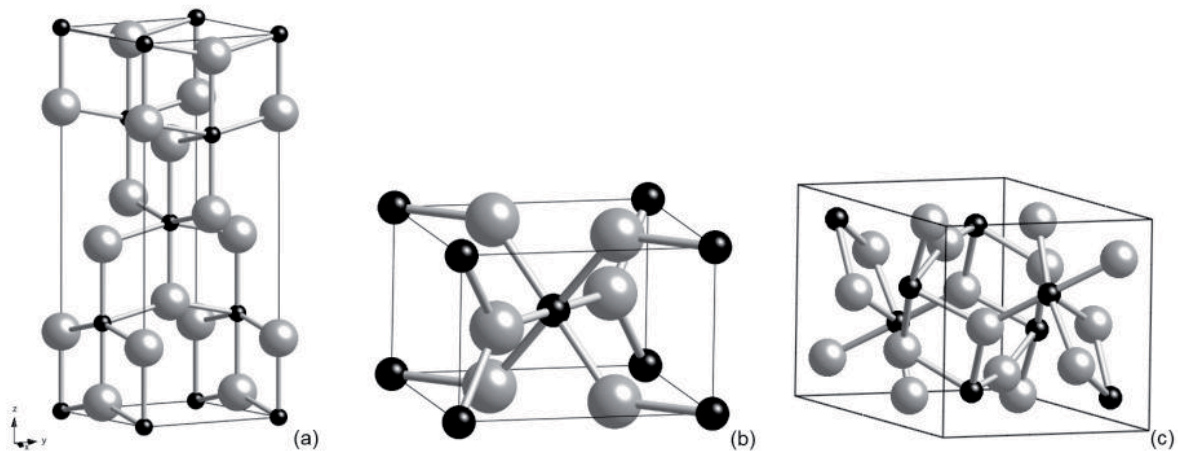


Fig. 2.3. Polymorphs of TiO₂: anatase (a), rutile (b) and brookite (c) (Ti – black, O – gray)

2.3.2 Zinc Oxide, ZnO

Zinc oxide, ZnO crystallizes in three crystal phases (Fig. 2.5): wurtzite (hexagonal), zinc blende (cubic) and rock salt (cubic). The wurtzite structure is most stable at ambient conditions and thus most commonly observed. The zinc blende form can be stabilized by growing ZnO on substrates with cubic lattice structure [Özgür et al. 2005]. The rocksalt structure is only observed at relatively high pressures (9 GPa [Kim et al. 2008]).

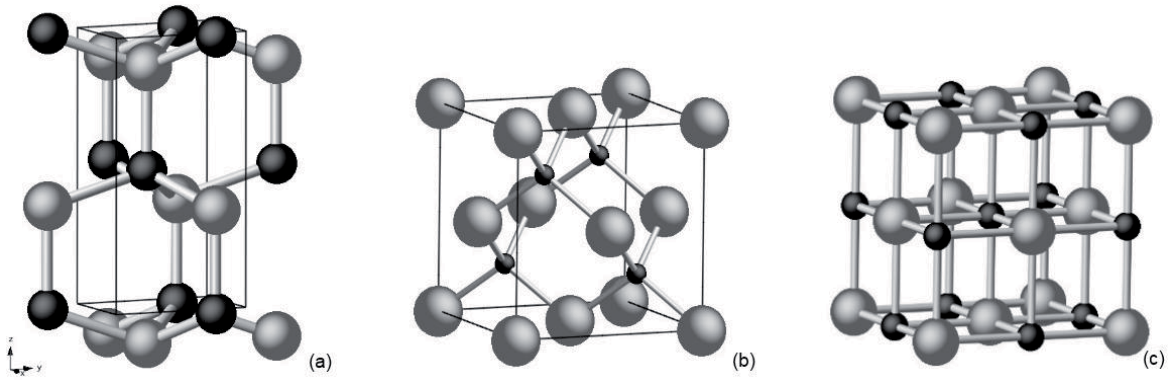


Fig. 2.4. Polymorphs of ZnO: wurtzite (a), zinc blende (b) and rock salt (c) (Zn black, O – gray)

2.4 Particle Characteristics

The properties of nanoparticles (physical, mechanical, electronic, optical, magnetic) can be tuned by adjusting the particle size, particle size distribution, shape or extent of agglomeration [Cao 2004]. Process variables such as process temperature, residence time, precursor gas concentration and cooling rate are some of the variables that can be used to control coagulation and sintering, and consequently, the characteristics of the final powders.

2.4.1 Particle Agglomeration and Size Distribution

Typically powders made in the gas phase have relatively narrow particle size distribution and consist of nonporous primary particles, but often they are agglomerated [Pratsinis and Vemury 1996]. Agglomeration arises from the competition between coagulation and sintering processes (Fig. 2.5). When the characteristic sintering (coalescence) time is much shorter than collision time ($\tau_s \ll \tau_c$), particles rapidly coalesce on collision and form spherical particles (collision limited process). On the other hand, when sintering time is much longer than collision time ($\tau_s \gg \tau_c$), colliding particles stop to coalesce and agglomerates are formed (sintering limited process). The nature and strength of the bonds between the primary particles inside of the agglomerate can be qualitatively estimated from the relation of sintering and coagulation rates [Friedlander 2000]. As the sintering and collision times approach each other ($\tau_s \approx \tau_c$), two types of necks between primary particles can form. When the sintering rate is much faster than the coagulation rate ($d\tau_s/dt \gg d\tau_c/dt$) soft agglomerates are formed (Fig. 2.6a). However, if the sintering rate is just slightly faster

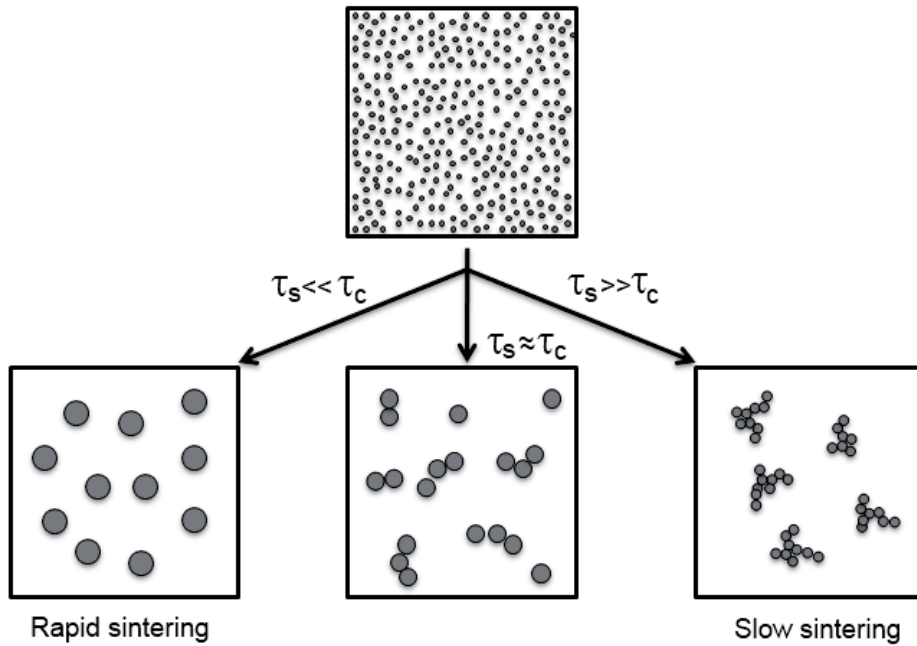


Fig. 2.5. The effect of the characteristic coagulation (τ_c) and sintering (τ_s) times on the type of particles produced by the collision-sintering process [reproduced from Friedlander 2000]

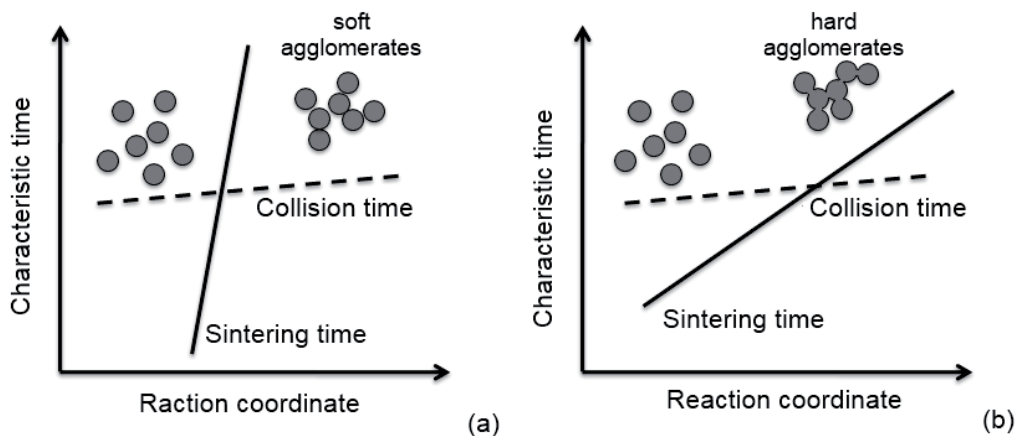


Fig. 2.6. Influence of collision and sintering rates on formation of soft (a) and hard (b) agglomerates [reproduced from Friedlander 2000]

than coagulation rate ($d\tau_s/dt > d\tau_c/dt$), particles have time to sinter only partially. As a result hard agglomerates are formed (Fig. 2.6b). Therefore, the control of coagulation and coalescence is crucial for obtaining non-agglomerated particles.

In the gas phase, particles undergo Brownian coagulation, and the shape of the particle size distribution changes with time. After some time initially monodispersed particles can reach the so-called ‘*self-preserving*’ size distribution [Friedlander 2000]. After this point the polydispersity (width of the distribution) of particles can hardly be reduced. According to Friedlander [Friedlander 2000] the self-preserving distribution can be approximated by a log-normal distribution function with $\sigma_g = 1.44$ for the continuum regime and with $\sigma_g = 1.46$ for the free molecule

regime. For the CVS process standard geometric deviation below 1.4 is typically observed.

In case of CVS a pulsed flow of reactants – depending on pulse length and frequency – can lead to a reduction in reactant and particle concentration by axial dispersion and thereby suppress dynamically the particle growth by chemical reaction and coagulation during their residence time. In this way the microstructure of the particles (degree and type of agglomeration and consequently particle size distribution) can be influenced.

A pulsed flow of reactants can be implemented experimentally using a laser flash evaporator [Winterer et al. 2007] by pulsing the CO₂ laser power. It is of great advantage for a systematic investigation that all other process parameters remain unchanged. In this way, it should be possible to reduce the particle number density and to achieve narrow particle size distribution in CVS. Figure 2.7 schematically illustrates this idea. When the pulse of precursor is delivered into the reactor (time: t_0) due to the molecular diffusion it starts to spread (times: t_1 and t_2) along the reactor. This can be described using the axial dispersion coefficient, D_a [Levenspiel 1999]:

$$\frac{\partial c}{\partial t} = \left(\frac{D_a}{uL} \right) \frac{\partial^2 c}{\partial z^2} - \frac{\partial c}{\partial z} \quad (2.16)$$

where (D_a/uL) is the parameter that measures the extent of axial dispersion called “dispersion number” (dimensionless), u is the velocity, L is the reactor length, c is the concentration, and $z = (ut + x)$. Solution of Eq. 2.16 is the symmetrical curve which is similar to Gaussian curve described by mean value and variance ($\sigma^2 = 2D_a/uL$). The main challenge is to keep pulses far enough from each other in order to avoid their mixing and to retain pulsed flow. As discussed later, this will be achieved by varying the laser pulse repetition frequency and duty cycle.

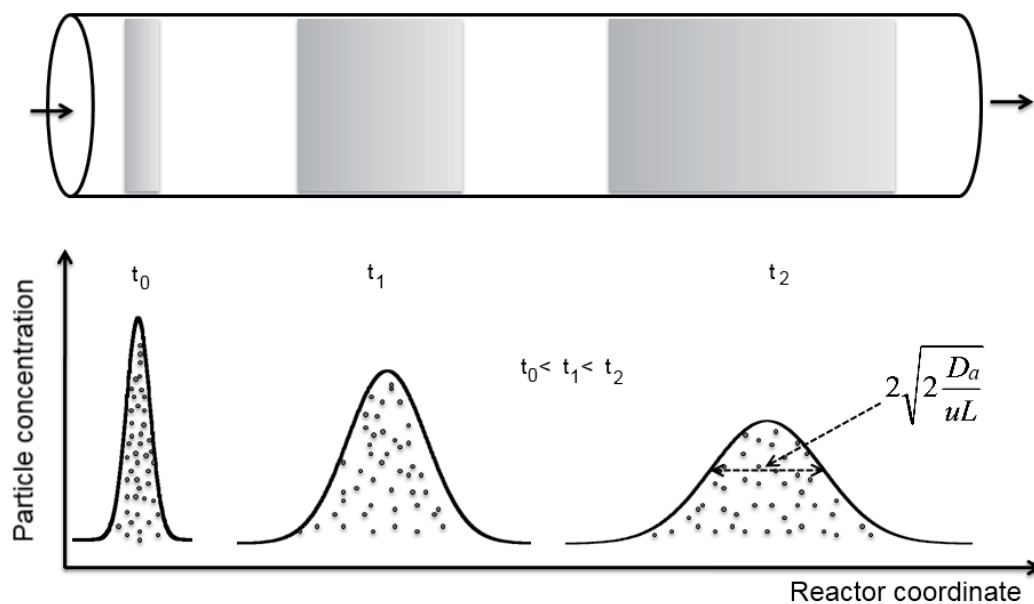


Fig. 2.7. The spreading of precursor pulse according to dispersion model [after Levenspiel 1999]

2.4.2 Magnetic Properties

There are two contributions to the magnetic moment μ of an electron: the orbital moment, μ_l resulting from the motion of the electron in its orbit, and the spin moment, μ_s resulting from a spinning motion of the electron about its own axis. The orbital and spin contributions associated with all the electrons in a full electron shell tend to balance one another so that the resulting magnetic moment is zero. Cooperative magnetism is observed only for partially filled electron shells [Givord 2006]. In the solid state, the mixing of orbitals often leads to the disappearance (quenching) of the orbital magnetic moment. The nature of the coupling between magnetic moments depends strongly on the elements that are present, and on the crystallographic arrangement of the atoms [Givord 2006].

Materials are classified as diamagnetic, paramagnetic, ferromagnetic, antiferromagnetic and ferrimagnetic, according to their response to an external magnetic field (Fig. 2.8). The magnetic susceptibility (χ) (Fig. 2.9) is used as a measure how responsive material is to an applied magnetic field [Culity 2009].

Diamagnetic materials are composed of atoms which have no net magnetic moment due to the absence of unpaired electrons. These materials have a small and negative susceptibility [Hornyak 2009].

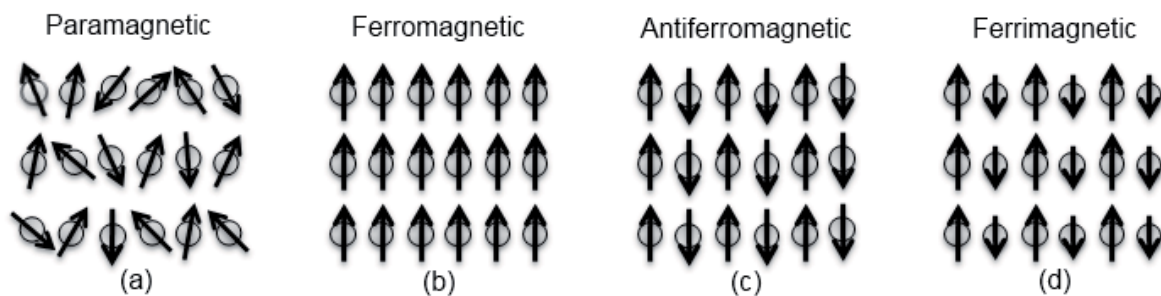


Fig. 2.8. Schematic illustration of different types of magnetic moment interactions: paramagnetic (a), ferromagnetic (b), antiferromagnetic (c), and ferrimagnetic (d) [after Shriver and Atkins 1999]

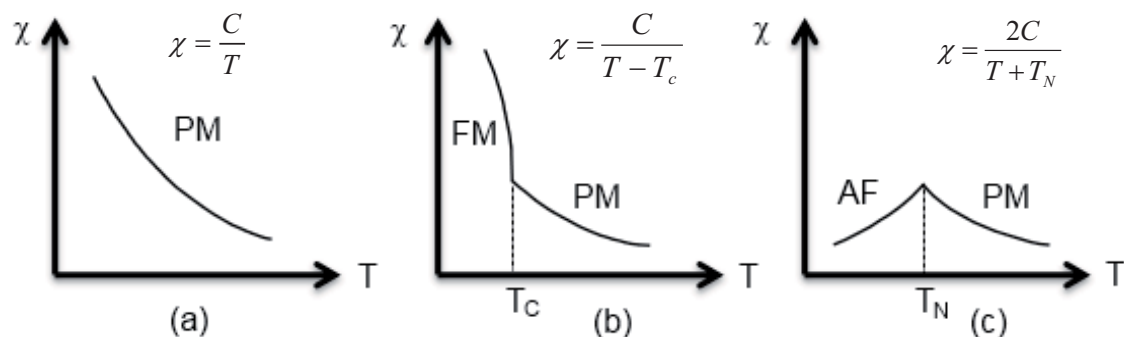


Fig. 2.9. Temperature dependence of the magnetic susceptibility for paramagnetic (a), ferromagnetic (b) and antiferromagnetic (c) materials [reproduced from Shriver and Atkins 1999]

Paramagnetic materials possess unpaired electrons and in the absence of a magnetic field, the magnetic moments are randomly oriented (Fig. 2.8a). In the presence of an external magnetic field, the magnetic moments tend to align parallel to the applied magnetic field, but thermal agitation obstructs this tendency [Hornyak 2009], and the magnetic moments are only partially aligned resulting in a small but positive magnetic susceptibility (Fig. 2.9a) (χ) which varies with temperature (T) according to the Curie law [Culity 2009]:

$$\chi = \frac{C}{T} \quad (2.17)$$

where C is the Curie constant.

Ferromagnetic materials are materials whose magnetic moments are parallel orientated (Fig. 2.8b) to an applied magnetic field. After an applied field is removed, a magnetization (remanence) remains up to certain extent. The magnetic field required to reduce the remanence to zero is called coercive field (coercivity). A property of material to remember its magnetic history is called hysteresis, Fig. 2.10. Ferromagnetic materials have large and positive magnetic susceptibility, Fig. 2.9b [Hornyak 2009, Culity 2009]. Above the Curie temperature (T_C) ferromagnet loses the remanence and becomes paramagnetic with magnetic susceptibility that can be described by Curie-Weiss law:

$$\chi = \frac{C}{T - T_c} \quad (2.18)$$

Ferromagnetism is usually observed in materials containing unpaired electrons in d or f orbitals [Shriver and Atkins 1999].

Antiferromagnetic materials are materials in which magnetic moments are ordered in an antiparallel arrangement (Fig. 2.8c) with zero net magnetic moment at temperatures below the ordering called Néel temperature ($T_N = \theta$) [Kittel 1976]. These materials have a small and positive susceptibility at all temperatures

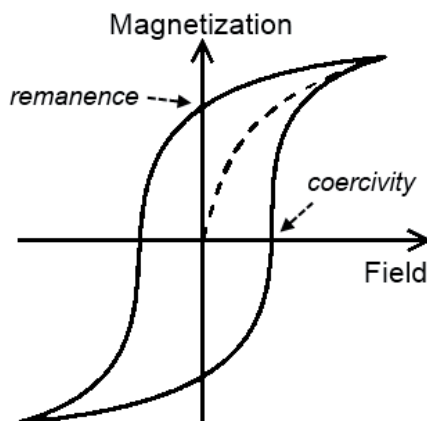


Fig. 2.10. Hysteresis of ferromagnetic material

(Fig. 29c). Above Néel temperature, material becomes paramagnetic with magnetic susceptibility that can be described by [Kittel 1976]:

$$\chi = \frac{2C}{T + T_N} \quad (2.19)$$

Antiferromagnetism is often observed in molecular complexes containing two metal atoms which are linked by ligands [Shriver and Atkins 1999].

Ferrimagnetic materials are materials whose magnetic moments are oriented antiparallel, as in antiferromagnets, but they are not equal (Fig. 2.8d), therefore the net magnetic moment is not zero. Ferrimagnetic materials consist of two different metal ions or of the same metal ions with different valences. The susceptibility of these materials is large and positive and they retain the magnetization in the absence of a field and below Curie temperature, similarly to the ferromagnetic materials [Hornyak 2009, Vollath 2008].

3 Experimental Methodologies

3.1 Operational Units of CVS Setup

A typical CVS setup consists of following sequences of unit operations (Fig. 3.1): gas supply, precursor delivery, hot-wall reactor (heat source), particle collector, temperature and pressure control system (vacuum pump, absolute pressure gauge, and butterfly valve). The basic principle of the gas phase particle synthesis is that after a precursor (liquid or solid) is evaporated, the vapors are transferred into the hot-wall reactor using a carrier gas (helium) where they react with oxygen to form oxide nanoparticles at controlled temperature and pressure.

3.1.1 Precursor Delivery

There are different ways to deliver precursor vapors into the reactor depending on precursor state. In this work two types of precursors were used – liquid and solid. For the evaporation of liquid precursors a *bubbler* was used, while for the evaporation of solid precursors the *flash evaporator* was used.

A *bubbler* is a stainless steel vessel (Fig. 3.2a) which is partially filled with a liquid precursor. The precursor is indirectly heated using a thermal (oil) bath in order to be evaporated. The precursor vapor is delivered to the reactor by a carrier gas (here helium) that is fed through the bubbler. The temperature at which precursor evaporates is selected according to the required precursor molar flow, \dot{n}_{prec} , which can be calculated knowing the precursor vapor pressure, p_{prec} , at that tem-



Fig. 3.1. Sequences of unit operations in a CVS setup

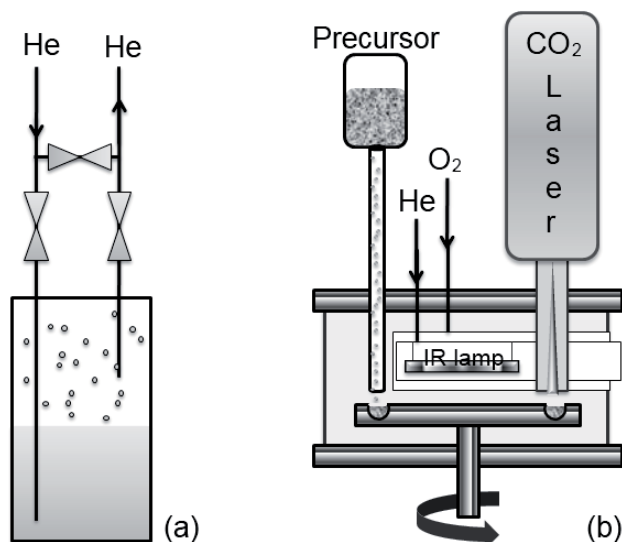


Fig. 3.2. Precursor delivery units: bubbler (a) and flash evaporator (b)

perature, pressure in the system, p and the molar flow of the carrier gas (helium), \dot{n}_{He} :

$$\dot{n}_{prec} = \left(\frac{p}{p - p_{prec}} \right) \cdot \dot{n}_{He} \quad (3.1)$$

A *flash evaporator* (Fig. 3.2b) consist of stainless steel chamber where a solid precursor is filled continuously into a ring-shaped groove located in the rotating stainless steel plate. The precursor is evaporated (sublimated) at a position close to the entrance to the reactor by a CO_2 laser and transported via a very short distance to the reactor by a preheated inert gas (helium) flow [Winterer 2007]. The wavelength of the CO_2 laser ($10.6 \mu m$) is advantageous as almost all metal organic compounds have a nearby absorption maximum. Therefore, a large number of solid precursors can be evaporated and a wide range of powders, from simple oxides, doped and complex oxides, to non-oxides can be produced using the flash evaporation method. An additional advantage of flash evaporation is the possibility to vary the laser pulse repetition frequency and duty cycle, allowing dynamic control over the amount of precursor that can be delivered into the reactor (more details are given in the section 3.3.1.2).

3.1.2 Hot-Wall Reactors as Heat Sources

The precursor vapor(s) react(s) at desired temperature and pressure with oxygen inside the hot-wall reactor consisting of alumina tube (18 mm inner diameter) and energy source. Two types of heating were used in this work: (i) *resistance heating* using a commercial *resistance furnace* (Fig. 3.3) operating up to 1473 K and (ii) *induction heating* using an *induction furnace* (Fig. 3.4) designed and built in this work operating at temperature well above 1473 K.

A *resistance furnace* converts a electric current, I , which flows through a resistor (e.g. metallic wire wound on ceramic tube), into heat, Q , based on Joule's law [Ganić and Hicks 2003]:

$$Q = I^2 \cdot R \cdot t \quad (3.2)$$

where R is the electrical resistance of the heating element, and t is the time. Generated heat is transferred to the reaction process by conduction, convection or radiation.

The wall temperature is measured by a thermocouple placed in between the protective tube and the heating element and controlled by temperature controller. In this work a Carbolite (MTF 12/38/400) resistive furnace with a wide zone of constant temperature and maximum operating temperature of 1473 K was used.

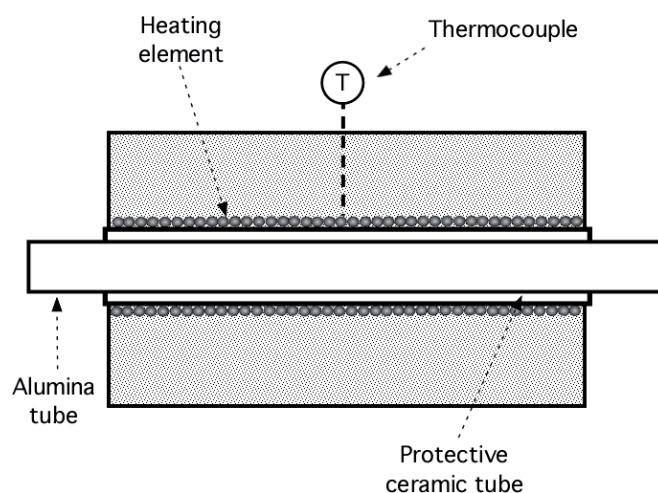


Fig. 3.3. Schematic illustration of a resistance furnace

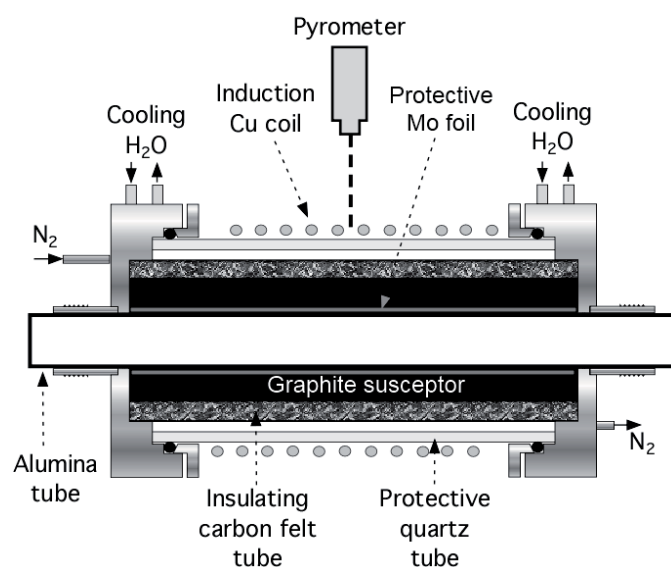


Fig. 3.4. Schematic illustration of induction furnace

An *induction furnace* is based on heat generation by eddy currents in an electrically conductive material. It consists of a water cooled copper coil (inductor), a graphite susceptor (heat source) in the form of a tube and a protective (insulating) graphite felt (in a form of a tube), protective quartz tube flashed with nitrogen in order to prevent oxidation of the graphite susceptor when heated (Fig. 3.4). An AC power supply (Hüttinger HF-Generator BIG 20/100) sends an alternating current (AC) through the copper coil (inductor), generating a time-dependent magnetic field which induces eddy currents within the graphite susceptor, generating the heat (Eq. 3.2). Heat is transferred from the susceptor to the wall of reactor tube (alumina), which is placed inside of the graphite susceptor. The temperature of the graphite susceptor is measured using a pyrometer and controlled by changing the value of the AC voltage (manually controlled). The induction furnace is advantageous compared to the commercial resistance furnace because the wall temperature profiles can be relatively easy adjusted by changing, for example, the design of coil (this work), or changing the design of the susceptor, and much higher temperatures can be achieved (well above 1473 K). In this work three types of the induction coils and consequently three types of the wall temperature profiles (here named ‘flat’, ‘down’, and ‘up’) were created as it is schematically shown in Fig. 3.5. In this way not only the temperature profiles of the reactor wall are changed, but also time-temperature history of particles inside of the reactor.

The total molar flow of gases (precursor vapor, helium and oxygen) through the reactor, \dot{n}_{tot} will determine the residence time, τ_r of the particles in the reaction zone for defined process temperature, T and the pressure, p :

$$\tau_r = \frac{p \cdot V}{\dot{n}_{tot} \cdot R \cdot T} \quad (3.3)$$

where R is the gas constant, and V is the reactor volume.

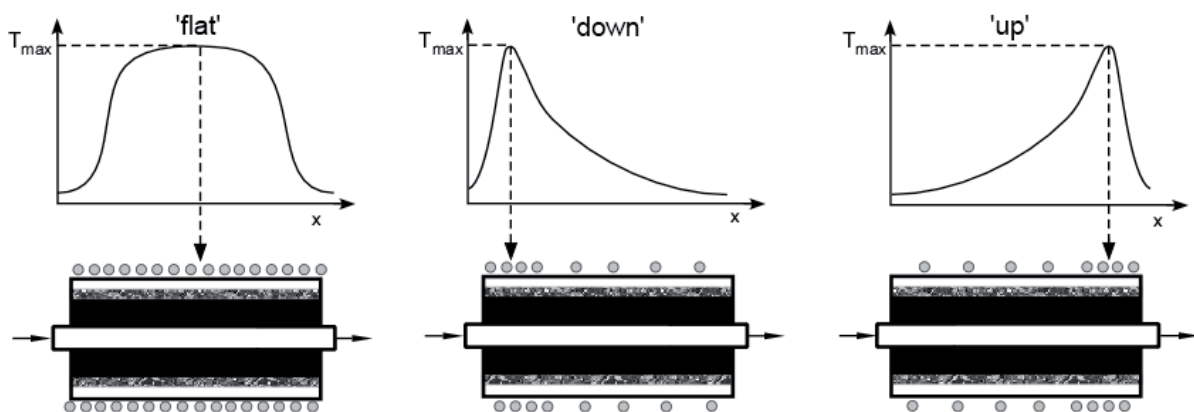


Fig. 3.5. Schematic illustration of the induction furnace with three different induction coils designed to obtain different temperature profiles: ‘flat’, ‘down’ and ‘up’ (arrows in the lower part of the illustration show the direction of the gas flow)

3.1.3 Particle Collection

The particle collector (Fig. 3.6) consists of water cooled channels ($T \approx 293$ K) and heating elements (infrared lamps, $T \approx 773$ K) which are placed in the center of the channels. Due to the temperature gradient particles experience a force in the direction of the decreasing temperature and deposit on the walls. For particles smaller than the gas mean free path ($d_p < \lambda_{gas}$, free molecular regime), the thermophoretic force is a result of a higher transfer of momentum from hot gas molecules (due to higher thermal velocity) to the particles compared to cold gas molecules. The thermophoretic force, F_{th} acting on the particles is proportional to their size, d_p and the strength of the temperature gradient, ∇T [Hinds 1999]:

$$F_{th} = -\frac{p \cdot \lambda_{gas} \cdot d_p^2 \cdot \nabla T}{T} \quad (3.4)$$

where p is the gas pressure, λ_{gas} is the gas mean free path, and T is the absolute temperature of the particle. The velocity of thermophoresis, V_{th} is independent of particle size and directly proportional to the temperature gradient, ∇T :

$$V_{th} = -\frac{0.55\eta \cdot \nabla T}{\rho_g \cdot T} \quad (3.5)$$

where η and ρ_g are the viscosity and the density of the gas, respectively.

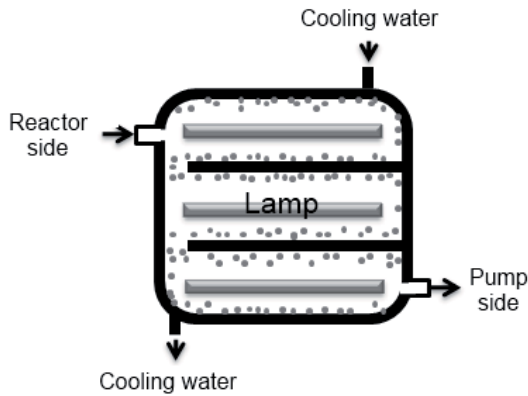


Fig. 3.6. Thermophoretic particle collector

3.2 Reactor Temperature Measurement

Two different measurement principles for the CVS reactor wall temperatures were used in this work: (i) contact measurement by a thermocouple in the case of experiments with the resistance furnace and (ii) non-contact measurement using a pyrometer in the case of the induction furnace.

A *thermocouple* is temperature sensor consisting of two wires made of two dissimilar metals which are joined together at one end and at the other end connected to an external electric circuit [Holman 2001] which measures a created electric potential, known as the Seebeck thermoelectric potential which is proportional to the temperature difference [Vanvor 1989].

A *pyrometer* is non-contact device that measures thermal radiation ($\lambda = 0.1\text{--}100\ \mu\text{m}$) emitted by an object. A pyrometer consists of an optical system which focuses the thermal radiation onto the detector. The output signal of the detector (temperature, T) is related to the energy, E emitted from the target object through the Stefan-Boltzmann law [Holman 2001]:

$$E = \varepsilon \cdot \sigma \cdot T^4 \quad (3.6)$$

where σ is the constant of proportionality called the Stefan-Boltzmann constant ($5.669 \cdot 10^{-8}\ \text{W/m}^2\text{K}^4$) and ε is the emissivity of the object. The emissivity of the object is an important variable in converting the detector output into an accurate temperature signal. In this work, pyrometer Sensotherm Metis MI16 ($\lambda = 1.6\ \mu\text{m}$) operating in temperature range 623–2073 K was used in the experiments with induction furnace to measure the temperature of the graphite susceptor. Emissivity for graphite susceptor was set to 0.8 [Omega 1998].

3.3 Synthesis of Nanoparticles

3.3.1 TiO₂ Nanoparticles

Nanocrystalline TiO₂ particles are synthesized using two different CVS setups:

1. In order to study the influence of different time-temperature profiles on the particle characteristic (phase composition, particle size, crystallinity, degree of agglomeration) a CVS setup with a bubbler and an induction furnace (Fig. 3.7) was used to synthesize the TiO₂ particles from a liquid precursor (titanium-tetraisopropoxide, TTIP).
2. In order to study the influence of particle number concentration on the particle size and size-distribution, a CVS setup with a flash evaporator and a resistive furnace (Fig. 3.8) was used to synthesize TiO₂ particles from a solid precursor (titanium diisopropoxide bis(tetramethylheptanedionate), Ti-(^tP)₂(TMHD)₂).

3.3.1.1 The Influence of Time-Temperature Profiles on Particle Characteristics

Figure 3.7 shows a schematic illustration of the CVS-setup used for the TiO_2 particle synthesis from titanium-tetraisopropoxide, TTIP (98%, ABCR, Germany). Helium carrier gas (150 sccm¹) is used to transport the precursor vapor from the bubbler (the temperature is maintained at 333 K using an oil bath thermostat) to the reaction zone, and oxygen (1000 sccm) is used as reaction gas. The gas flow was controlled by thermal mass flow controllers (MKS Instruments). In the hot zone of the reactor the precursor vapor decomposes and reacts with oxygen to form oxide particles. The process pressure is held constant at 20 mbar using a Baratron absolute pressure gauge and a butterfly valve with aid of pumping system (dry screw pump Busch Cobra NC 0600A). The particles are then transported by the gas stream to the particle collector, where they are separated from the gas flow by thermophoresis. As a hot-wall reactor, the induction furnace was used. Three induction coils (Fig. 3.5) were used in order to change the temperature profile of the gas phase. The first type of coil creates the ‘flat’ temperature profile similar to the profile in the standard resistance furnace with a maximum wall temperature located in the center of the furnace. The other two types of coils create two step temperature profiles: ‘up’ and ‘down’ with the maximum wall temperature located closer to the end or the entrance of the reactor, respectively (see Fig. 3.5). In the first set of experiments the TiO_2 nanoparticles were synthesized using the ‘flat’ temperature profile with maximum reactor wall temperatures in the range from 873 K up to 2023 K. The second set of experiments was performed using the ‘up’ temperature profile setting the maximal reactor wall temperature in range from 1273 K up to 2023 K. The last experiment was performed at 1473 K using the ‘down’ temperature profile. The wall temperatures in all experiments were measured using a pyrometer. The details of positions at which wall temperatures were measured and how the data for the wall temperature profiles are determined prior to use in CVSSIN model are given in the Appendix (Tables A and B).

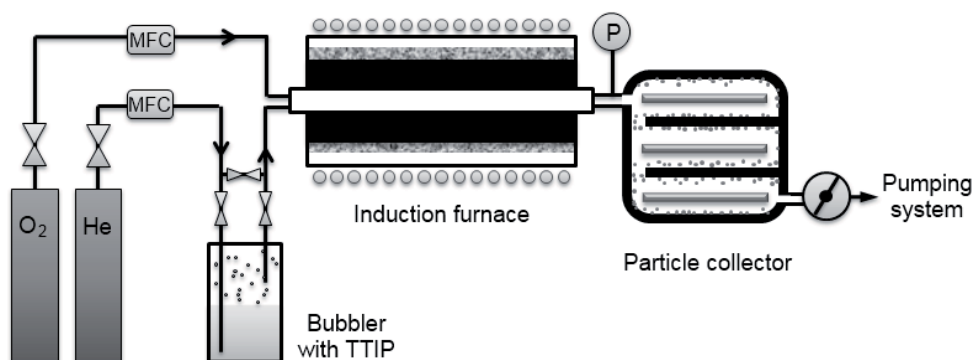


Fig. 3.7. The CVS setup for synthesis of TiO_2 nanoparticles from liquid precursor

¹ standard cubic centimeter per minute

3.3.1.2 The Influence of Particle Number Concentration on Width of Particle Size Distribution

Figure 3.8 schematically illustrates a CVS setup used for the TiO₂ particle synthesis from titanium diisopropoxide bis(tetramethylheptanedionate), Ti(ⁱP)₂(TMHD)₂ (95%, ABCR, Germany). The precursor was continuously (manually) fed into the flash evaporator and evaporated using a CO₂ laser (Coherent GEM, operated at 95 W). In order to study the influence of the particle number concentration on the width of the particle size distribution, the precursor has to be delivered in pulses into the reactor. In this work, different pulses of precursors were created by varying the CO₂ laser pulse repetition frequency and the duty cycle.

The *pulse frequency*, f (Hz) is defined as the inverse of the period, P in which laser is in operation (so-called “On-time”):

$$f = \frac{1}{P} \quad (3.7)$$

and the *duty cycle*, DC (%) is defined as the ratio of the “On-time” (t) to the period (P):

$$DC = \frac{t}{P} \quad (3.8)$$

Figure 3.9 schematically illustrates the frequency and duty cycle definitions. Each state when the laser is “ON” defines the amount of precursor which enters the reactor and consequently the particle number concentration. The laser repetition frequency and duty cycle were varied ($f = 0.2\text{--}25$ kHz; $DC = 20\text{--}100$ %) in each experiment. Schematic illustration of some of the frequency and duty cycle combinations is shown in Fig. 3.10.

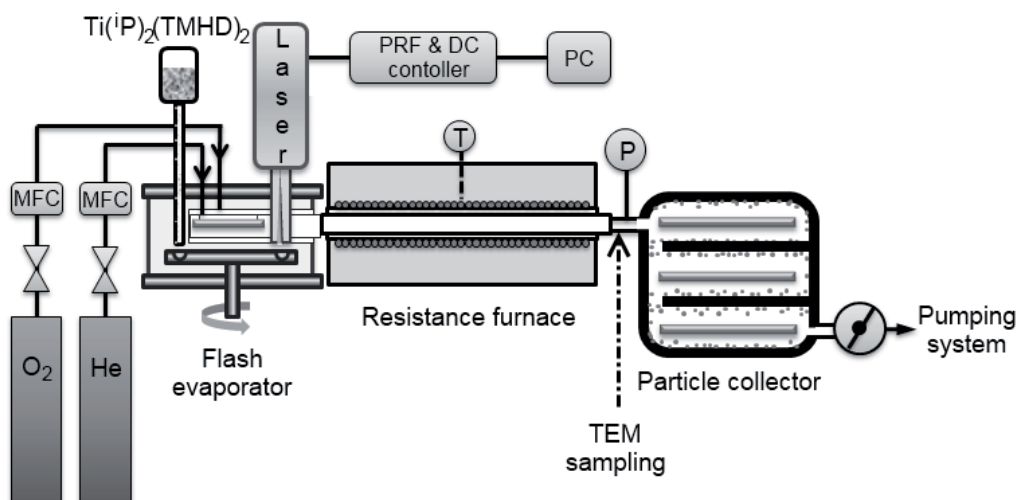


Fig. 3.8. The CVS setup for synthesis of TiO₂ nanoparticles from solid precursor

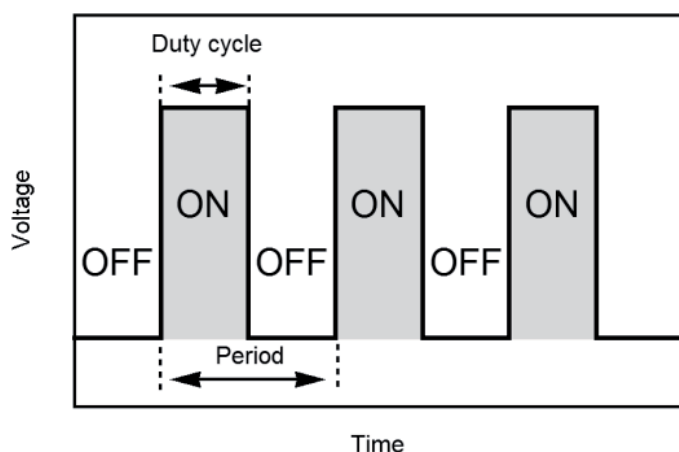


Fig. 3.9. Schematically illustration of the laser duty cycle

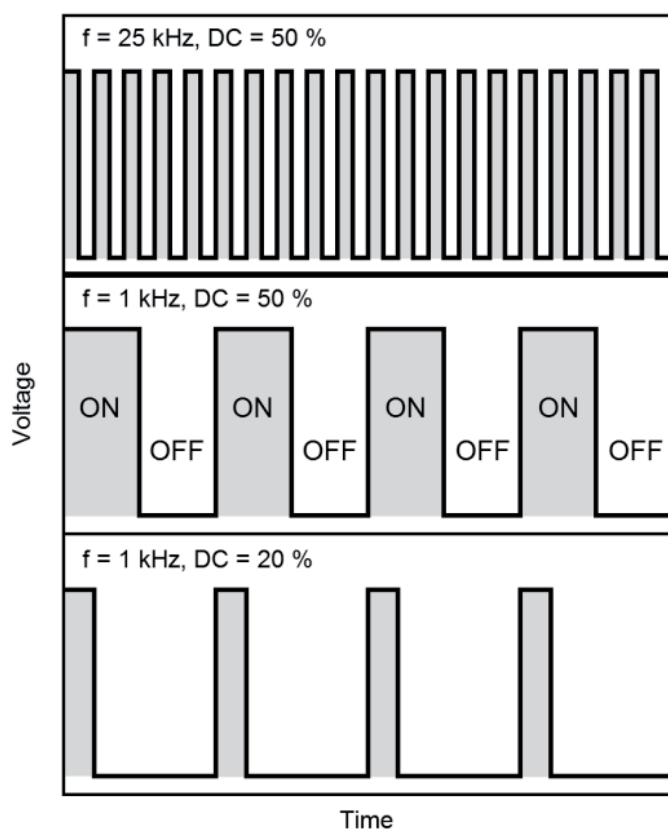


Fig. 3.10. Schematic illustration of the frequency and duty cycle combinations. The gray areas represent the laser “ON” state in which a defined amount of precursor is evaporated

After the precursor is evaporated, its vapor was carried by a helium stream (1020 sccm) into the hot-wall reactor where the TiO_2 particles are formed reacting with 1000 sccm of oxygen at a temperature of 1273 K and a pressure of 20 mbar. Particles are collected in the thermophoretic particle collector. For each experiment particles were also sampled thermophoretically in-situ [Dobbins and Megarids 1987] by deposition on a Cu-grid with a carbon film for investigation with the electron microscope (particle size distribution).

3.3.2 Co-doped and Co,Li-doped ZnO Nanoparticles

Nanocrystalline ZnO particles doped with cobalt ($\text{Zn}_{1-x}\text{Co}_x\text{O}$, $x = 0-0.50$) are synthesized in a CVS reactor consisting of two sequential resistive furnaces and ceramic (alumina) tube (Fig. 3.11). Anhydrous solid zinc acetate, $\text{Zn}(\text{OAc})_2$ (Sigma Aldrich, 99.9% purity) and cobalt acetate $\text{Co}(\text{OAc})_2$ (Sigma Aldrich, 99.9% purity) powders are thoroughly mixed in a mortar under inert conditions inside a glovebox corresponding to a nominal Co content, x . The precursor mixture was transferred under inert conditions to the laser flash evaporator. The radiation of a CO_2 laser (95 W, $f = 25$ kHz, $DC = 50\%$) is used to evaporate the precursor mixture. The precursor vapors are transported into the hot-wall reactor using helium as carrier gas (1020 sccm) where they react with oxygen (1000 sccm) to form the particles. A wall temperature of 1373 K and a total pressure of 20 mbar were used for all experiments. The particles are thermophoretically separated from the gas flow in the particle collector. Co,Li-doped ZnO nanoparticles ($\text{Zn}_{0.95-y}\text{Co}_{0.05}\text{Li}_y\text{O}$, $y = 0-0.05$) are prepared using the same procedure and experimental parameters as in case of Co-doped ZnO. Lithium acetate precursor (LiOAc, Sigma Aldrich, 99.99%) was used as a source for Li.

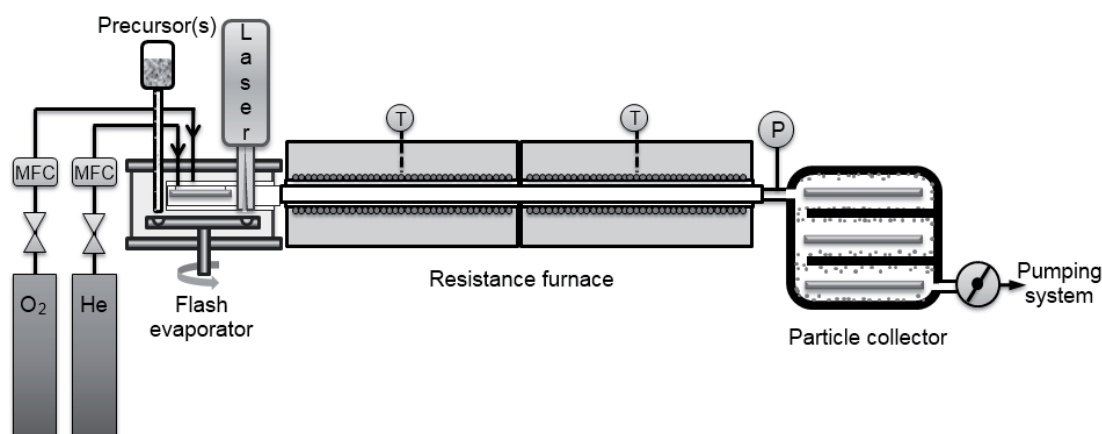


Fig. 3.11. The CVS setup for synthesis of Co-doped and Co,Li-doped nanoparticles

3.4 Particle Characterization

3.4.1 X-Ray Diffraction (XRD) and Rietveld Refinement

X-ray diffraction (XRD) is one of the most important methods for materials characterization. It provides information on crystal structure and defects averaged over the sample volume (volume weighted technique). The diffraction of X-rays is a result of their scattering from atoms arranged in a lattice. The spacing between

atoms and lattice planes is in the order of the wavelength of the X-rays. Bragg's law describes the principle for X-ray diffraction [Hornyak et al. 2008]:

$$n \cdot \lambda = 2d \cdot \sin \theta \quad (3.9)$$

where n is an integer, λ is the wavelength of the incident wave, d is the spacing between the lattice planes in the crystal, and θ is the angle between the incident X-ray and the scattering planes.

The Rietveld refinement [Rietveld 1969] of XRD data is a well established method for extracting information about the phase composition, crystal structure parameters (cell parameters, atomic displacements, atomic occupation numbers, temperature factors, preferred orientation parameters) and the microstructural characteristics of samples (microstrain and crystallite size) from XRD patterns. The Rietveld refinement is based on the least square method that is used to minimize the difference between observed and calculated profile (residual function - weighted sum of squares, WSS) [Young 1995]:

$$WSS = \sum w_i \cdot (Y_{oi} - Y_{ci})^2 \quad (3.10)$$

where w_i is the weighting factor = $1/Y_{oi}$, Y_{oi} and Y_{ci} are the observed and calculated intensity at i^{th} step, respectively. The calculated intensity Y_{ci} is defined as:

$$Y_{ci} = bkg_i + s \sum_{k=1}^{N_{peaks}} L_k |F_k|^2 \phi(2\theta_i - 2\theta_k) P_k A \quad (3.11)$$

where bkg_i is the background (polynomial) function, s is the scale factor, L_k is the Lorentz-polarization factor (defined by the geometry of the instrument), F_k is the structure factor for the k th Bragg reflection, ϕ is the reflection profile function (often used liner combination of Gaussian (strain) and Lorentzian (size) functions called pseudo-Voigt), θ is the Bragg's diffraction angle, P_k is the preferred orientation function, A is the absorption multiplier (accounts for absorption of both incident and diffracted beams and nonzero porosity of the powdered sample) [Pecharsky and Zavalij 2009]. The structure factor, F_k is defined by details of the crystal structure (coordinates and types of atoms, their distribution, and thermal motion):

$$F_k = \sum_i N_j f_j t_j \exp\{2\pi i \cdot (hx_j + ky_j + lz_j)\} \quad (3.12)$$

where N_j is the occupation factor of the j th atom, f_j is the atomic scattering factor describing the interaction of the incident wave with a specific type of an atom, t_j is the temperature (Debye-Waller) factor which describes the temperature motion of the j th atom, $i = (-1)^{1/2}$, h , k , l are the Miller indices, and x_j , y_j , and z_j are the atom position parameters in the unit cell.

There are several programs available for the Rietveld refinement of the XRD data (e.g. TOPAS, FullProf, GSAS, Maud etc.). In this a work program developed

by Lutterotti and Scardi [Lutterotti and Scardi 1990] called MAUD (version 2.14) was used.

The following figures of merit (residuals) are used to characterize quality of the refinement:

- The weighted profile residual, R_{wp} :

$$R_{wp} = \sqrt{\frac{\sum w_i \cdot (Y_{oi} - Y_{ci})^2}{\sum w_i (Y_{oi})^2}} \quad (3.13)$$

- The expected profile residual, R_{exp} :

$$R_{exp} = \sqrt{\frac{n - p}{\sum w_i (Y_{oi})^2}} \quad (3.14)$$

where n is the number of data points and p is the number of free least squares parameters.

- The goodness of fit, $GofF$ is defined as:

$$GofF = \sqrt{\frac{R_{wp}}{R_{exp}}} \quad (3.15)$$

The volume-weighted crystallite size can be related to the average crystallite diameter and the dispersion of the log-normal distribution by [Hinds 1999]:

$$f(d) = \frac{1}{\sqrt{2\pi} \cdot d \cdot \ln \sigma_g} \cdot \exp\left[-\frac{(\ln d - \ln d_g)^2}{2(\ln \sigma_g)^2}\right] \quad (3.16)$$

where d is the crystallite diameter, d_g is the geometric mean diameter, and σ_g is the geometric standard deviation (dimensionless; ≥ 1). Therefore, it is in principle possible to obtain also information on crystallite size distribution from XRD data.

The degree of crystallinity, Γ can be estimated from the integrated peak intensity ($2\theta = 20\text{--}120^\circ$) (with, $I+B$ and without, I background, respectively) of the sample divided by the integrated peak intensity of well crystalline standard (LaB_6) sample measured under the same conditions:

$$\Gamma = \frac{\int [I/(I+B)]_{sample} d(2\theta)}{\int [I/(I+B)]_{reference} d(2\theta)} \quad (3.17)$$

A PANalytical X-ray diffractometer (X'Pert PRO) with Ni-filtered Cu K_α radiation ($\lambda = 0.15406$ nm) produced at 40 kV and 40 mA was used for collection of the XRD patterns of as-synthesized powders. The data are recorded over a 2θ range from 20 to 120° with a step size of 0.03° and a sampling time of 200 s/step using a X'Celerator detector.

The Rietveld refinement was used in order to obtain information about phase composition, crystallite size and crystallite size distribution of TiO₂ nanoparticles. In case of Co-doped and Co,Li-codoped ZnO it was used to extract information about phase composition, crystallite size, lattice parameters (a , b) and oxygen position parameter (u). In order to eliminate the influence of the instrument on the diffraction patterns (broadening and asymmetry of the peaks), the instrumental resolution function was obtained by refinement of the XRD pattern of LaB₆ standard powder (NIST).

3.4.2 Low-Temperature Nitrogen Adsorption

Low-temperature nitrogen adsorption is a technique to determine surface area and pore size distribution of porous materials regardless of their chemical composition and crystal structures. When a gas comes in contact with a solid surface under suitable temperature and pressure the molecules will adsorb onto the surface and reduce the surface energy. Adsorption may be either physisorption or chemisorption. For physical adsorption, the amount of gas needed to form a monolayer or to fill pores can be measured as a function of gas pressure.

The Brunauer-Emmett-Teller (BET) theory is used to explain the physisorption (multilayer) of gas molecules (here nitrogen). The BET equation [Lowel et al. 2004] describes the linear part of the adsorption isotherm:

$$\frac{p}{W \cdot (p_0 - p)} = \frac{1}{W_m \cdot C} + \frac{C-1}{W_m \cdot C} \cdot \frac{p}{p_0} \quad (3.18)$$

where p is the equilibrium experimental pressure, p_0 is the vapor pressure of the adsorbate gas (here nitrogen) at experimental temperature (here 77 K), and W and W_m are the adsorbed and monolayer weights, respectively, and C is the BET constant defined as the heat of adsorption, ΔH_{ads} (for the first physisorbed layer) and the latent heat of condensation, ΔH_{cond} (additional layers):

$$C = \exp\left(\frac{\Delta H_{ads} - \Delta H_{cond}}{R \cdot T}\right) \quad (3.19)$$

In the range of relative pressures from $0.05 < (p/p_0) < 0.35$ the adsorption isotherm (Eq. 3.18) has a linear region from which the mass of the adsorbed monolayer (W_m), the BET constant, C and consequently, the specific surface area, S_s [m²/g] can be calculated by:

$$S_s = \frac{A \cdot N_A \cdot W_m}{M \cdot m} \quad (3.20)$$

where A is the area covered by absorption of one gas molecule (0.162 nm² for nitrogen), N_A is the Avogadro's constant, M is the molecular mass of the adsorbate, m is the mass of the solid material.

Assuming the spherical particles, the particle size, d_{BET} can be calculated from the specific surface area using the following expression:

$$d_{BET} = \frac{6}{S_s \cdot \rho} \quad (3.21)$$

where ρ is the density of material.

The specific surface area of TiO₂ particles was measured using a Quantachrome Autosorb-1C instrument. Prior to the measurement particles were degassed at 423 K for approximately 2 h in order to remove any adsorbed moisture or gasses. For the calculation of the particle size, the bulk density of anatase was used ($3.895 \cdot 10^3 \text{ kg/m}^3$).

3.4.3 Transmission Electron Microscopy (TEM)

Transmission electron microscopy is a technique which is widely used for obtaining information on particle morphology, size, structure, structural defects, etc. The sample, which has to be transparent to electrons, is exposed to an electron beam which interacts strongly with the atoms by elastic and inelastic scattering. The electron intensity distribution behind the specimen is imaged with a lens system onto a fluorescent screen. The image can be recorded by direct exposure of a photographic emulsion or an image plate inside the vacuum, or digitally via a fluorescent screen coupled by a fiber-optic plate to a CCD camera [Reimer and Kohl 2008].

In this work, a TEM instrument was used to determine the particle size and size distribution of TiO₂ nanoparticles. For that purpose the thermophoretic (in-situ) particle deposition on Cu grids with carbon film or sample preparation by powder deposition after dispersing in 2-propanol was used. The measurement were carried out by a Philips Tecnai F20 Super Twin microscope equipped with field emission electron gun with maximal accelerating voltage of 200 kV and 0.23 nm point resolution. Images were recorded using the Gatan Multiscan CCD (794IF) camera. The particle size distribution is obtained by a log-normal fit (Eq. 3.16) of binned data obtained from the TEM images by measuring the size of several hundred particles.

In order to study the cobalt distribution in Co-doped ZnO, energy filtered TEM (EFTEM) was used. This technique uses only electrons of particular kinetic energies (here for cobalt) which are inelastically scattered from the sample to form the image or diffraction pattern.

3.4.4 Photon Correlation Spectroscopy (PCS)

Photon correlation spectroscopy (PCS), also known as dynamic light scattering (DLS), is a technique used to determine the size of particles in a dispersion. Particles in a liquid undergo random Brownian motion due to multiple collisions with

the thermally driven molecules of the liquid that surrounds the particles [Tscharnauter 2000]. The scattered light (e.g. laser) intensity from these diffusing particles will fluctuate in time, thus carrying information about the diffusion coefficient of the particles, D according to the Stokes-Einstein equation:

$$D = \frac{k_B \cdot T}{3 \cdot \pi \cdot \eta(T) \cdot d_h} \quad (3.22)$$

where k_B is the Boltzmann constant, T is the absolute temperature, $\eta(T)$ is the viscosity of the dispersing medium, and d_h is the hydrodynamic diameter.

The size of TiO₂ nanoparticles was measured using a Zetasizer Nano S (Malvern) equipped with green laser ($\lambda = 532$ nm). Prior to the measurement 12.5 mg nanoparticles were dispersed in 25 ml of 0.01 M HCl (pH \approx 2) and ultrasonically treated for 15 min using ultrasonic horn (Hielscher UP200S, 200W, 24 kHz) with sonotrode tip of 7 mm diameter operating at an amplitude of 65 % and a duty cycle of 70 %.

3.4.5 Atomic Absorption Spectroscopy (AAS)

Atomic absorption spectroscopy is a technique for determining the concentration of a particular metal element within a sample. The sample solution is sprayed into a flame and during the combustion, atoms of the element of interest in the sample are reduced to free, unexcited ground state atoms, which absorb light (from a light source) at characteristic wavelengths. The analyte concentration can be related to the amount of light absorbed by the sample according the Lambert-Beer's law [Kuhn and Försterling 2000]:

$$I = I_0 \cdot e^{-\varepsilon \cdot c \cdot l} \quad (3.23)$$

where I and I_0 is the incoming and absorbed light intensities, respectively, ε is the absorption coefficient, c is the concentration of the analyte element, and l is the length of the absorption path. Direct application of the Lambert-Beer's law is difficult due to variations in the atomization efficiency from the sample, and non-uniformity of concentration and path length of analyte atoms. Concentration measurements are usually determined from working curve after calibrating the instrument with standards of known concentration.

In this work, the AAS is used to determine the Co concentration in Co-doped ZnO nanoparticles. The measurement was carried out using a Thermo Scientific Atomic Absorption Spectrometer (M Series).

3.4.6 Ultraviolet-Visible Spectroscopy (UV-Vis)

Ultraviolet-visible spectroscopy is a method which measures how much of the light in ultraviolet ($\lambda = 10$ –380 nm) and visible ($\lambda = 380$ –780 nm) region is absorbed by atoms or molecules. In some molecules and atoms, photons of UV and

visible light have enough energy to cause electron transitions from a lower energy level to the higher one. These transitions result in absorbance bands at wavelengths highly characteristic of the difference in energy levels of the absorbing species [Owen 2000]. Transition metal ions have electronic energy levels that cause absorption in of 400–700 nm in the visible region.

In this work, the UV-Vis spectroscopy was used as a qualitative method to obtain information about environment of Co atoms in Co-doped nanoparticles based on absorption bands in the visible region due to $d-d$ electron transitions. UV-Vis spectra, in the wavelength region from 200–900 nm, were obtained using Varian Cary 400 Scan spectrometer. Powder samples were placed in a 3 mm sampling cup so the surface of the sample is flat. A baseline correction was performed, prior to the measurement, using a Teflon sample.

3.4.7 X-ray Absorption Spectroscopy (XANES and EXAFS)

X-ray absorption spectroscopy (XAS) relies on photoelectron promotion upon absorption of X-ray photon. The wave nature of the photoelectron is used to determine local structures around specific atomic species in both ordered (crystalline) and disordered (amorphous) materials. The measurements are performed using high energy X-rays, which are generated by synchrotron radiation sources. Usually, the absorption of the sample is measured by monitoring the incoming (I_0) and transmitted (I) X-ray intensities [Koningsberger et al. 2000]:

$$I = I_0 \cdot e^{-\mu(E)x} \quad (3.24)$$

where μ is the absorption coefficient and x is the sample thickness.

The high energy X-rays excites a deep core electron into a state above the Fermi energy (Fig. 3.12a). The generated photoelectron propagates as a wave and scatters off surrounding atoms (Fig. 3.12b) producing a backscattered wave. The core electron promotion to the continuum causes a sharp rise in the absorption known as absorption edge (Fig. 3.13). The interference between the outgoing

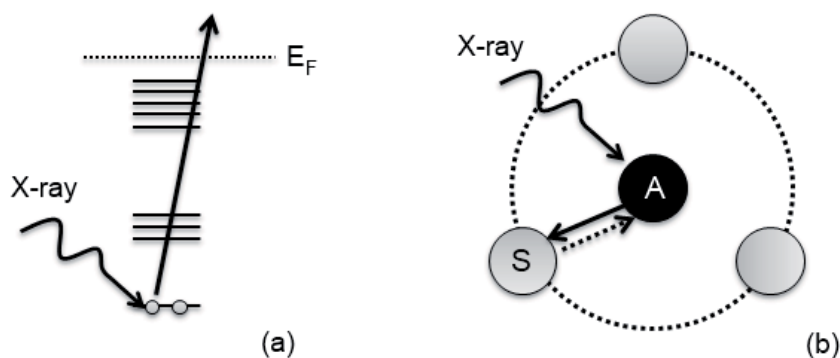


Fig. 3.12. The schematic representation of the photoelectric effect (a) and the interference between the outgoing wave and the backscattered waves (b) (A – absorber, S – scatterer) [reproduced from Koningsberger et al. 2000]

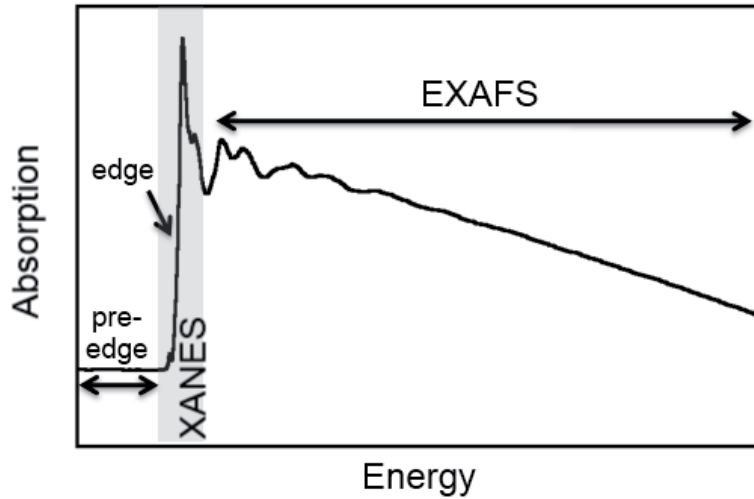


Fig. 3.13. XAS spectrum with basic features: pre-edge, edge, XANES and EXAFS region

wave and the backscattered wave is the source of the oscillatory structure in X-ray absorption spectrum. Two regions are often separated: (i) the X-ray absorption near-edge structure (XANES) typically 100 eV beyond the absorption edge and (ii) the extended X-ray absorption fine structure (EXAFS) which extends up to 400-2000 eV from the edge [Aksenov et al. 2001]. The XANES is strongly sensitive to the oxidation state and coordination chemistry (e.g., octahedral, tetrahedral coordination) of the absorbing atom, while the EXAFS is used to determine coordination number, interatomic distance (distance between the absorbing atom and the backscattering atoms), and Debye-Waller factor [Newville 2004]. The signals, which can be sometimes observed in the pre-edge region, are usually caused by the electron transitions from the core level to the higher unfilled or half-filled orbitals. For the K -edge of a first row transition metals, this is caused by $1s \rightarrow 3d$ transitions, and are observed for every metal that has an open $3d$ shell [Penner-Hahn and Ni 2004].

The EXAFS oscillatory part can be described by the following equation [Stern 1988]:

$$\chi(k) = \sum_j \frac{N_j f_j(k)}{kR_j^2} e^{-2k^2\sigma_j^2} \cdot e^{-2R_j/\lambda} \cdot \sin(2kR_j + \delta_j(k)) \quad (3.25)$$

where $f_j(k)$ and $\delta_j(k)$ are the backscattering amplitude and the phase-shift, respectively (both properties of the atoms neighboring the excited atom, j), N_j is the coordination number (the number of neighboring atoms), R_j is the distance to the neighboring atom, λ is the mean free path of photoelectron, $e^{-2k^2\sigma_j^2}$ is the Debye-Waller factor with σ_j^2 as the disorder in the interatomic distance and k as the wave number of the photoelectron, which is defined as:

$$k = \sqrt{\frac{2m \cdot (E - E_0)}{\hbar^2}} \quad (3.26)$$

where m is electron mass, E is the X-ray energy, E_0 is the absorption edge energy, and \hbar is the Planck's constant.

Figure 3.14a shows the EXAFS signal, $\chi(k)$ as a function of the wave number, k . The Fourier transformation of the EXAFS signal results in a radial distribution function, Fig. 3.14b. The Fourier transformation, $FT(R)$ is defined by [Koningsberger et al. 2000]:

$$FT(R) = \frac{1}{\sqrt{2\pi}} \int_{k_{\min}}^{k_{\max}} k^n \chi(k) e^{i2kR} dk \quad (3.27)$$

where R is the distance from the absorber atom.

The intensity of the X-ray beam is measured before and after passing through the sample. Fluorescence mode is used when the sample is dilute.

In order to investigate the local structure of Co in Co-doped ZnO nanoparticles, X-ray absorption spectra were measured at the Co K -edge and Zn K -edge using beamline 12.BM.B at the Advanced Photon Source (APS) at Argonne National Laboratory. The beamline 12.BM.B is a bending magnet beamline with an energy range of 7.5–28 keV. The absorption of the samples is optimized by diluting appropriate amounts of sample homogeneously into starch powder and pressing a pellet (13 mm diameter) uniaxially (25 kN/10 min). Transmission and fluorescence spectra are collected at ambient temperature. The spectra of commercial CoO and Co₃O₄ powders (Sigma Aldrich) are also recorded as a reference. The XAFS data were analyzed using the program *xafsX* [Winterer 1997]. The extracted EXAFS data are then analyzed by the Reverse Monte Carlo Method (RMC) using the *rmcxas* program [Winterer 2000]. In order to eliminate multiple scattering, the EXAFS data are filtered by Fourier back transformation from R -space between 0.5 and 3.5 Å. Initial atom configurations are generated from results of the Rietveld refinements of XRD data of the corresponding samples and contain an appropriate number of Co atoms. Zn and Co EXAFS spectra are analyzed simultaneously using a single atomic configuration where an appropriate number of Zn atoms are substitutionally replaced in a wurtzite lattice by Co atoms. Theoretical amplitude and phase functions for RMC analysis are obtained by FEFF 8 simulations [Ankudinov et al. 1998].

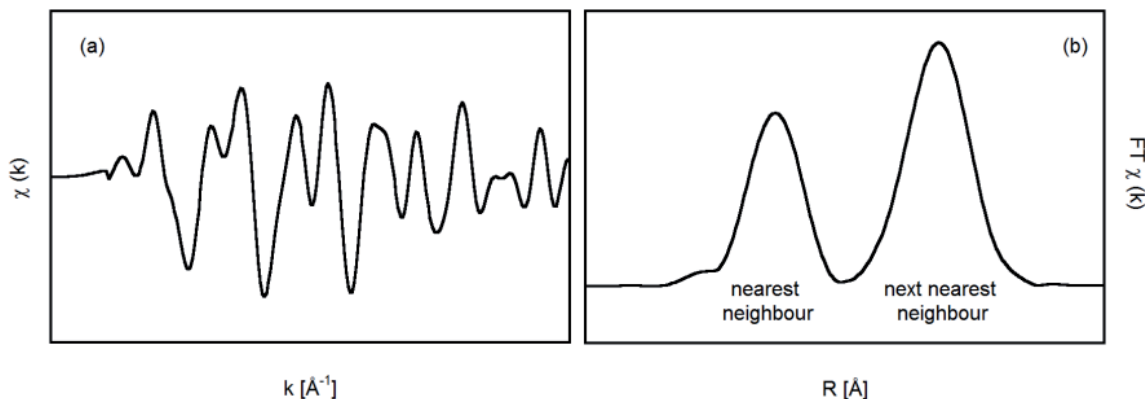


Fig. 3.14. The EXAFS spectrum in k -space (a) and its Fourier transform to R -space (b)

3.4.8 Superconducting Quantum Interference Device (SQUID) Measurements

A superconducting quantum interference device (SQUID) measures a change in a magnetic flux. These changes can be used to measure any physical quantity related to flux (magnetic field, current, voltage, magnetic susceptibility, etc.) [Kleiner et al. 2004]. The measurement is performed by moving the sample through the superconducting detection coils which are located outside the sample chamber and at the center of magnet. As the sample moves through the coil, the magnetic moment of the sample induces an electric current in the detection coil. The variations in the current in the detection coil produce corresponding variations in the SQUID output voltage which are proportional to the magnetic moment of sample [McElfriesh 1994].

In this work, the magnetization measurements were carried out using a superconducting quantum interference device magnetometer (MPMS XL, Quantum Design, Inc.). A plastic capsule filled with powder samples (between 5 and 20 mg) was placed in a polymer straw and the SQUID sample chamber. Temperature-dependent magnetization was measured in external magnetic fields of 200 Oe between 5 and 320 K. For all samples the magnetization was measured in both zero-field-cooled (ZFC) and field-cooled (FC) regime. Field-dependent measurement was carried out at 5 and 300 K varying the fields from 0 kOe up to 50 kOe and back.

The specific magnetization, σ (emu/g) was calculated from the magnetic moment, μ (emu) and the mass of sample, w (g) [Cullity and Graham 2009]:

$$\sigma = \frac{\mu}{w} \quad (3.28)$$

The molar magnetic susceptibility, χ (emu/molOe) is calculated according to:

$$\chi = \frac{\sigma}{H} \cdot M \quad (3.29)$$

where σ is the specific magnetization (emu/g), H is the magnetic field strength (Oe) and M is the molecular weight (g/mol).

4 Results and Discussion

4.1 Particle Size and Degree of Agglomeration

The time-temperature profile is the most important process parameter in chemical vapor synthesis which determines particle characteristics. In order to study the influence of time-temperature profiles in the CVS reactor on particle generation and their characteristics (e.g. particle size, degree of agglomeration - number of primary particles in an agglomerate, crystallinity) the CVSSIN model was used to simulate TiO₂ particle formation and results are compared to the experimental one.

4.1.1 Results of the CVSSIN Model

Initial CVSSIN simulations were performed for three types of hypothetical temperature profiles: (i) 'flat' with a broad zone of constant temperature (Fig. 4.1), (ii) 'down' with a steep decrease of temperature and (iii) 'up' with a steep increase of temperature (Fig. 4.2). Results for the 'flat' temperature configuration revealed that a simple increase of the wall temperature does not only increase the gas temperature in the reactor but changes the time-temperature profile completely (Fig. 4.1a), and as the conversion of the TTIP precursor into TiO₂, CO₂ and H₂O is a highly exothermic reaction, a hot spot in the reactor develops. In case of the 'flat' configuration, the difference of the maximum gas temperature to the wall temperature decreases with increasing temperature and the position of the hot spot moves closer to the reactor entrance (Fig. 4.1a). The degree of agglomeration displays a minimum after a maximum which is formed due to the particle nucleation burst by chemical reaction (Fig. 4.1b). At that point (minimum, see inset in Fig. 4.1b as an example) the gas temperatures are sufficiently high to completely coalesce the very small primary particles inside of the agglomerates. However, at the reactor exit, where the particles are collected the degree of agglomeration increases and shows a maximum for particles produced at 873 K (Fig. 4.1b). At the lowest process temperature the sintering kinetics of the primary particles is too slow, while at higher process temperatures the sintering kinetics is enhanced and coalescence is possible. The 'up' temperature profile configuration (Fig. 4.2a) leads to much lower degree of agglomeration in comparison to the 'down' profile due to the faster cooling rates at the reactor exit (Fig. 4.2b).

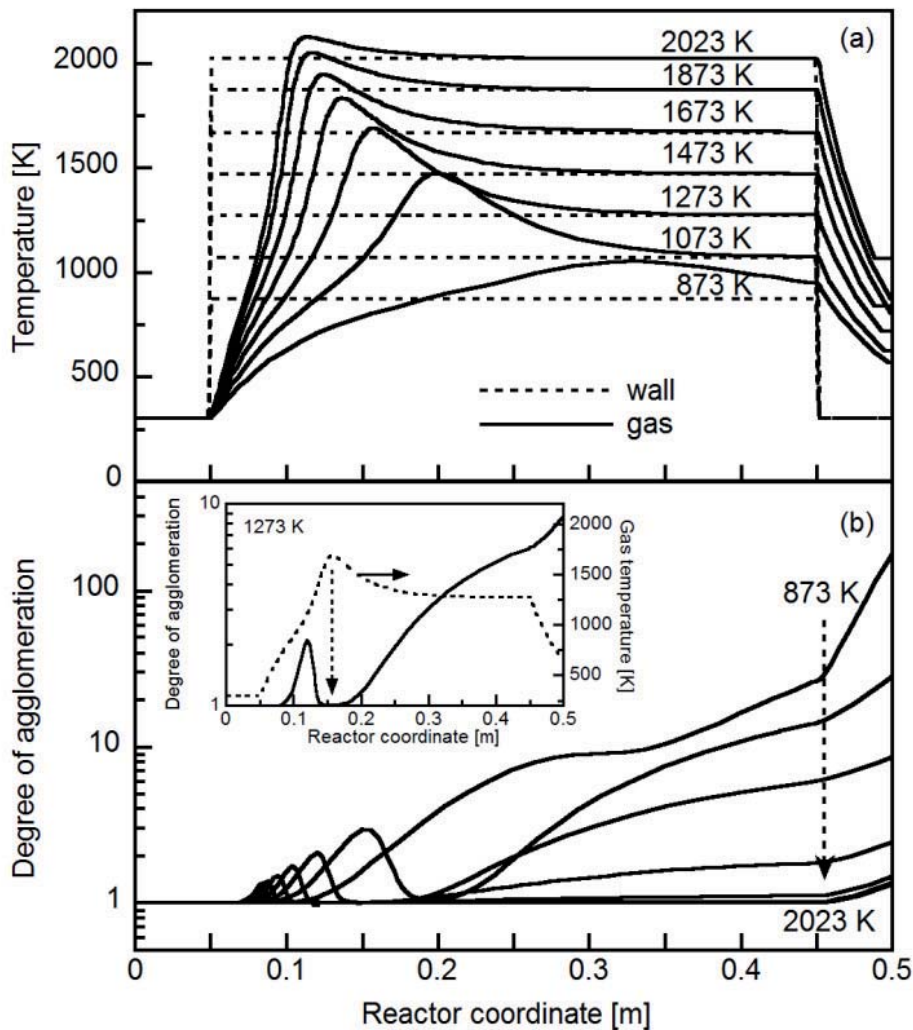


Fig. 4.1. Gas temperature profiles (full lines) as a function of reactor coordinate for hypothetical ‘flat’ wall temperature profile (dashed lines) (a) and corresponding degree of agglomeration (b) (inset: Change of the degree of agglomeration and gas temperature inside of the reactor when maximum wall temperature is set to 1273 K)

These preliminary results of the CVSSIN model were the base for a detailed systematic investigation where the wall temperatures were measured and used as an input data for more realistic simulation. Therefore, the reactor length is extended from 0.5 to 1 m, due to the natural heat distribution along the reactor tube. Figures 4.3 and 4.4 display ‘flat’ time-temperature profiles as a result of the simulation. As it can be seen the wall temperature profiles, as well as the gas temperature profiles, are different from the profiles in preliminary simulation (Fig. 4.1a), but the hot spot is still developed close to the reactor entrance. The total residence time (Fig. 4.5) in the reactor decreases and the cooling rates increase with increasing wall temperature as it can be seen from the slope of t - T -profile (Fig. 4.4) at the reactor exit. As the temperature increases the primary and agglomerate particle size increases. The agglomerate size reaches the maximum at 1273 K (Fig. 4.6). Above these temperatures, due to faster chemical reaction rate, the number of smaller particles increases and the sintering enhances leading to a decrease of ag-

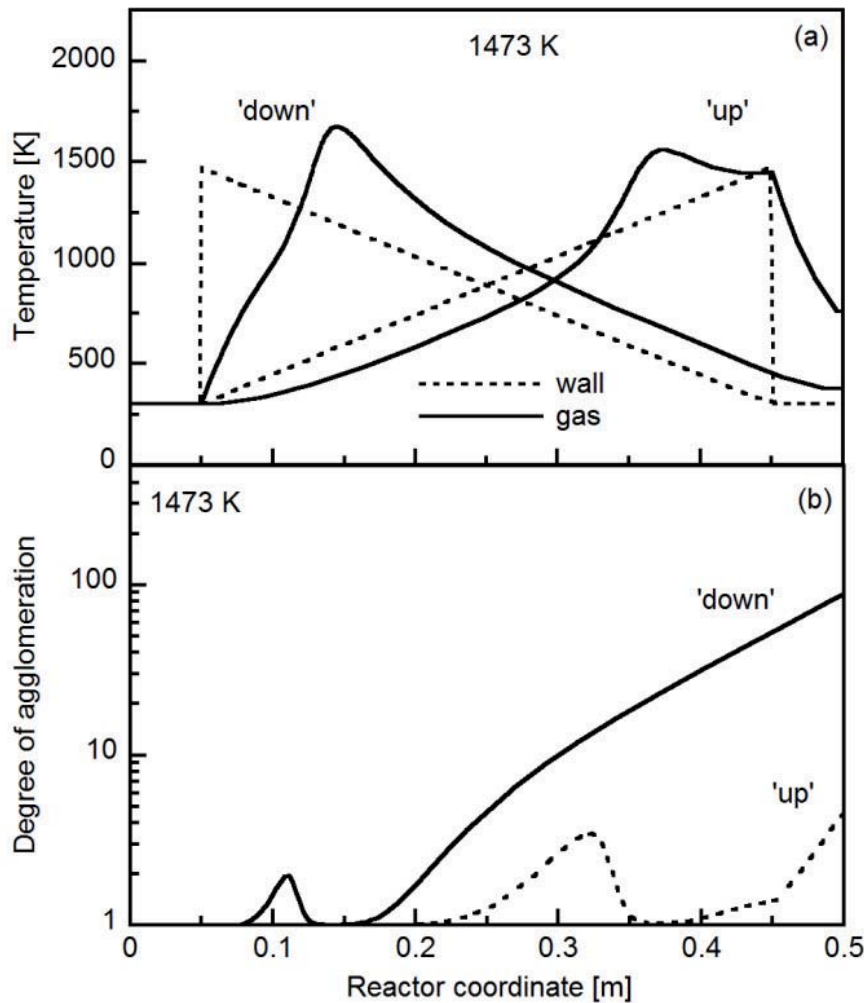


Fig. 4.2. Gas temperature profiles (full lines) as a function of reactor coordinate for hypothetical 'down' and 'up' wall temperature profiles (dashed lines) (a) and corresponding degree of agglomeration (b)

glomerate size. As a result a significant decrease of the degree of agglomeration at highest process temperature is observed, Fig. 4.7 and 4.8. Figure 4.9a shows distribution of temperature along the reactor with 'down' and 'up' temperature profiles when the maximum temperature is set to 1473 K (as an example). From these results it can be seen that the gas temperatures are again quite different from the wall temperature. Hot spots are also pronounced, and in both cases ('down' and 'up') they are developed close to the reactor entrance (at 0.20 and 0.30 m, respectively) which is contrary to the preliminary simulation (Fig. 4.2b) where hot spots are formed close to the reactor entrance ('down') or exit ('up'). This difference arises from fact that real wall temperature profiles are broader, or in case of 'up' temperature profile less steep than it was assumed in the preliminary simulation (Fig. 4.2). The degree of agglomeration (Fig. 4.9b) is considerably smaller for 'up' temperature profile due to a faster quenching rate, but in comparison to 'flat' temperature profile (Fig. 4.10), the degree of agglomeration for 'up' temperature profile is just slightly smaller. This is again correlated with a broader wall tempera-

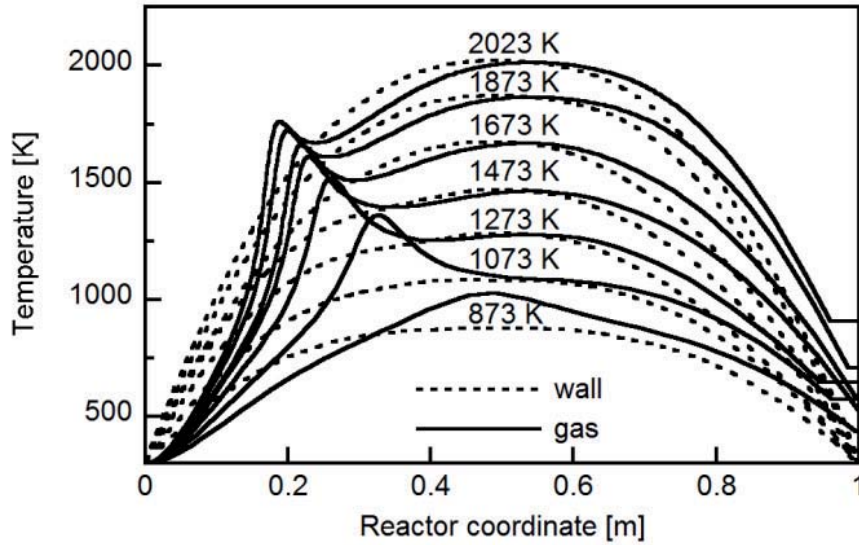


Fig. 4.3. Gas temperature profiles (full lines) for ‘flat’ wall temperature profiles (dashed lines) as a function of the reactor coordinate for experimentally measured reactor wall temperatures

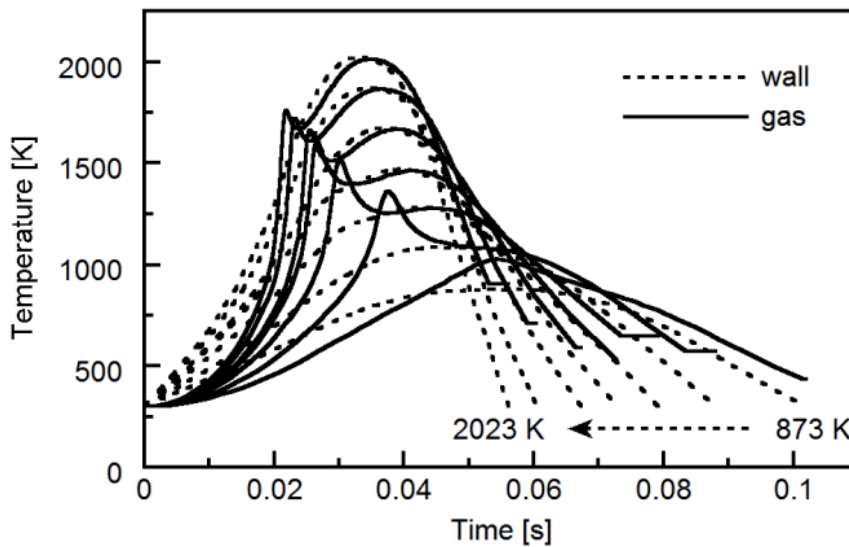


Fig. 4.4. Gas temperature profiles (full lines) ‘flat’ wall temperature profiles (dashed lines) as a function of the reaction time for experimentally measured reactor wall temperatures (dashed lines)

ture profile, which does not contribute significantly to an increase of the cooling rate as it was expected from the preliminary results. Therefore, from the results of the simulations, it can be expected that the lowest degree of agglomeration could be achieved using a highest process (wall) temperature and ‘flat’ or ‘up’ time-temperature profiles.

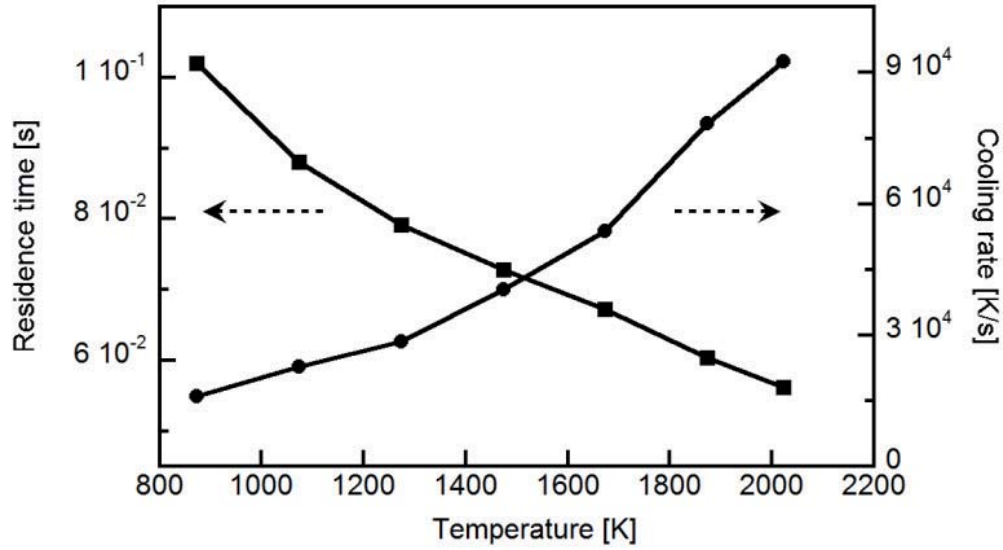


Fig. 4.5. Residence time and maximum cooling rate (according to the CVSSIN model) in the CVS reactor as a function of the maximum wall temperature for ‘flat’ time-temperature profiles

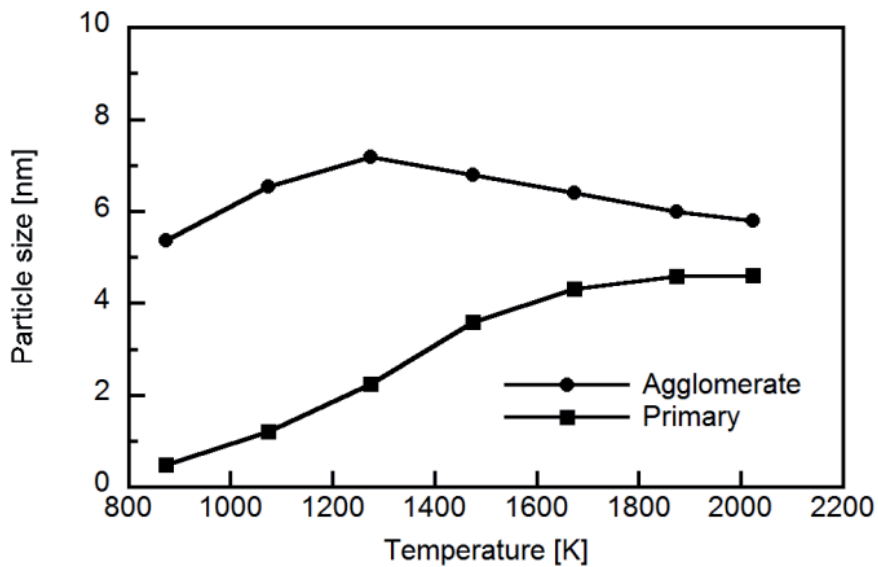


Fig. 4.6. Primary and agglomerate particle size (according to the CVSSIN model) as a function of the maximum wall temperature for ‘flat’ time-temperature profiles

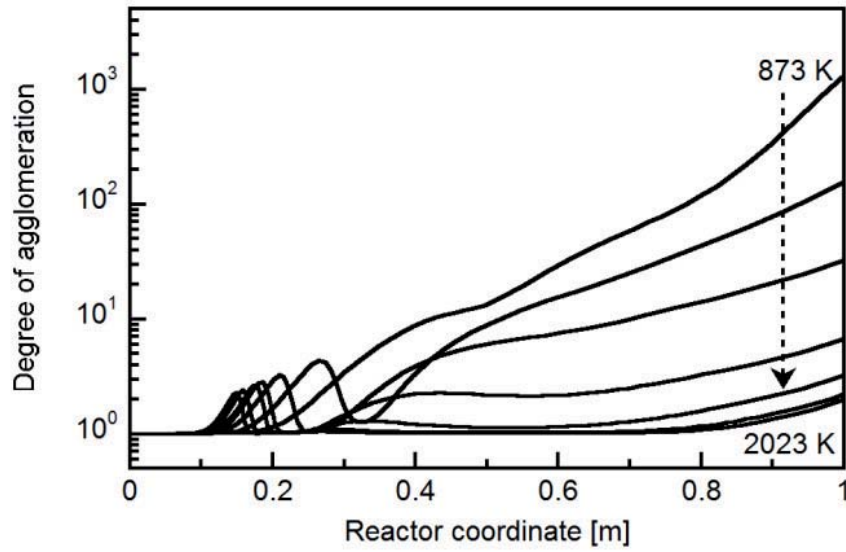


Fig. 4.7. Degree of agglomeration (according to the CVSSIN model) as a function of reactor coordinate for the ‘flat’ time-temperature profiles

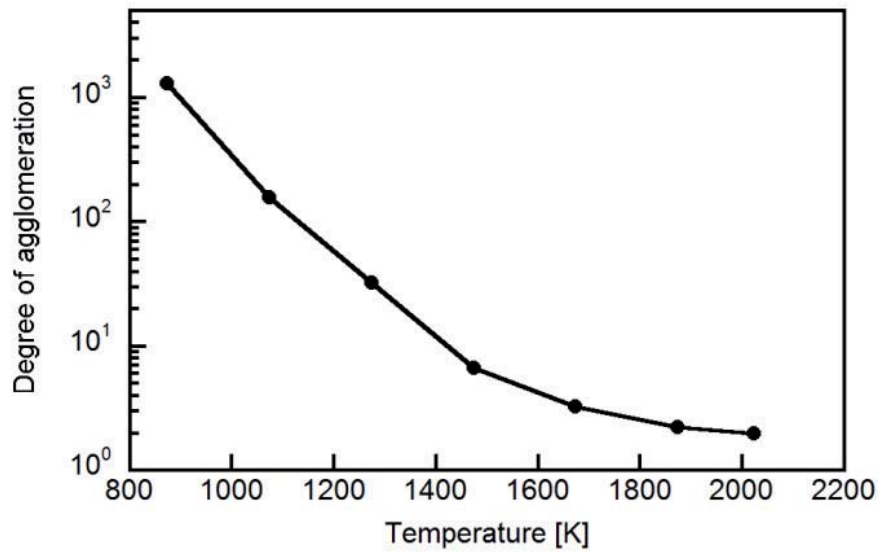


Fig. 4.8. Degree of agglomeration (according to the CVSSIN model) as a function of the reactor wall temperature for the ‘flat’ time-temperature profiles

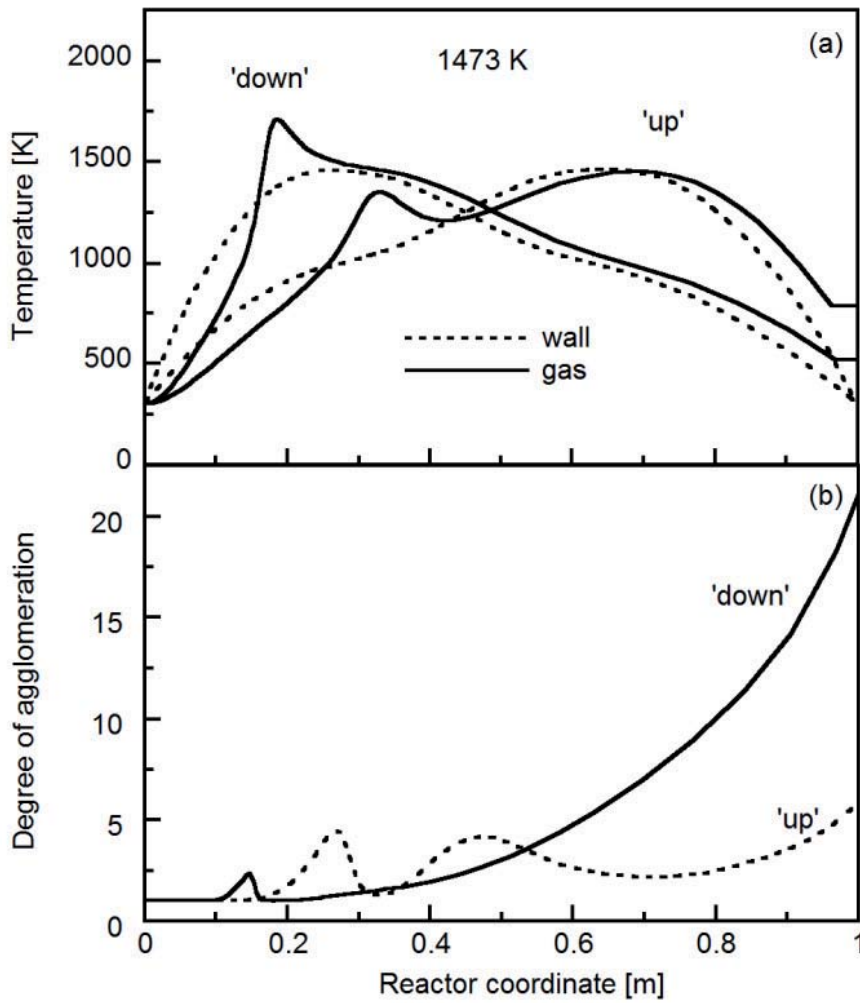


Fig. 4.9. Gas temperature profiles (full lines) (a) and degree of agglomeration (b) in a CVS reactor for 'up' and 'down' wall temperature profiles (dashed lines)

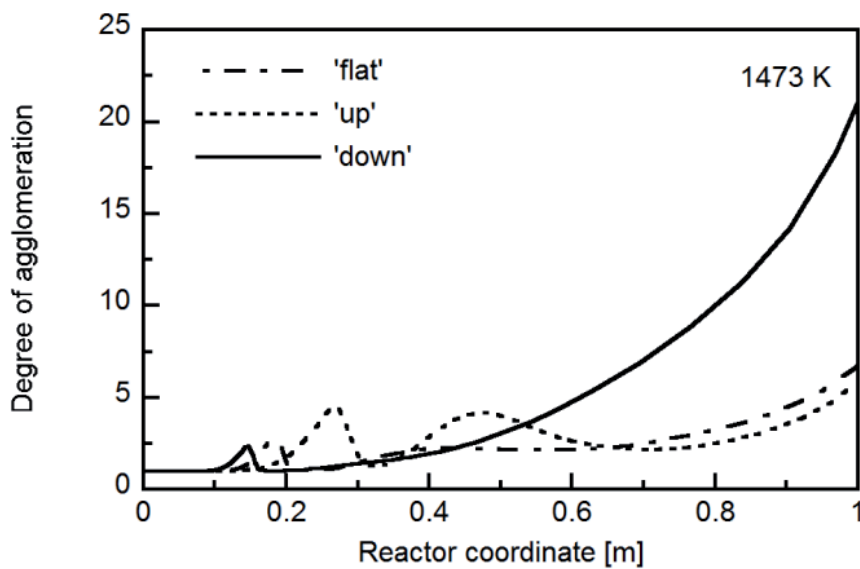


Fig. 4.10. Comparison of the degree of agglomeration for 'up' and 'down' time-temperature profiles with the degree of agglomeration from 'flat' time-temperature profile

4.1.2 The Experimental Results

In order to verify the results of CVSSIN model, TiO₂ particles were synthesized and characterized. Experimental results are discussed and compared with the results obtained from CVSSIN model.

4.1.2.1 The 'Flat' Time-Temperature Profiles

X-ray diffraction patterns of as-synthesized TiO₂ powders (Fig. 4.11) show strong reflections which can be assigned to the anatase phase. In the powders synthesized above 1273 K minute quantities of the rutile phase were identified, and in powders synthesized above 1473 K, besides rutile, brookite was found as well (Fig. 4.12). Rietveld analysis of the XRD data shows very good agreement between experiment and refinement (Fig. 4.13). The Rietveld analysis was also used for the determination of phase composition (Table 4.1), crystallite size and microstrain. Powders synthesized at 873 K, consisting of pure anatase phase, have the smallest crystallite size (Fig. 4.14) as it is expected from the CVSSIN model. Generally, the anatase crystallite size increases with process temperature, and it ranges from about 2 nm (873 K) up to 11 nm (2023 K). Zhang and Banfield [Zhang and Banfield 1998] presume that the anatase to rutile phase transformation occurs due to coarsening of anatase particles. In their work, the transformation was found for particles larger than 14 nm. As it can be seen from the results presented here, the

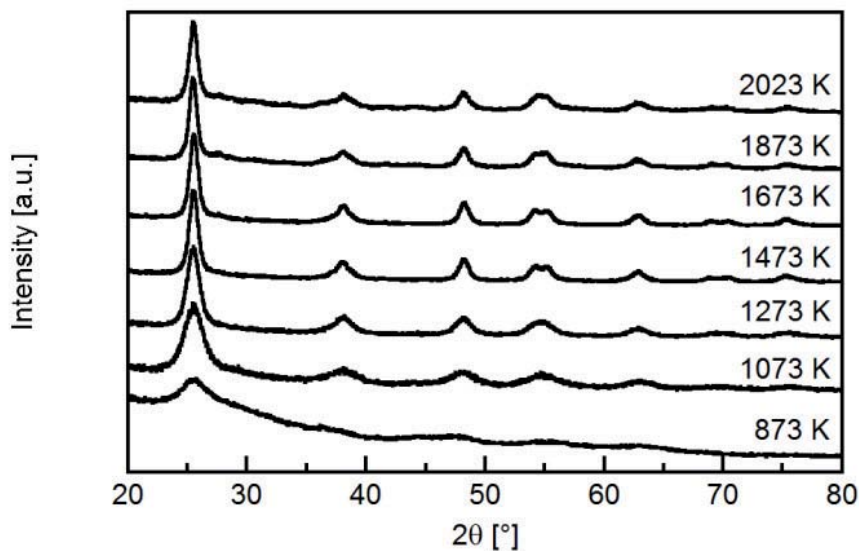


Fig. 4.11. XRD pattern of as-synthesized TiO₂ nanoparticles using the 'flat' time-temperature profile

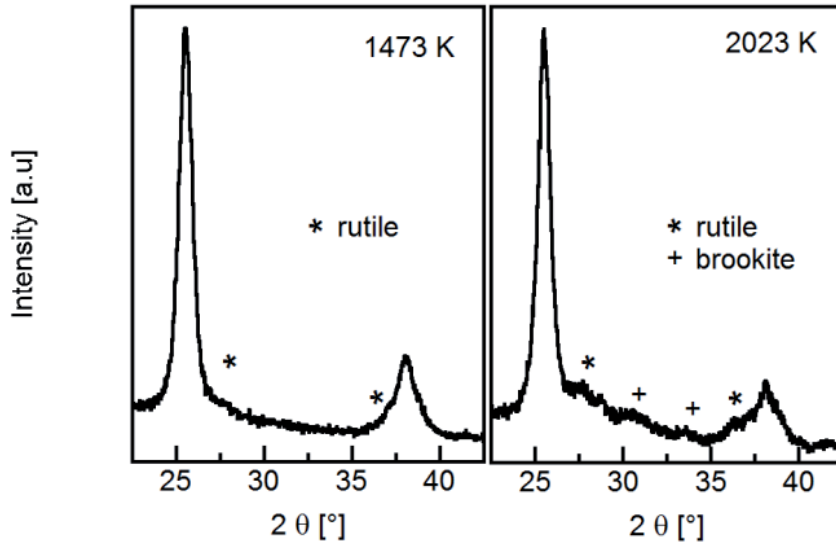


Fig. 4.12. Rutile and brookite phase formation

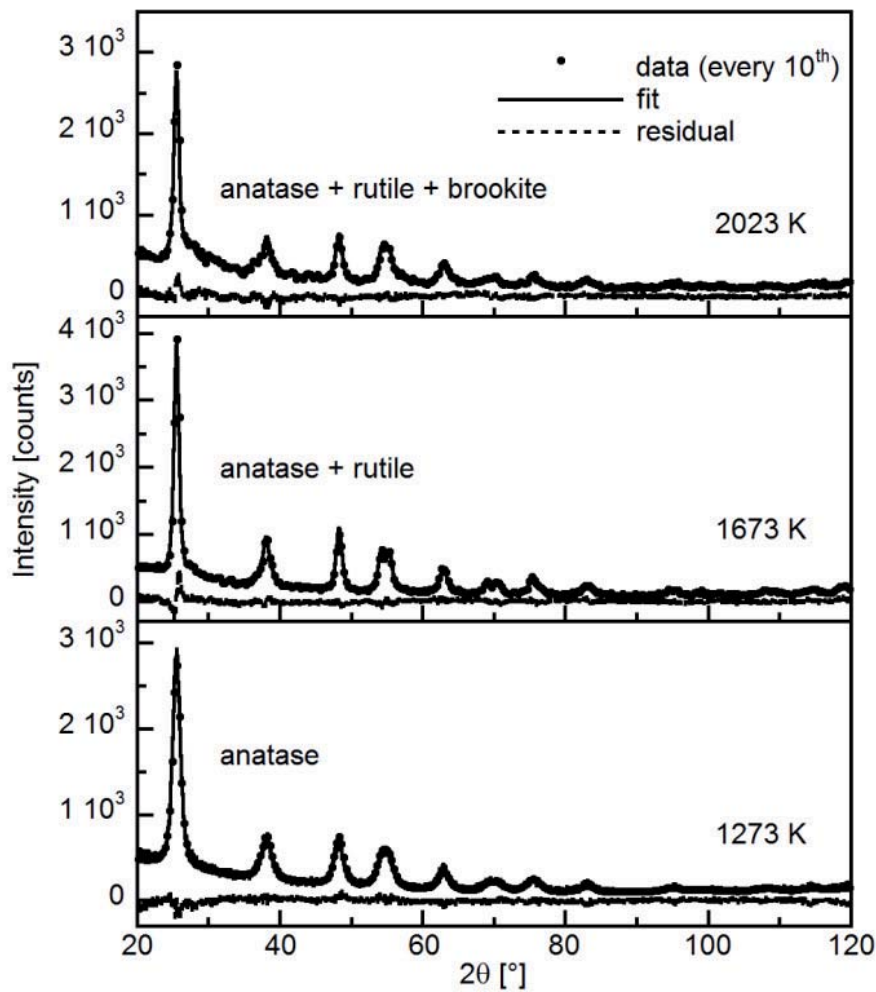


Fig. 4.13. XRD patterns with the Rietveld refinement of TiO₂ particles showing a presence of different phases: 1273 K (anatase), 1673 K (anatase and rutile) and 2023 K (anatase, rutile and brookite)

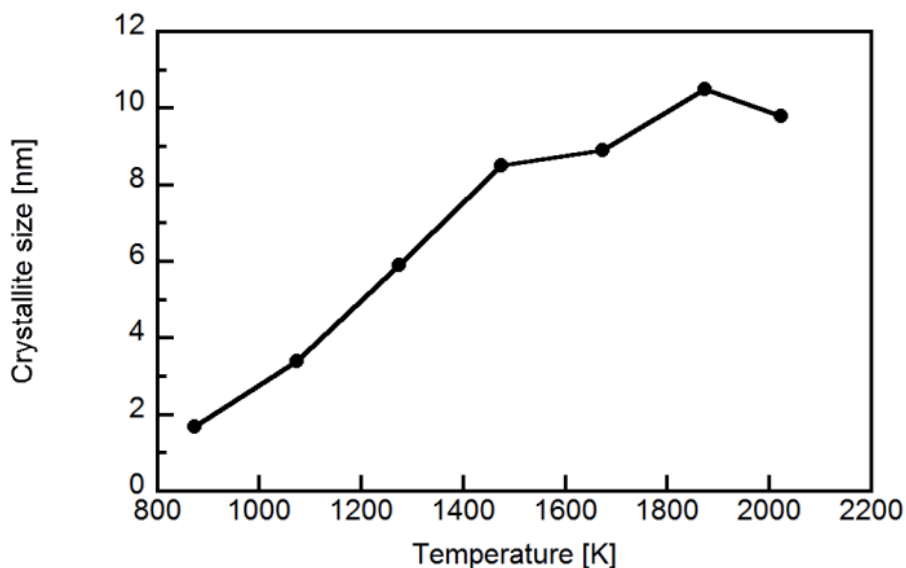


Fig. 4.14. Crystallite size of TiO₂ (anatase) nanoparticles as a function of process temperature (the error bars are smaller than the symbols)

Table 4.1. Phase composition and crystallite size of as-synthesized TiO₂ particles ('flat' time-temperature profile) obtained from Rietveld refinement of the XRD data

Temperature [K]	Phase composition [vol.%]			Crystallite size [nm]		
	Anatase	Rutile	Brookite	Anatase	Rutile	Brookite
873	100	-	-	1.7(0)	-	-
1073	100	-	-	3.4(1)	-	-
1273	100	-	-	5.9(1)	-	-
1473	96	4	-	8.5(1)	8.5(8)	-
1673	94	6	-	8.9(1)	7(1)	-
1873	63	11	26	10.5(2)	7.3(3)	3.2(1)
2023	60	11	29	9.8(2)	7.4(4)	4.6(4)

rutile was observed even in powders comprising of particles smaller than 14 nm (Table 4.1). The size 'border' for the anatase to rutile phase transformation, stated by Zhang and Banfield [Zhang and Banfield 1998] does not hold here. Probably, not only the size effect but also other parameters like the process conditions, play a role in this phase transformation. It has been shown for zirconia [Winterer 2002] that the quenching rate influences the phase composition more than coarsening of the particles. At 1473 K, the Rietveld analysis showed that the rutile crystallite size is same as that of anatase. As the crystallite size of rutile at higher temperatures (> 1473 K) is smaller than at 1473 K, the identical size of rutile and anatase crystallites is rather correlated with lower accuracy of Rietveld refinement using the MAUD software for low phase content (at 1473 K, only 4 % of rutile, Table 4.1) than with meaningful physical origin. This assumption is later supported by TEM imaging.

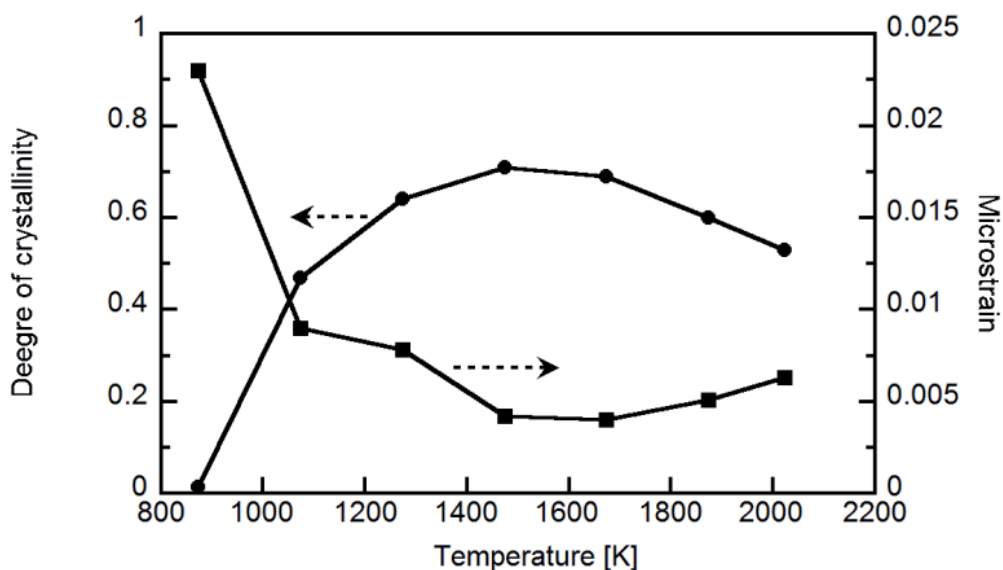


Fig. 4.15. Degree of crystallinity (Eq. 3.5) and microstrain of TiO_2 (anatase) nanoparticles as a function of process temperature (the error bars are smaller than the symbols)

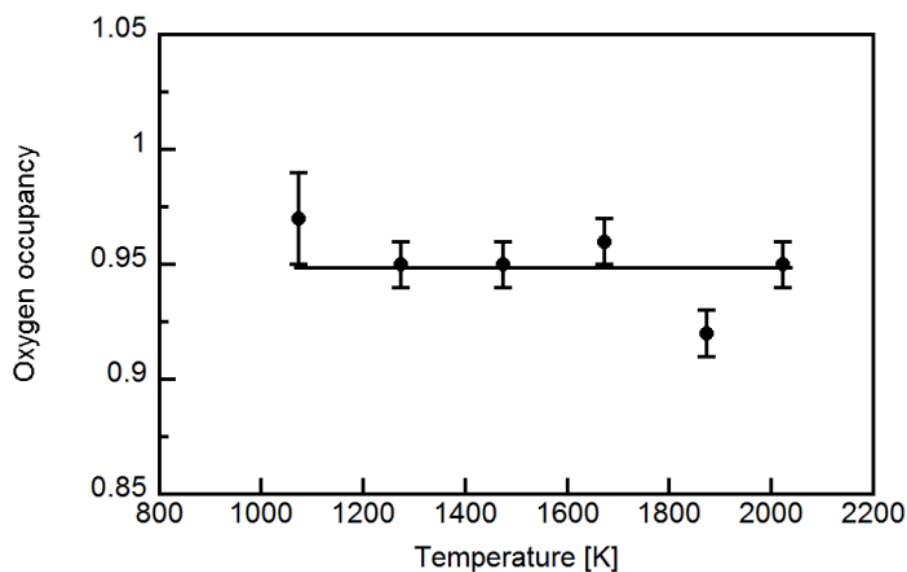


Fig. 4.16. Oxygen occupancy in the TiO_2 powders from the Rietveld refinement of the XRD data

In addition to the phase composition, the degree of crystallinity is important, as it plays a significant role in determining properties of materials. Figure 4.15 shows dependence of degree of crystallinity on process temperature, and it can be seen that crystallinity of particles increases with increasing a process temperature up to 1473 K, after which it shows slight decrease. One would expect that at these high temperatures the oxygen deficiency would be possible source for decrease of crystallinity (increase of microstrain). But results of refinement of the oxygen occupation factor (Rietveld refinement of the XRD data) revealed that the oxygen occupation factor does not change with temperature (Fig. 4.16). This result excludes the oxygen deficiency as a possible source of decrease of crystallinity. On the oth-

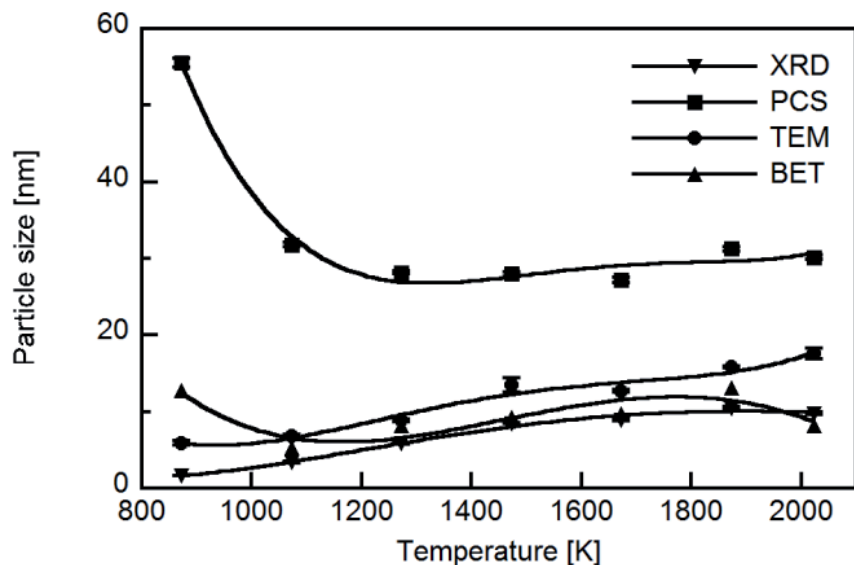


Fig. 4.17. Particle size determined using different techniques as a function of temperature (all values, with exception of BET, are volume weighted)

er hand, as it was shown earlier (e.g. Fig. 4.13, Table 4.1), the rutile phase forms at temperatures ≥ 1473 K, while from 1673 K brookite phase appears as well, which may be the source for the slight decrease of crystallinity above these temperature as well as increase of microstrain (Fig. 4.15). As it will be discussed later, the rutile phase most probably forms by surface nucleation on the already existing anatase nanoparticles, while the brookite phase forms presumably by atom rearrangement (solid state diffusion) inside of anatase particles. This all may lead to the formation of defects and consequently to the decrease of the crystallinity. Even thou the temperatures are sufficiently high for annealing of the defects, time may not be long enough.

In order to determine the degree of agglomeration, particle size was measured (or obtained) using different characterization methods: XRD, TEM, PCS and BET. As different characterization techniques measure different type of particles size with different weights in order to be comparable, the number weighted particle sizes (d_n) obtained from TEM image analysis was converted into the volume weighted particle size (d_v) using Hatch-Choate equation [Hinds 1999]:

$$d_v = d_n \cdot \exp\left(3 \cdot \ln^2 \sigma_g\right) \quad (4.1)$$

where σ_g is the geometric standard deviation obtain from the log-normal fit of the TEM data. Particle sizes calculated from the specific surface are kept as area weighted values because the standard deviation, necessary for conversion into the volume weighted values, is unknown. Particle sizes determined by photon correlation spectroscopy (PCS, volume weighted) are a measure of the size of agglomerate particles formed under the conditions of the aqueous colloidal system. Figure 4.18 shows the comparison of the particle size determined using these methods. The cubed ratio of the particle size determined from PCS / TEM / BET to the primary particle size obtained from XRD is a measure for the degree of agglomera-

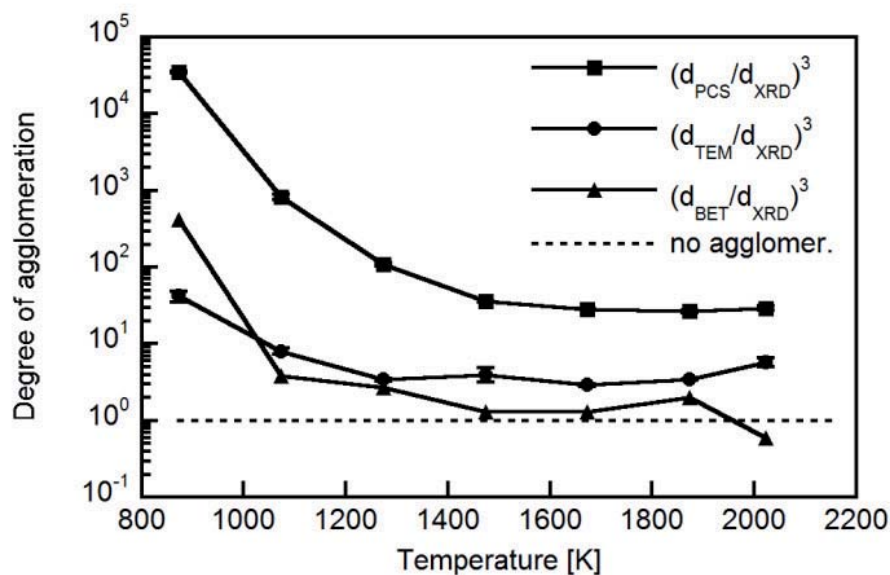


Fig. 4.18. Degree of agglomeration as a function of temperature calculated from values of particle size obtained from different measurement techniques

tion (Fig. 4.18). Clearly, at the highest process temperature (2023 K) the lowest degree of agglomeration is achieved as it was predicted by CVSSIN model (see Fig. 4.8). Grass et al. [Grass et al. 2006] investigated the degree and strength of agglomeration when TiO_2 is formed in flames. They found that non-agglomerated particles can be formed at low precursor flow rates and high quenching rates. Solid state diffusion and the t - T profile are main parameters that have control over the agglomeration. The results presented here are in the agreement with these findings.

HRTEM micrographs of some selected TiO_2 as-synthesized nanoparticles as well as corresponding particle size distributions are summarized in Fig. 4.19. Particles synthesized at lower process temperature are evidently more agglomerated (e.g. Fig 4.19a) than particles synthesized at higher temperatures (e.g. Fig. 4.19d) which is in agreement with results discussed above. Particles synthesized at 1473 K (Fig. 4.19b) show a bimodal size distribution which can be explained by the formation of a second (rutile) phase (see Table 4.1) where smaller particles are most probably rutile particles. The Rietveld refinement of the XRD data for this sample showed that anatase and rutile crystallites have same size, but the TEM images clearly show presence of particles with two different sizes. This supports the earlier assumption that Rietveld refinement has low accuracy in crystallite size determination for lower phase content. In addition, as the XRD is average (volume based) technique, the presence of higher amount of larger crystallites can contribute to the refinement error. As the temperature increases the rutile particles are growing and size distribution becomes again monomodal (Fig. 4.19c). At the highest process temperature (2023 K) due to the formation of brookite phase, the particle size distribution becomes again bimodal, where now the smaller particles are most probably brookite phase (in agreement with XRD, Table 4.1), while anatase and rutile particles contribute to the bigger particle size.

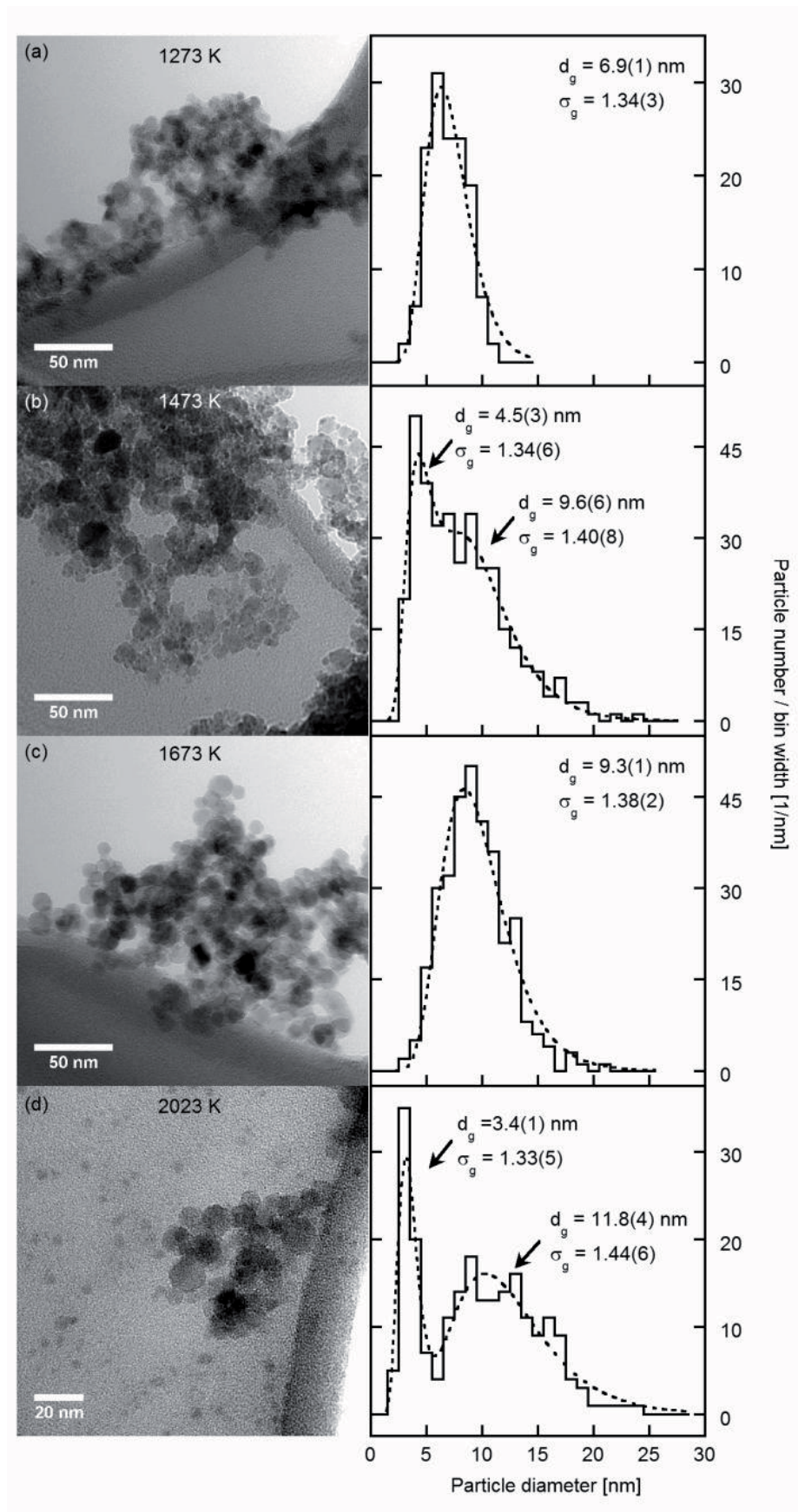


Fig. 4.19. TEM micrographs (left) and corresponding particle size distributions (right) of selected as-synthesized TiO_2 nanoparticles (dashed line - log-normal fit of data)

The mechanism of rutile and brookite formation is widely discussed in the literature. For an overview see for example Chen and Mao [Chen and Mao 2007] or Hanaor and Sorrell [Hanaor and Sorrell 2011]. However, it is still very difficult to draw a final conclusion about the rutile and brookite formation mechanism in the gas phase, because most of the experimental work was carried out by annealing [Gribb and Banfield 1997] or sintering [Liao et al. 1995] TiO_2 (amorphous or anatase) powders at different temperatures for different periods of time (hours) which are far beyond the residence time in the CVS reactor (the order of tens milliseconds). From Fig. 4.19b it is clearly visible that smaller (presumably rutile) particles are ‘sitting’ on the surface of larger ones (presumably anatase). Therefore, at the temperatures above 1473 K the rutile particles are most probably formed by surface nucleation on already existing anatase particles. Zhang et al. [Zhang et al. 2006] reported surface nucleation as a mechanism for rutile formation after annealing amorphous TiO_2 particles. At temperatures above 1873 K the TiO_2 particles additionally contain brookite (Table 4.1). From the TEM image (Fig. 4.19d) it is clearly visible that smaller particles, which are believed to be the brookite according to the XRD data, are well separated from the larger ones (anatase and rutile). According to this surface nucleation seems unlikely as a possible mechanism for brookite formation. A more probable scenario is that due to similar arrangement of atoms in the brookite and anatase crystal lattice, at these high temperatures, the thermal energy is sufficiently high that Ti atoms can rearrange inside of anatase to transform the brookite phase. Therefore, the brookite phase is most likely formed from anatase by solid-state reactions. This mechanism was proposed by Penn and Banfield [Pen and Banfield 1998]. Figure 4.20 shows the mechanism for the rutile and brookite phase formation in case of TiO_2 nanoparticles synthesized in gas phase (this work) based on the TEM images and the XRD analysis. More detailed TEM studies on the CVS grown particles are necessary for the elucidate mechanism of formation of different TiO_2 phases.

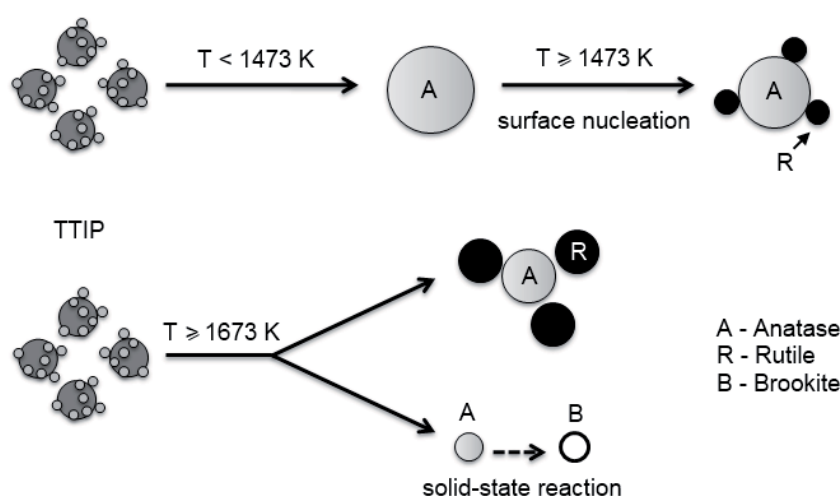


Fig. 4.20. Proposed mechanism for rutile and brookite phase formation for TiO_2 nanoparticles produced in gas phase (CVS)

4.1.2.2 The 'Up' Time-Temperature Profile

The XRD patterns of the as-synthesized TiO₂ nanoparticles using 'up' temperature profile are shown in Fig. 4.21. The patterns are not much different from those synthesized using 'flat' temperature profile (Fig. 4.11). The powders consist of anatase as a main phase, and the second phases (rutile and/or brookite) appear above

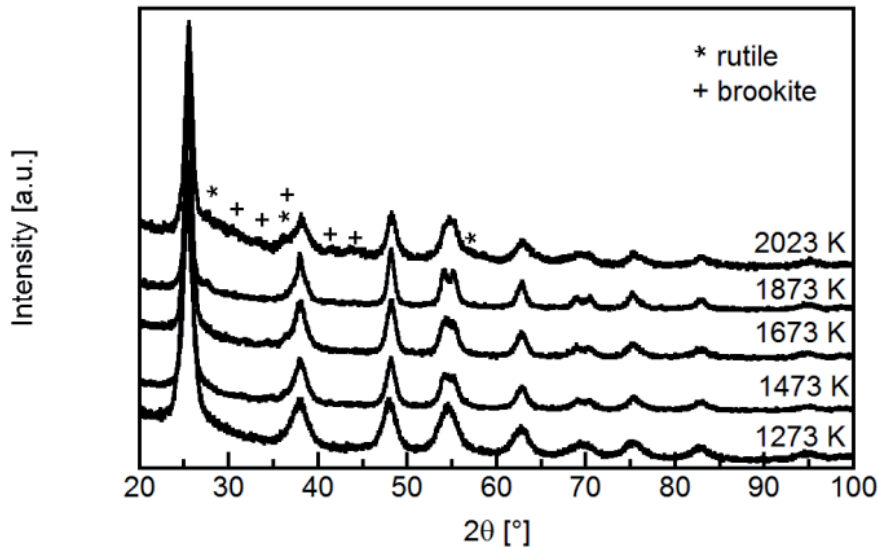


Fig. 4.21. The XRD patterns of the TiO₂ particles synthesized using the 'up' time-temperature profile

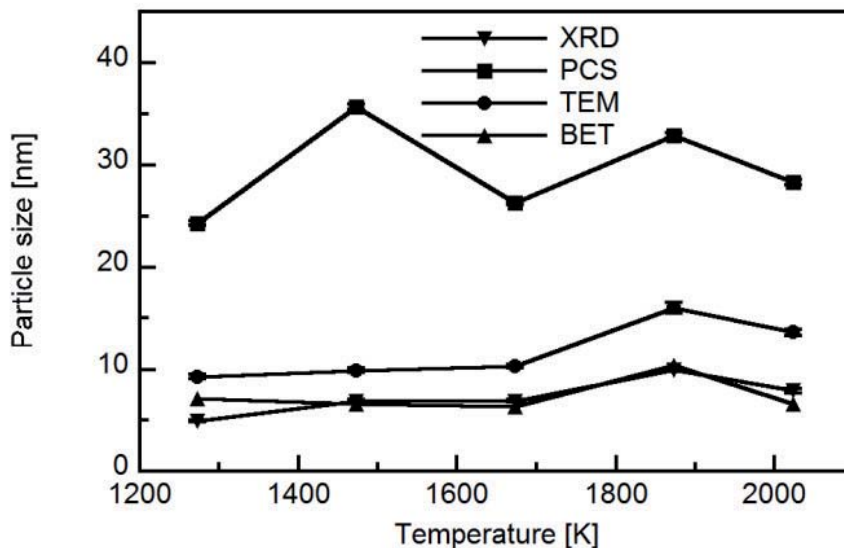


Fig. 4.22. Particle size determined using different characterization techniques as a function of process temperature for the 'up' time-temperature-profile

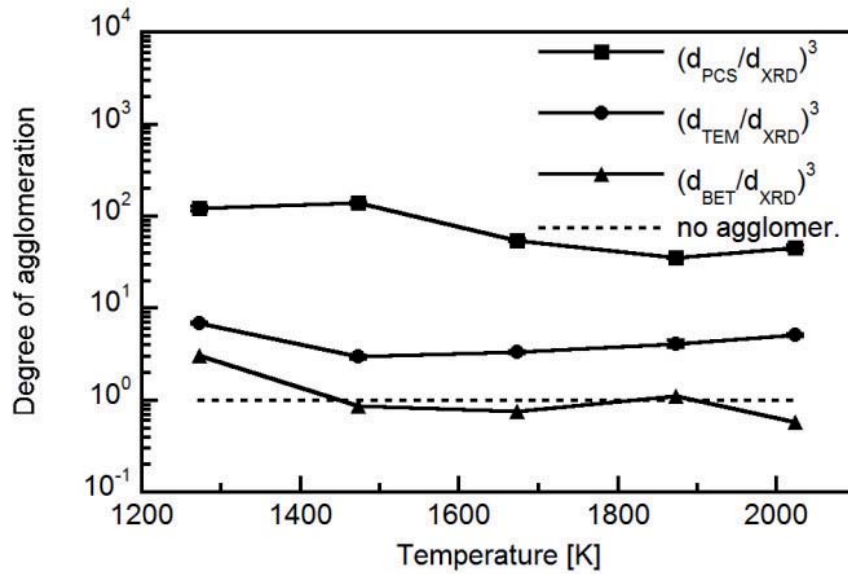


Fig. 4.23. Degree of agglomeration as a function of process temperature for the ‘up’ time-temperature profile

1273 K. The crystallite size, obtained from the Rietveld refinement of the XRD patterns, ranges from 5 to 10 nm (Fig. 4.22). Similarly to the ‘flat’ temperature profile, the crystallite size from the XRD is relatively close to the particle size obtained from TEM and BET, and lower than particle size obtained from PCS (Fig. 4.22). As it was expected, the degree of agglomeration is decreasing with increasing the process temperature (Fig. 4.23).

4.1.2.3 Comparison of Different Time-Temperature Profiles

The CVSSIN simulation predicted that the ‘up’ temperature profile is more efficient in reducing the degree of particle agglomeration than the ‘flat’ temperature profile (Fig. 4.10). Experimental results show that this prediction is valid only for the degree of agglomeration calculated for particles in a ‘dry’ form (according to e.g. BET and TEM, Fig. 4.24), but has deviation for particles in solution (according to PCS). The reason for the observed deviation may be that the method of dispersing particles for PCS size measurement (ultrasonic treatment) is not efficient enough, and may even be a source of additional particle agglomeration. Similar results are obtained for the degree of agglomeration at temperatures other than 1473 K, Figs. 4.25 and 4.26. Without any doubt, and independently on the time-temperature profile configuration, at the high process temperature particles with lowest degree of agglomeration are generated.

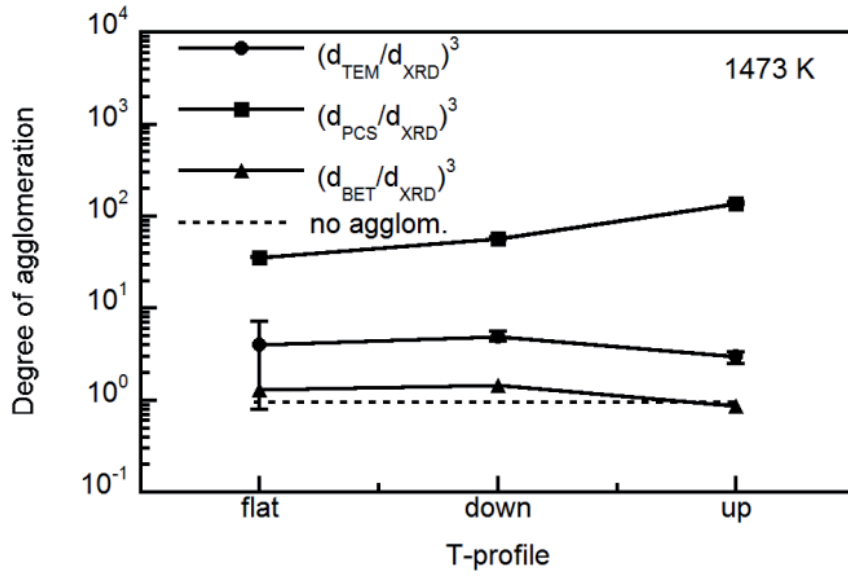


Fig. 4.24. Degree of agglomeration for the 'flat', 'down' and 'up' time-temperature profiles

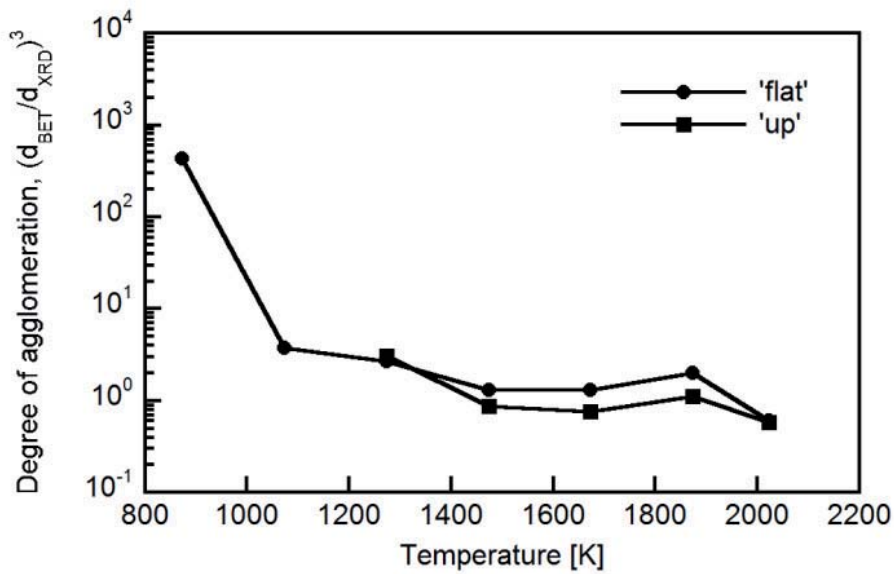


Fig. 4.25. Comparison of degree of agglomeration for the 'flat' and 'up' time-temperature profiles estimated from BET and XRD for different process temperatures

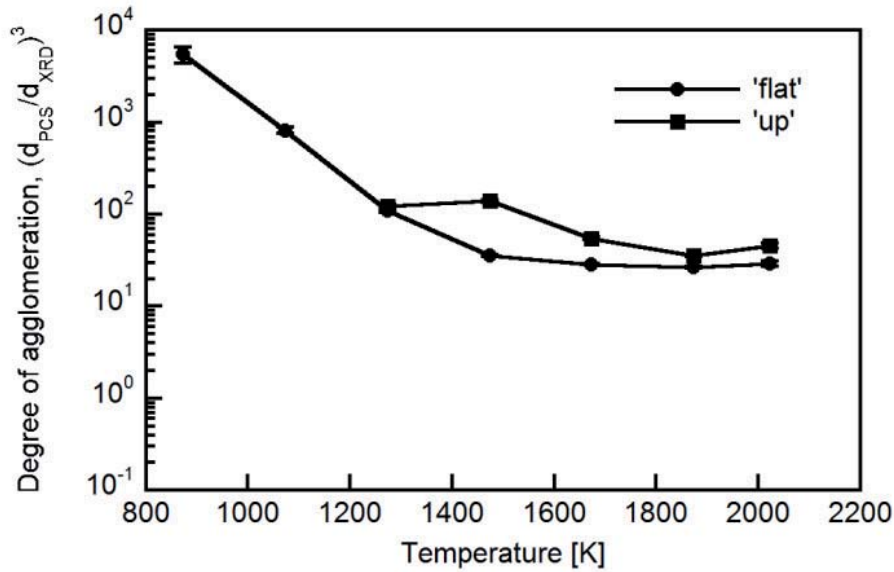


Fig. 4.26. Comparison of degree of agglomeration for the ‘flat’ and ‘up’ time-temperature profiles estimated from PCS and XRD data for different process temperatures

4.1.3 Comparison of the CVSSIN Model with Experimental Data

A comparison of the degree of agglomeration obtained from the CVSSIN model and calculated from the experimental data for a ‘flat’ temperature profile is shown in Figs. 4.27 and 4.28. It can be seen that the experimental data follows the trend of the CVSSIN model. A somewhat better agreement (in terms of the absolute values) was observed when the model is compared with experimental values obtained from BET and XRD (Fig. 4.27) than that one obtained from PCS and XRD (Fig. 4.28). The cause for the observed differences between the degree agglomeration obtained from the model and that one obtained from the experiment (PCS/XRD) may lay in the particle preparation for the PCS measurement. Namely, particles are dispersed in water using an ultrasonicator and there is a possibility that ultrasonication causes additional particle agglomeration due to intensified particle collisions.

In general, model matches better with experiment at higher temperatures, than at lower temperatures. It is known [Nakaso et al. 2003] that the surface reactions dominate particle growth at lower temperatures. As the surface reactions were not included in the CVSSIN model, this could be the reason for the observed discrepancy between model and experiment at lower temperatures. The other reason which can contribute to not good matching is the value of the activation enthalpy for the grain boundary diffusion (Eq. 2.14) used in the model (29909 K). In order to check the sensitivity of the model on activation enthalpy (E_D/k_B) two arbitrary values were chosen (25000 K and 35000 K) and compared to that one reported in the literature and used the model (29909 K). The result is shown in Fig. 4.29. As it can be seen, there is a significant influence on the absolute values, especially at lower temperatures where better matching is observed for the lower activation

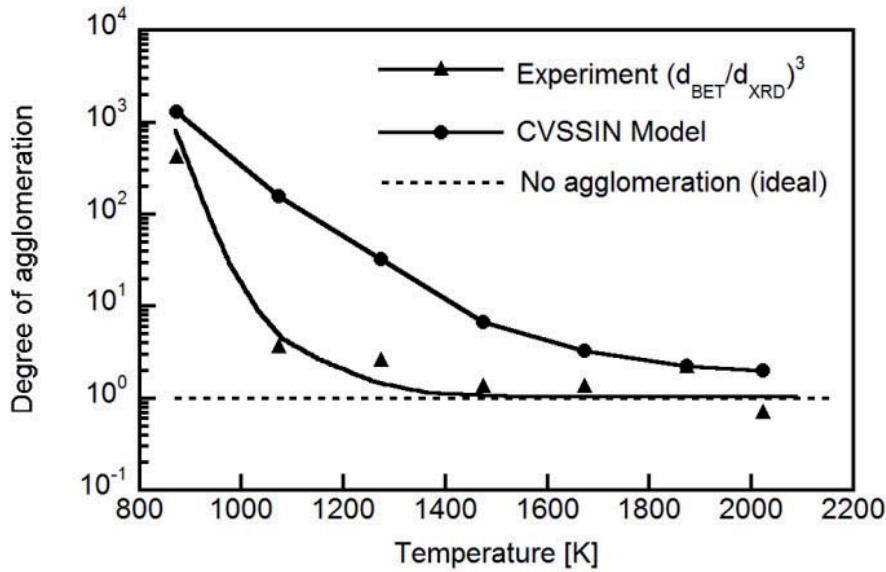


Fig. 4.27. Comparison of degree of agglomeration obtained from the model and experimental values obtained from the BET and XRD data for the ‘flat’ time-temperature profile

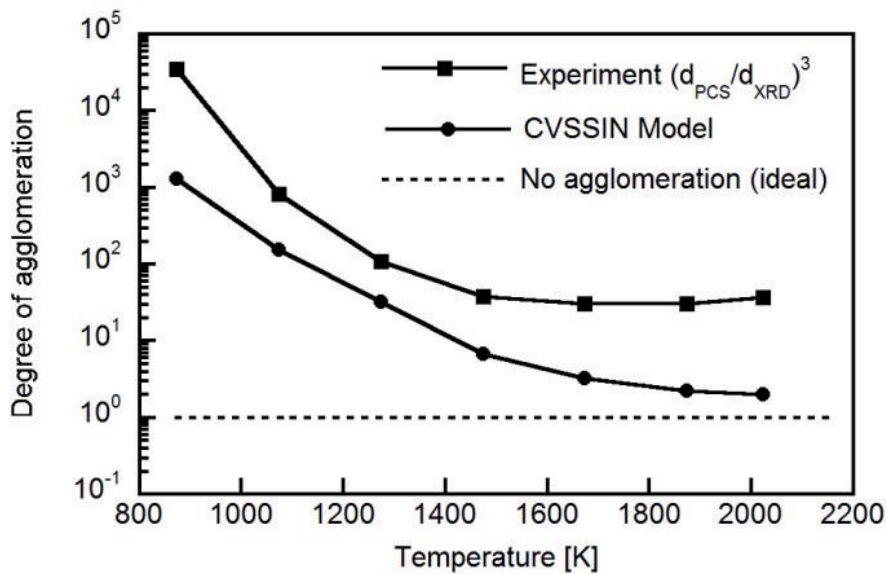


Fig. 4.28. Comparison of degree of agglomeration obtained from the model and experimental values obtained from the PCS and XRD data for the ‘flat’ time-temperature profile

enthalpy. This observation is most probably correlated with faster sintering kinetics of smaller particles which are formed at the lower temperatures (Fig. 4.14.)

In order to understand better the particle agglomeration, method of characteristic times [Friedlander 2000]) was used where the residence, collision and sintering times are calculated and their ‘interaction’ analyzed.

The residence time, τ_r , is estimated as the time interval between maximum heating and cooling rate as obtained from the CVSSIN model.

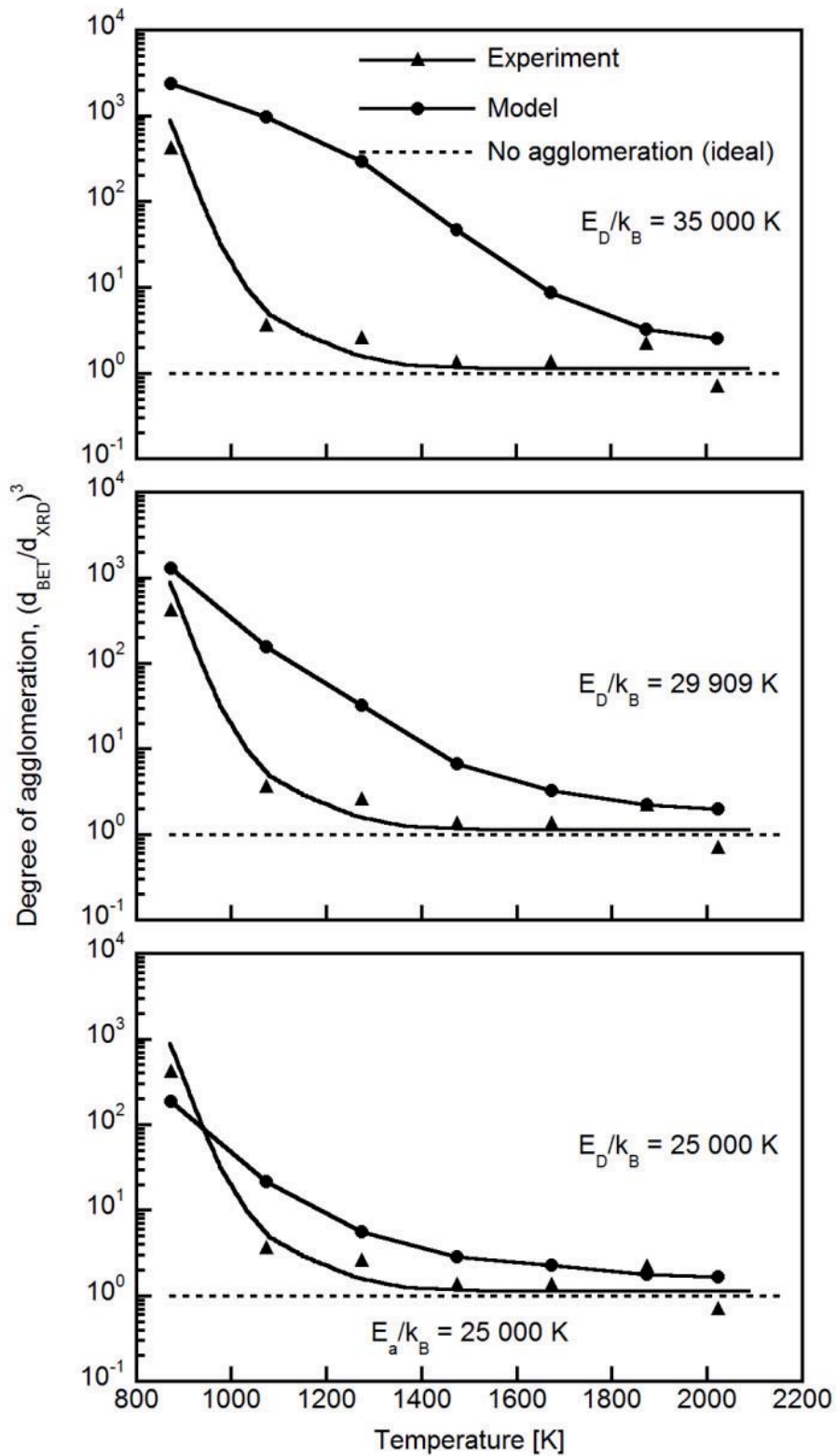


Fig. 4.29. Influence of the activation enthalpy of grain boundary diffusion on the results (degree of agglomeration) of the simulation and comparison with experimental results obtained from BET and XRD data

The collision time, τ_c , was calculated from Eq. 2.9, where for the number density of agglomerates, N_a , the value obtained from the CVSSIN simulation (at the reactor position where the cooling rate is highest) was used. For calculation of the collision frequency, β (Eq. 2.7), as a collision diameter, d_c , the particle diameter obtained from PCS was used. Finally, the collision time is calculated as:

$$\tau_c \cong 1.72 \cdot 10^{12} \left[\frac{s^2 K}{m^3} \right]^{1/2} \frac{1}{N_a \cdot (T \cdot d_c)^{1/2}} \quad (4.2)$$

The sintering time, τ_s , was calculated from Eq. 2.13, where for the primary particle size, d_p , the crystallite diameter obtained from XRD was used. The grain boundary diffusion coefficient, D_{gb} , was calculated from Eq. 2.14. Finally, the sintering time by grain boundary diffusion is calculated as:

$$\tau_s \cong 6.58 \cdot 10^{19} \left[\frac{s}{Km^4} \right] \cdot T \cdot d_p^4 \cdot \exp\left(\frac{29909}{T}\right) \quad (4.3)$$

The characteristic times (residence, collision and sintering), as a function of the highest process (wall) temperature, are presented in Fig. 4.30. As the collision time is shorter than the sintering time ($\tau_c < \tau_s$) for the entire set of process temperatures (873–2023 K), particles collide and form agglomerates. Similar theoretical results were reported for SiO₂ [Tsantilis and Pratsinis 2004] and TiO₂ [Grass et al. 2006] particles produced by flame synthesis as well as SiC [Winterer 2002] nanoparticles. At temperatures below 1700 K where the sintering time is longer than the collision time ($\tau_s > \tau_c$), particles collide much faster than they sinter which contributes to higher degree of agglomeration. Above this temperature, as the sintering time becomes shorter than the residence time, sintering of primary particles in-

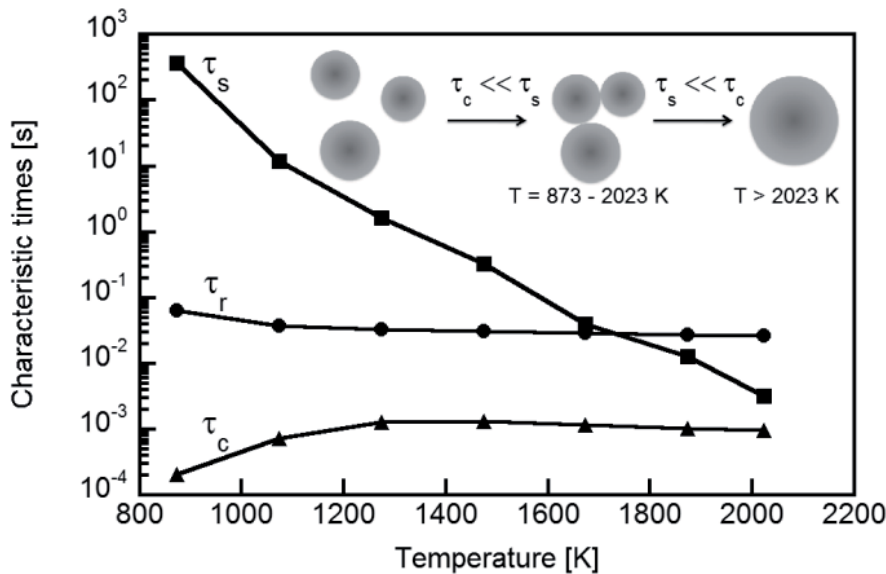


Fig. 4.30. Characteristic times as a function of process temperature (τ_s – sintering, τ_c – collision, τ_r – residence time)

side the agglomerate becomes feasible [Nakaso 2003] and the degree of agglomeration becomes significantly lower (e.g. Fig. 4.27). No agglomeration is expected at temperatures well above 2023 K when the sintering time becomes much shorter than collision time ($\tau_s \ll \tau_c$).

4.1.4 Conclusion

Characteristics of nanocrystalline materials (here TiO_2 as a study material) produced by chemical vapor synthesis are sensitive to the time-temperature history of the gas phase in the reactor. With increasing wall temperatures the gas temperature becomes sufficiently high and sufficient for a complete coalescence of the primary particles inside the agglomerates and the quenching rate at the reactor exit fast enough to prevent an extensive formation of hard agglomerates. Therefore, the fast quenching at the end of the reactor is essential for the formation of weakly agglomerated particles. Using chemical vapor synthesis, not only the particle size and degree of agglomeration is controllable, but also the degree of crystallinity as well as the microstrain. The use of an induction hot-wall reactor allows flexibility in designing the different temperature profiles which can allow the optimization of powder characteristics, hence having a control over material properties.

4.2 Particle Size and Size Distribution by Pulsed Precursor Delivery

Figure 4.31 shows diffraction patterns of selected as-synthesized TiO_2 powders. Powders synthesized by evaporating the precursor using a CO_2 laser operated at higher (25 kHz) and lower (1 kHz) frequency (Fig. 4.31a) are highly crystalline nanoparticles consisting of anatase with a very small contribution of rutile. The powders synthesized varying the laser duty cycle (Fig. 4.31b) showed high crystallinity as well.

It is interesting to mention that only powder synthesized by evaporating the precursor with the laser operated at high frequency 25 kHz ($DC = 50\%$) were

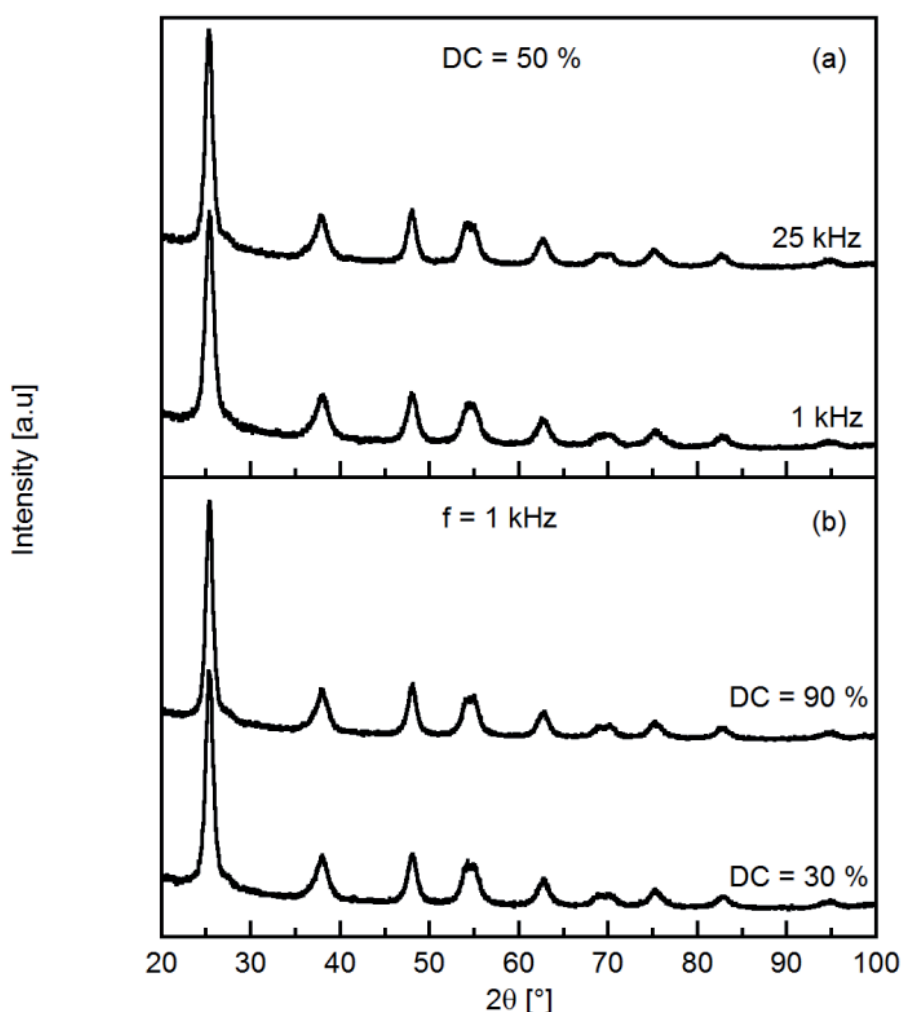


Fig. 4.31. The XRD patterns of selected TiO_2 particles synthesized from $\text{Ti}(\text{P})_2(\text{TMHD})_2$ precursor which was evaporated using a CO_2 laser operated by varying the frequency (a) and duty cycle (b)

grayish, while the all other powders were white, clearly indicating difference in the precursor concentration in the reactor. At high frequency (25 kHz) delivery of precursor can be considered as a continuous, hence due to the high precursor concentration, the process conditions were not optimal for the complete precursor decomposition.

4.2.1 Influence of Laser Pulse Repetition Frequency

For lower laser pulse repetition frequencies it is expected that the particle number concentration in the reactor is lower and thus the formation of smaller particles with a narrow particle size distribution (PSD) was expected. Figure 4.32 shows the TEM images of TiO₂ particles synthesized using a high (25 kHz) and a low (0.05 kHz) laser frequency. From the images it can be already seen that particle size does not differ much. Detailed analysis of particle size from the TEM images for the frequency range 0.05–25 kHz showed that the particle size is not affected by change of the laser pulse repetition frequency (Fig. 4.33). The slight fluctuation in particle size observed at lower frequency is most likely related to a variation of the amount of precursor available for the evaporation due to the manual feed of the precursor powder. Although it was expected that with lowering the laser pulse repetition frequency, the particle size distribution will become narrower, only an insignificant narrowing of the particle size distribution from σ_g of 1.25(3) to 1.23(2) was observed (Fig. 4.34). Friedlander [Friedlander 2000] has shown that the particle size distribution can reach so-called “self-preserving” size distribution. The “self-preserved” size distribution is characterized by the geometric standard deviation of 1.40 and 1.46 for the continuum and free molecule regime, respecti-

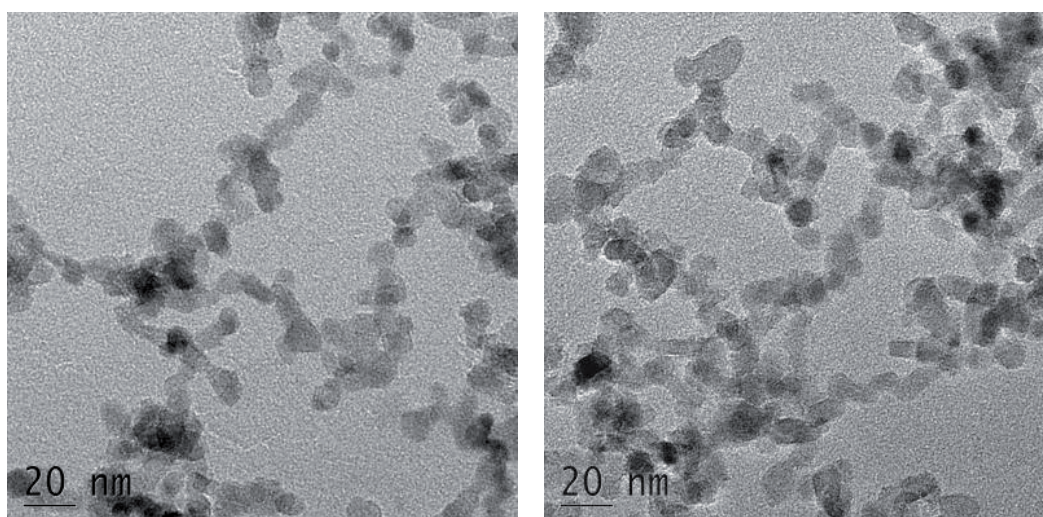


Fig. 4.32. TEM images of TiO₂ nanoparticles synthesized using a laser operated at 25 kHz (left) and 0.05 kHz (right) with 50 % of duty cycle

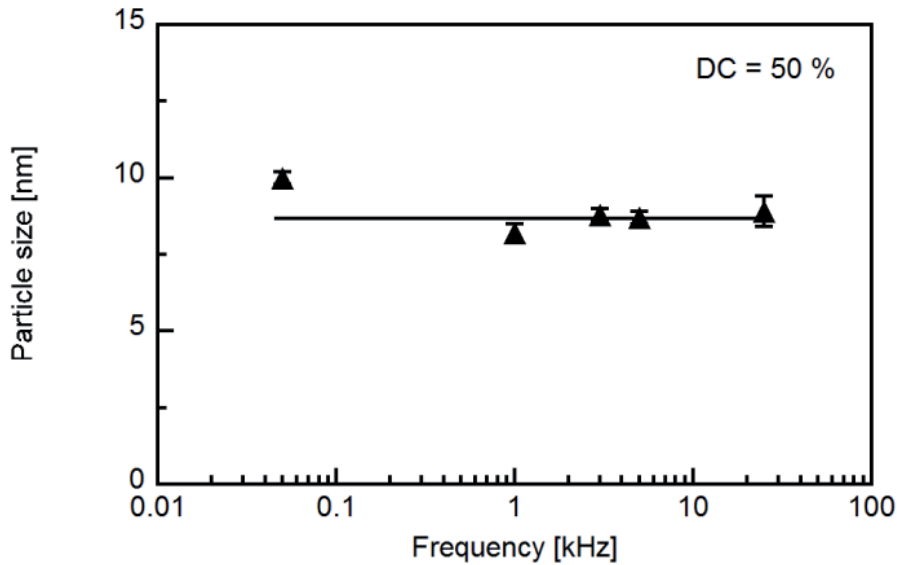


Fig. 4.33. Particle size as a function of the laser pulse repetition frequency at 50 % of duty cycle

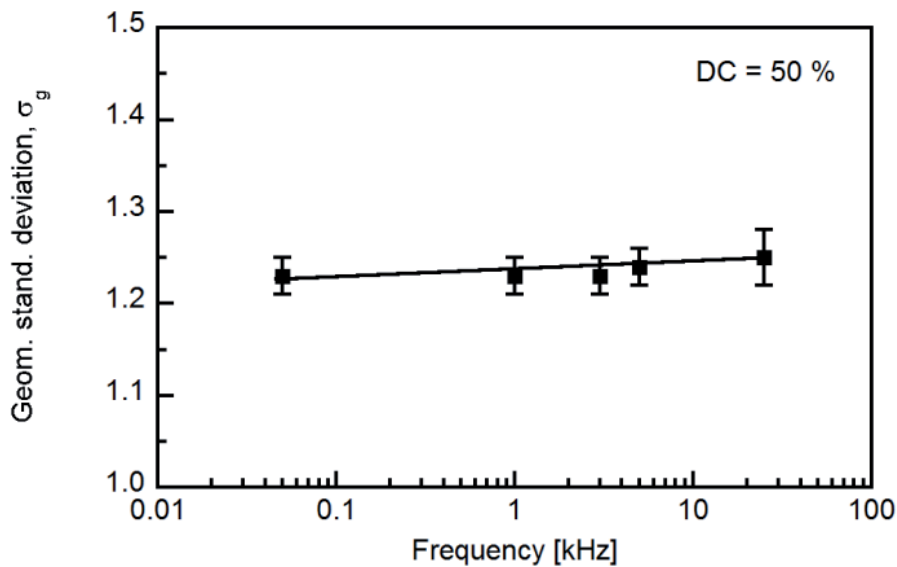


Fig. 4.34. Geometric standard deviation as a function of laser pulse repetition frequency at 50 % of duty cycle

vely. As the width of TiO_2 particle size distribution presented here is about 1.25, the “self-preserved” size distribution has not been reached and it is already rather narrow. Therefore, variations in other process parameters probably mask changes in the size distribution originating from the pulsed operation of the flash evaporator.

Kodas and Friedlander [Kodas and Friedlander 1988] investigated the monodispersed aerosol production in tubular low reactors and they found that in order to produce monodispersed aerosols, the nucleation and growth step should be separated, the residence time distribution should be narrow (all particles have same time to grow) and particles should be exposed to similar monomer concentration.

Therefore, as it was mentioned above, the manual precursor feeding, which causes the fluctuations in the evaporated amount of the precursor, could be the reason for not significant change in the width of the particle size distribution.

4.2.2. Influence of Laser Duty Cycle

Figure 4.35 shows the TEM images of TiO₂ particles synthesized using a frequency of 1 kHz and varying the duty cycles. It is clear that duty cycle has a significant influence on the particle size, as it is also observed in Fig. 4.36. Therefore, choosing a lower duty cycle, the amount of precursor, and consequently the number concentration of particles was evidently reduced, leading to the formation of smaller particles. Not only the particles size decreased but also the degree of agglomeration showed a significant decrease, as it can be seen from the cubed ratio of particle size obtained from the PCS and XRD (Fig. 4.37). Concerning the width

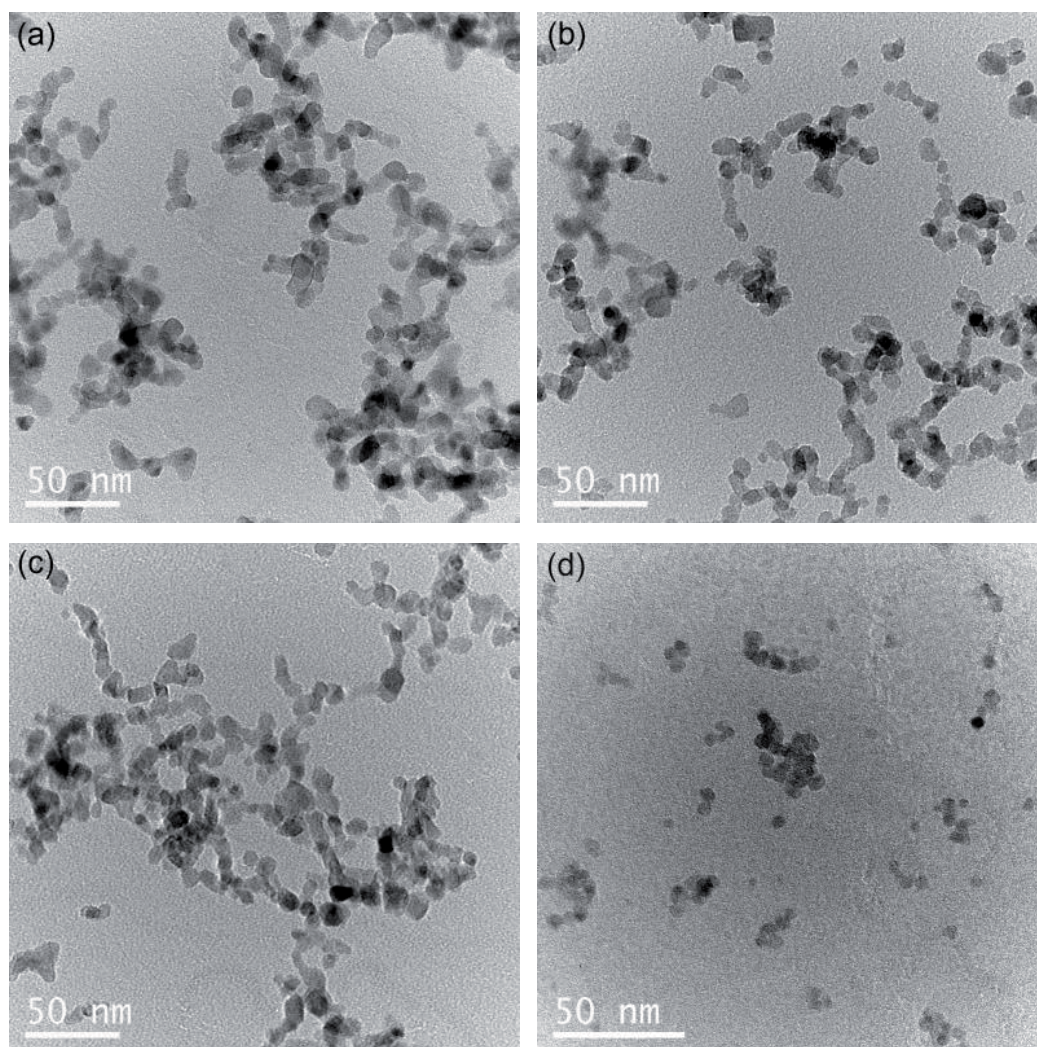


Fig. 4.35. TEM images of TiO₂ nanoparticles synthesized using the laser operating at 1 kHz and different duty cycles: 100 % (a), 80 % (b), 60 % (c) and 20 % (d)

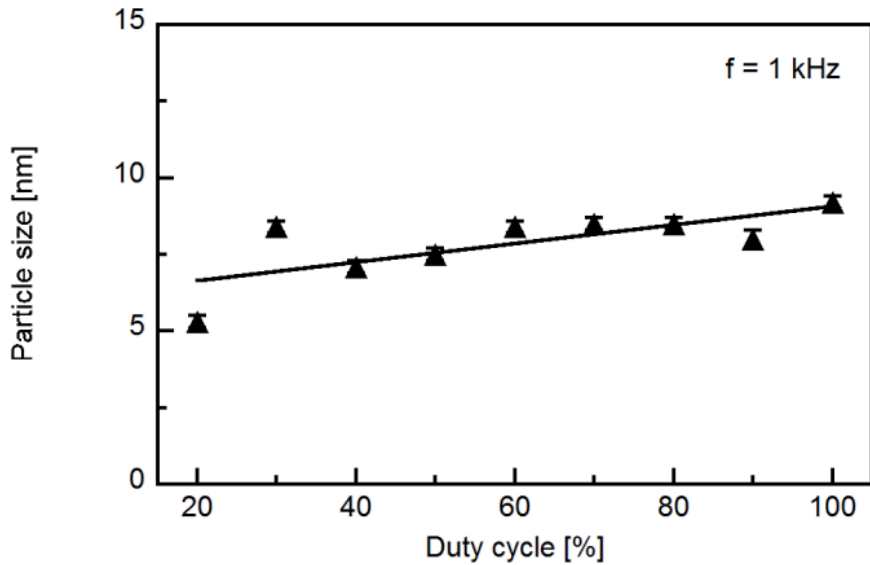


Fig. 4.36. Particle size obtained from the TEM images as a function of laser duty cycle at 1000 Hz

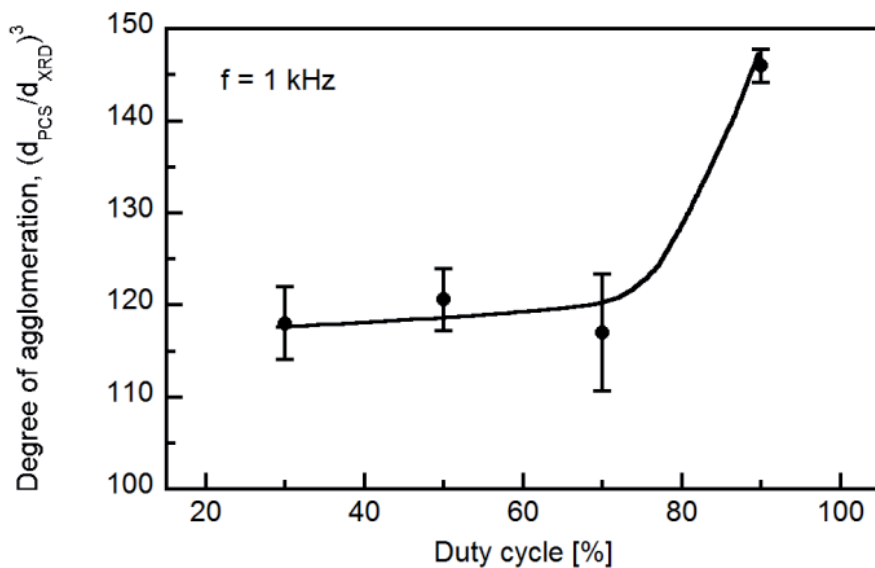


Fig. 3.37. Particle degree of agglomeration as a function of duty cycle at frequency of 1 kHz (line is only guide to the eyes)

of particle distribution, results showed that at 1 kHz, the duty cycle has no influence on the particle size distribution (Fig. 4.38). Similar conclusions can be drawn for the experiments performed at lower frequency (0.2 kHz), shown in Figs. 4.39–4.41. Duty cycle had only impact on particle size (Figs. 4.39 and 4.40), while no influence on the width of the particle size distribution was observed (Fig. 4.41).

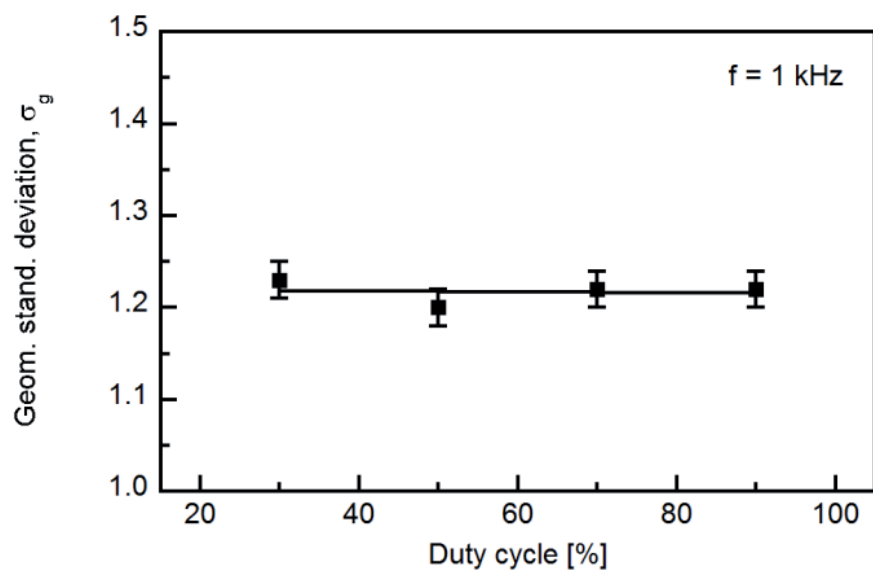


Fig. 4.38. Geometric standard deviation as a function of laser duty cycle at 1 kHz

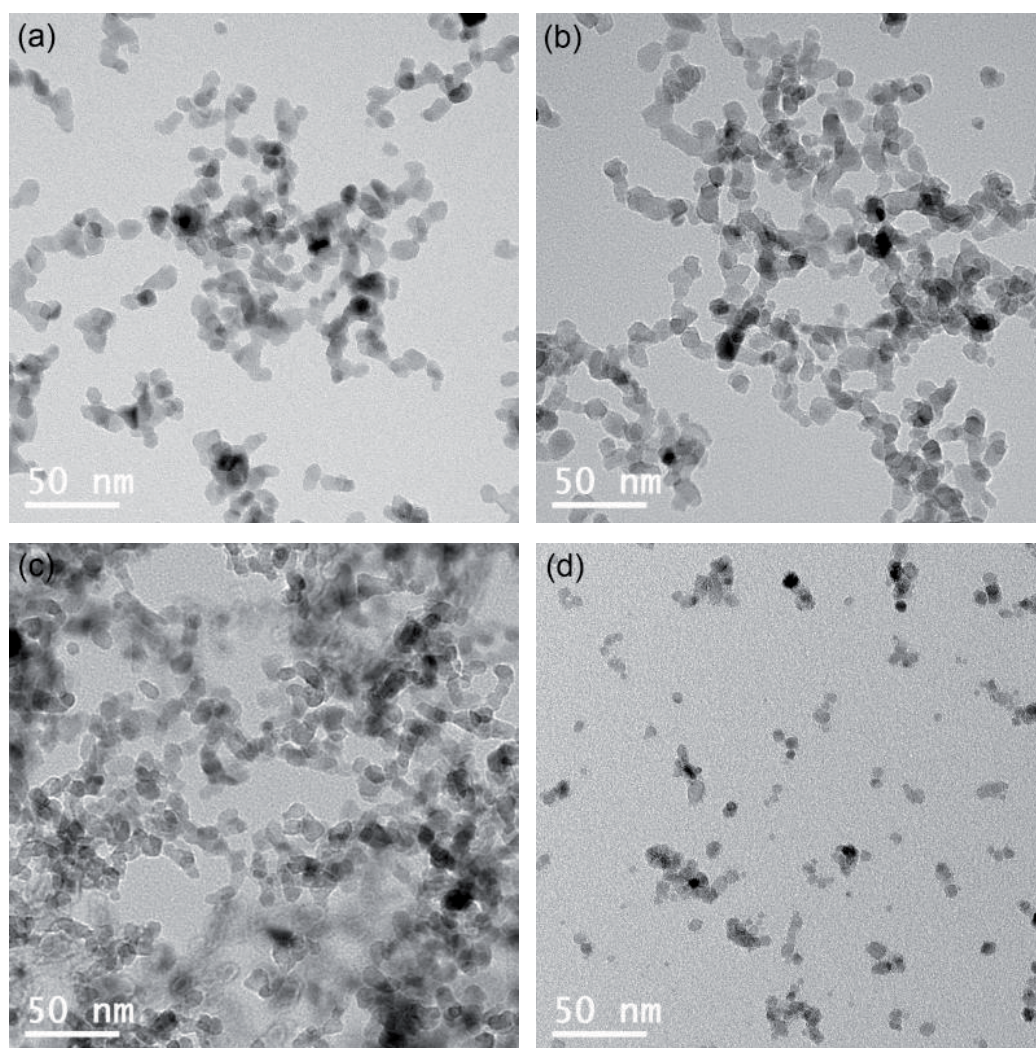


Fig. 4.39. TEM images of TiO_2 nanoparticles synthesized using the laser operating at 0.2 kHz and different duty cycles: 100 % (a), 80 % (b), 60 % (c) and 20 % (d)

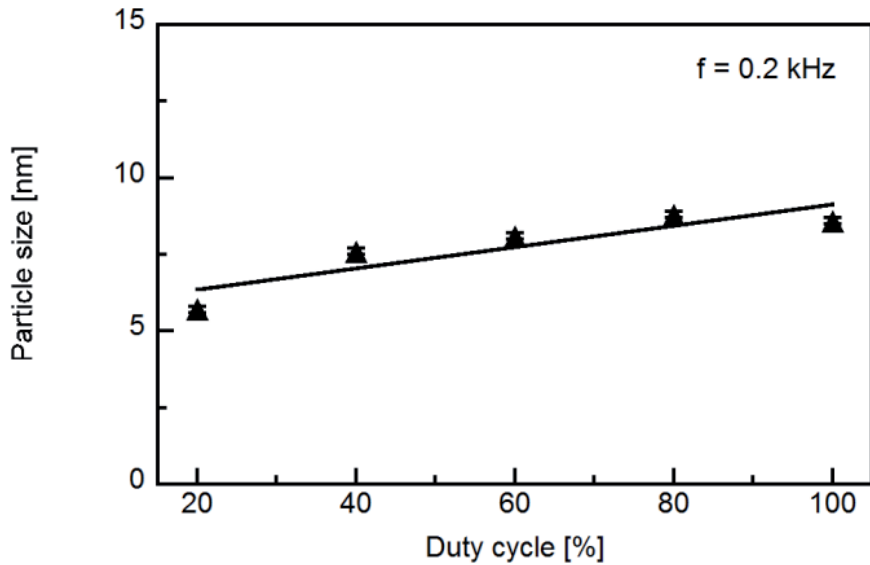


Fig. 4.40. Particle size as a function of laser duty cycle at 0.2 kHz

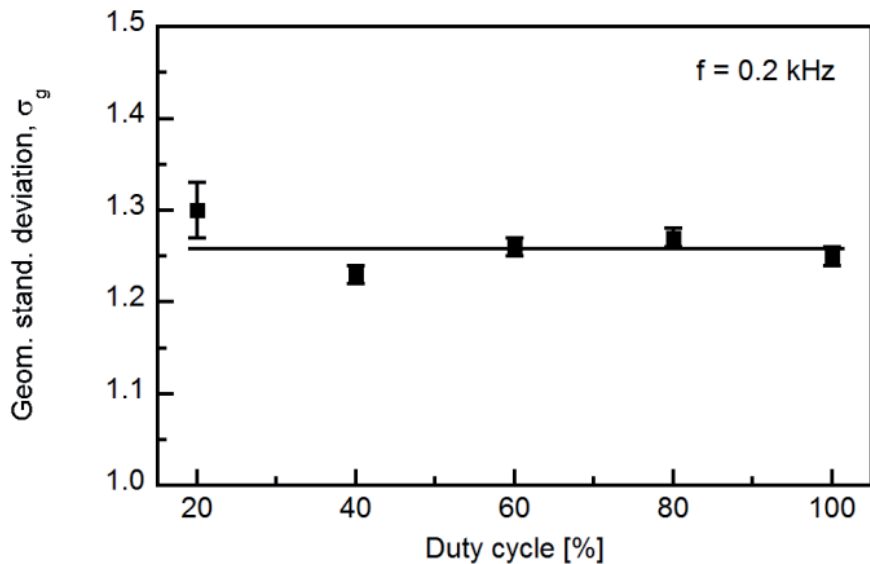


Fig. 4.41. Geometric standard deviation (obtained from the log-normal fit of the TEM data) as a function of laser duty cycle at 0.2 kHz

4.2.3 Conclusion

A systematic study of the influence of pulsed precursor delivery in a CVS reactor showed so far only limited influence on the width of the particle size distribution, but a significant impact on the reduction of the particle size and the degree of agglomeration. The laser pulse repetition frequency had only little influence on the particle size and the size distribution. On the other hand, it is possible to lower the particle number concentration, thus to have influence on reducing the final particle size with rather narrow particle size distribution by decreasing the laser duty cycle. A lower duty cycle leads also to a significant decrease in the degree of agglomeration.

4.3 Structure and Properties of Doped ZnO Nanoparticles

As the chemical composition, crystal and local structure play an important role in particle properties, detailed structural characterization is essential for their understanding. Therefore, in the following section the structure and magnetic properties of the Co-doped ZnO, $\text{Zn}_{1-x}\text{Co}_x\text{O}$ ($x = 0-0.50$) and Co, Li-codoped ZnO, $\text{Zn}_{0.95-y}\text{Co}_{0.05}\text{Li}_y\text{O}$ ($y = 0-0.05$) nanoparticles will be discussed.

4.3.1 Chemical Composition

The chemical analysis of the $\text{Zn}_{1-x}\text{Co}_x\text{O}$ ($x = 0-0.50$) by AAS (Fig. 4.42) shows that the actual Co concentrations (x_a) in the as-synthesized $\text{Zn}_{1-x}\text{Co}_x\text{O}$ nanoparticles are systematically higher compared to the nominal concentration (x) of the precursor mixture used. It is also observed that the evaporation rate of the precursor mixture as determined from its weight loss is enhanced with increasing Co concentration (Fig. 4.43) which may explain the systematic deviation of the actual Co content from the nominal. The reason for increasing evaporation rate of precursor mixture with increasing Co content is probably that the Co-acetate precursor absorbs more laser light compared to the Zn-acetate at the wavenumber corresponding to the narrow CO_2 laser emission as it can be seen from the FTIR spectra (Fig. 4.44). The advantage of using a laser flash evaporation method for

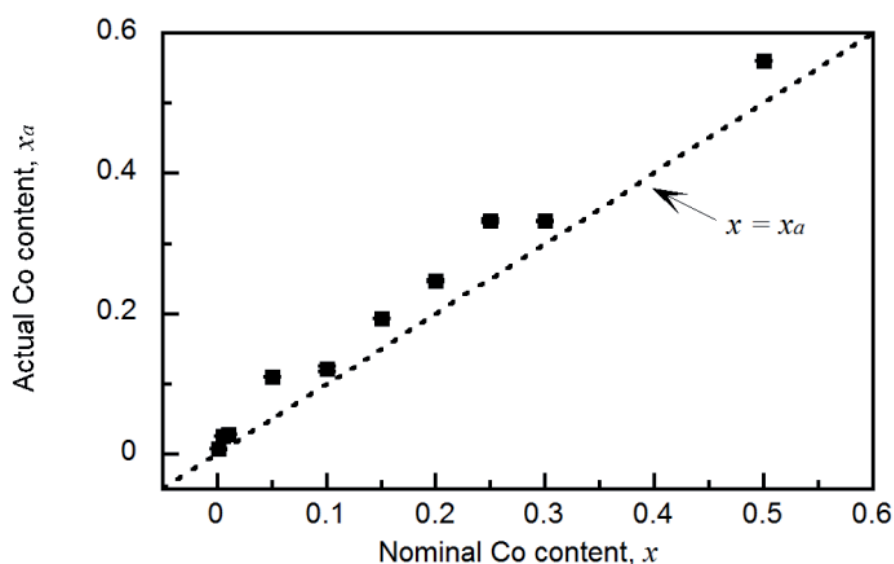


Fig. 4.42. Correlation between actual (x_a) and nominal (x) Co content (error bars are smaller than the symbols)

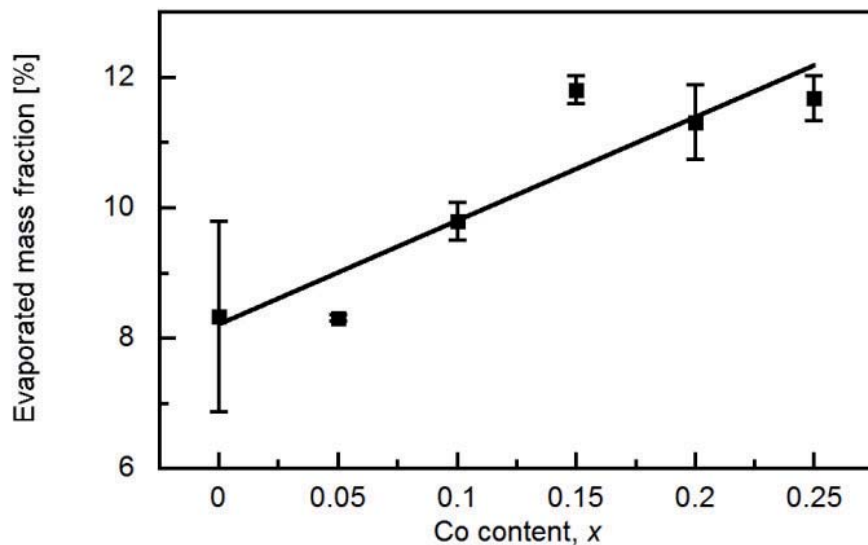


Fig. 4.43. Evaporation rate of precursor mixture as a function of nominal Co content

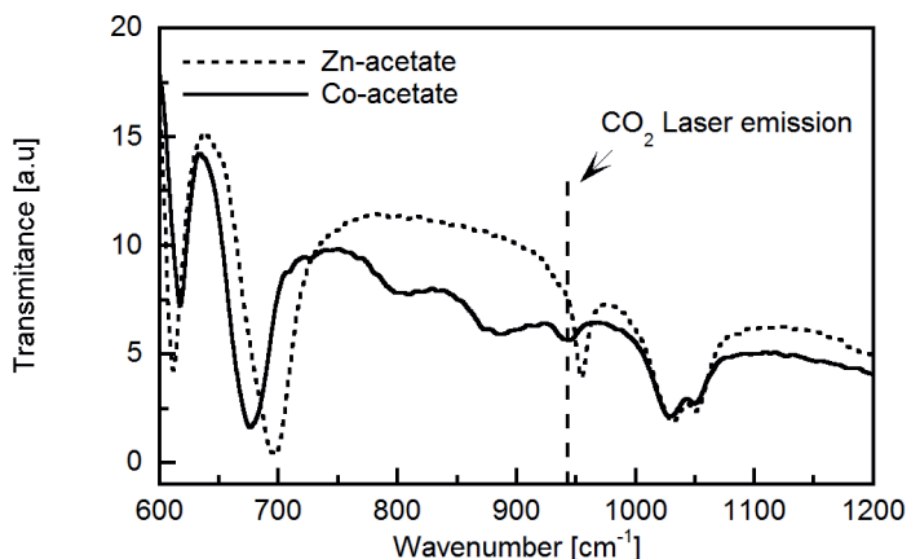


Fig. 4.44. The FTIR spectra of the Zn- and Co-acetate precursor and the emission line of the CO₂ laser (wavelength of 10.6 μm)

precursor evaporation is that chemical composition can be easily adjusted knowing the evaporation rates of used precursors which can be easily obtained from the mass balance.

The TEM study of the sample with the highest Co content (Zn_{0.75}Co_{0.25}O, actual Co content of $x_a = 0.33$), Fig. 4.45 confirms that Co atoms are distributed homogeneously in the sample. The same is valid for particles with lower Co content. This result is very important regarding the magnetic properties of this material as it will be discussed later.

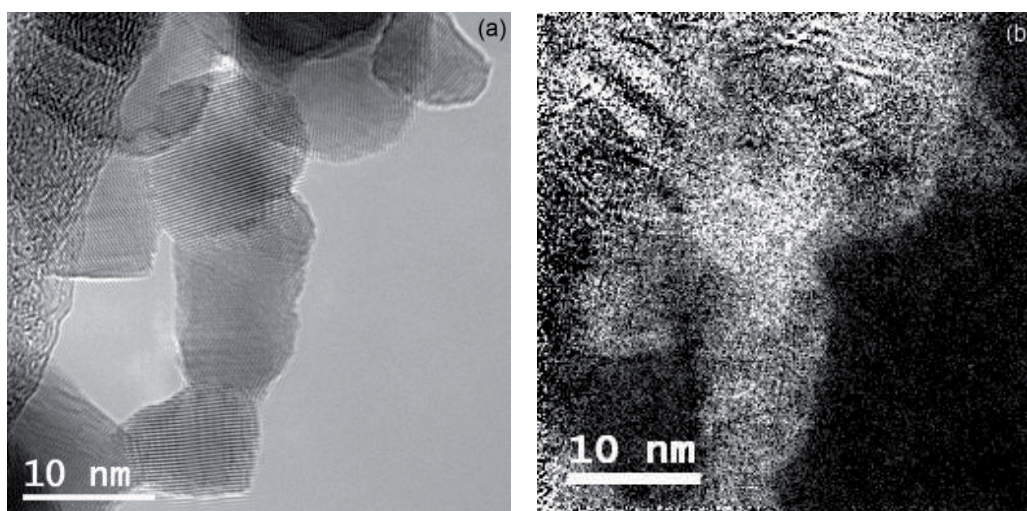


Fig. 4.45. TEM micrographs of $\text{Zn}_{0.85}\text{Co}_{0.15}\text{O}$ sample (a) and Co elemental map (b) showing the uniform distribution of Co atoms in the sample (bright spots)

4.3.2 Crystal Structure

Figure 4.46 shows the XRD patterns of as-synthesized $\text{Zn}_{1-x}\text{Co}_x\text{O}$ nanoparticles. The substitution of Co did not cause remarkable changes in the diffraction patterns for Co contents up to $x \leq 0.25$. Rietveld refinement of XRD data shows (Fig. 4.47) that those particles are of wurtzite structure, while in particles with Co concentration $x \geq 0.30$ CoO and Co_3O_4 are present as additional phases. The maximum Co solubility in wurtzite type ZnO, for which the particles are still single-phase, varies greatly for samples of the same nominal composition but prepared by different methods [Kolesnik et al. 2004, Risbud et al. 2003, Duan et al. 2008, Jayaram et al. 1999, Schaedler et al. 2006]. Recently, Straumal et al. [Straumal et al. 2008, 2009B] found that the solubility of Co and Mn increases with decreasing the grain size. They showed that the solubility of Co increases with decreasing grain size from 2 at. % in the bulk and up to about 40 at. % in polycrystalline samples (grain sizes below 20 nm). The Co solubility limit in nanoparticles studied in this work, is about $x_a = 0.33$ (nominal content $x = 0.25$) (Figs. 4.42 and 4.46). Further Co addition causes the generation of second phases: CoO in the sample with nominal Co content of $x = 0.30$ ($x_a = 0.332$) and CoO and Co_3O_4 in the sample with $x = 0.50$ ($x_a = 0.56$). This is consistent with the literature reports [Straumal et al. 2008]. Additional doping with Li in $\text{Zn}_{0.95}\text{Co}_{0.05}\text{O}$ ($\text{Zn}_{0.95-y}\text{Co}_{0.05}\text{Li}_y\text{O}$), does not change the phase composition of as-synthesized $\text{Zn}_{0.95-y}\text{Co}_{0.05}\text{Li}_y\text{O}$ nanoparticles (Fig. 4.48). The crystallite size of $\text{Zn}_{1-x}\text{Co}_x\text{O}$ nanoparticles ranges from about 9 nm for undoped sample ($x = 0$) up to 20 nm for the sample with a Co content of $x = 0.25$ (Fig. 4.49). The incorporation of Co ions into the wurtzite structure leads not only to an increasing crystallite size (Fig. 4.49) but also to a decrease of the microstrain (Fig. 4.50a). The observation of an increase of crystallite size with increasing dopant content is opposite to other doping elements such as Cr [Jin et al. 2007] or Al [Brehm et al. 2006] where impurity drag is slowing down particle gro-

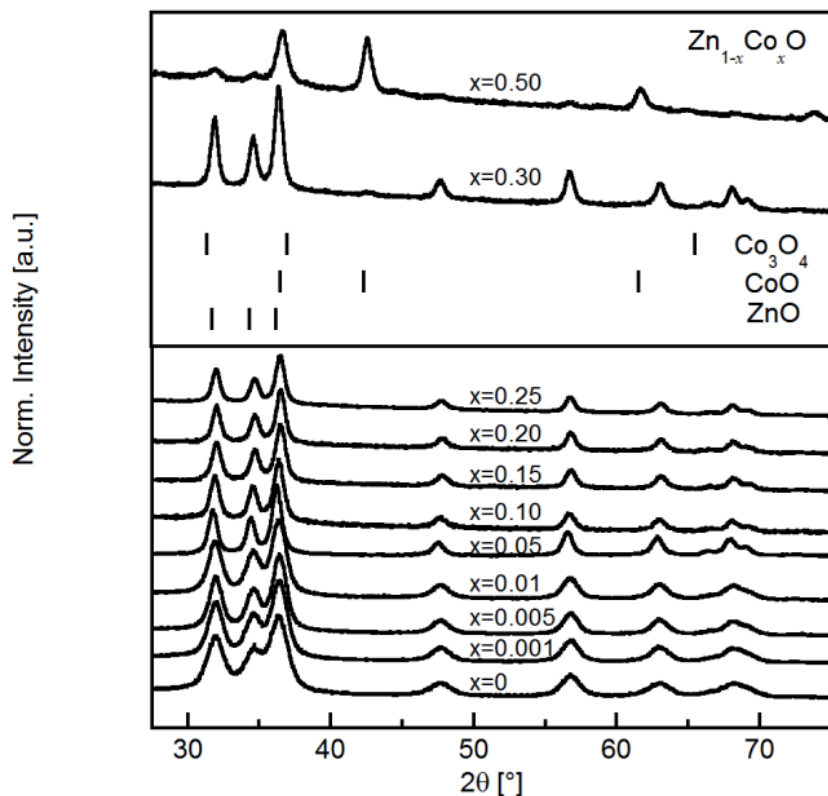


Fig. 4.46. XRD patterns of as-synthesized Zn_{1-x}Co_xO nanoparticles (vertical bars correspond to the three most pronounced Bragg reflections for wurtzite ZnO, CoO, and Co₃O₄)

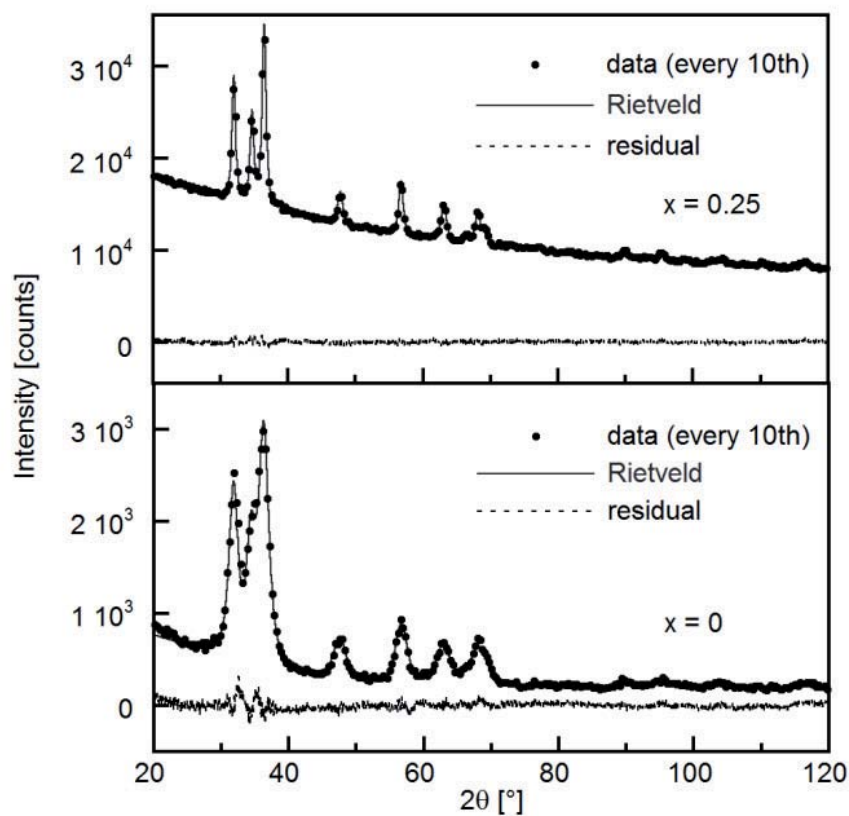


Fig. 4.47. Rietveld refinement of the XRD patterns of Zn_{1-x}Co_xO nanoparticles with nominal Co content $x = 0$ and $x = 0.25$

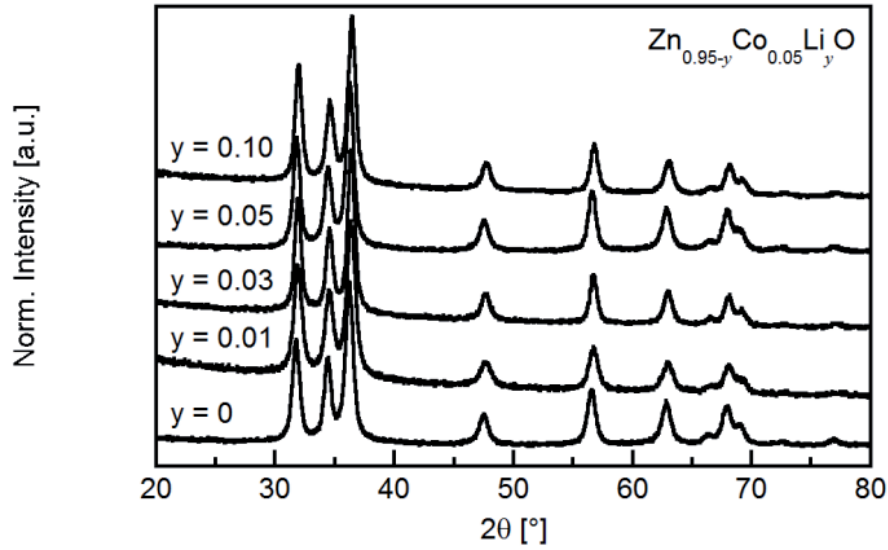


Fig. 4.48. XRD patterns of as-synthesized $\text{Zn}_{0.95-y}\text{Co}_{0.05}\text{Li}_y\text{O}$ nanoparticles

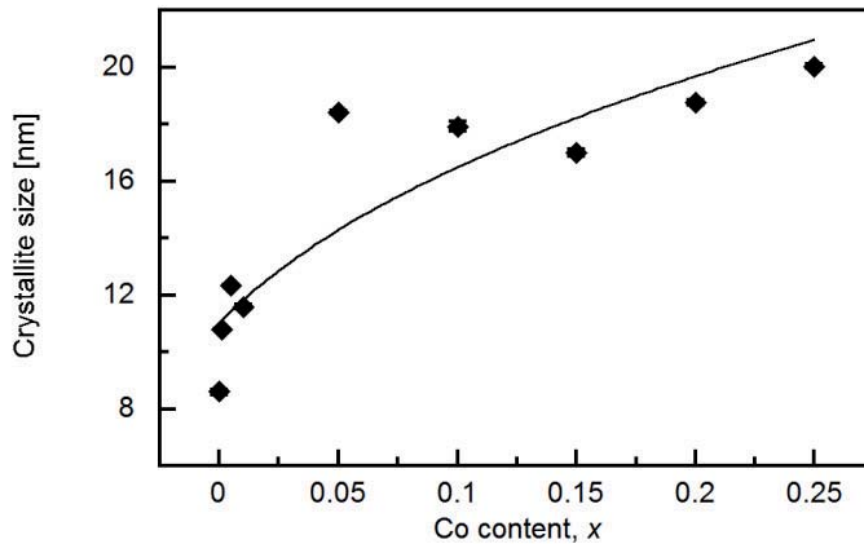


Fig. 4.49. Crystallite size of $\text{Zn}_{1-x}\text{Co}_x\text{O}$ nanoparticles as a function of Co content and fit according to monodisperse coagulation (Eq. 4.9) (error bars are smaller than the symbols)

with by coalescence. The origin for this observation is likely due to the increased evaporation rate with increasing Co content in the precursor mixture (Fig. 4.43). A fit with the growth law for monodisperse particles by coagulation [Hinds 2001] where d_0 is the initial particle diameter, N_0 the initial number concentration (which is assumed to increase linearly with the Co concentration) and β is the coagulation coefficient:

$$d = d_0 \cdot (1 + N_0 \cdot \beta \cdot t)^{1/3} \quad (4.9)$$

agrees with the experimental data (Fig. 4.49). Therefore, the cause for the decrease in microstrain is not because of the introduction of Co into the wurtzite lattice as Fig. 4.50a might suggest, but it is due to the decrease of surface to volume ratio

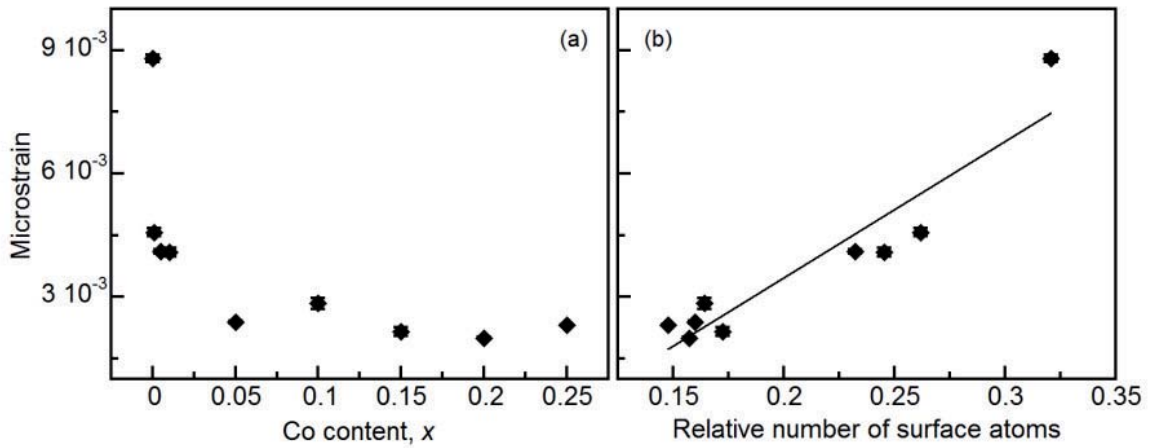


Fig. 4.50. Microstrain in $\text{Zn}_{1-x}\text{Co}_x\text{O}$ nanoparticles as a function of Co content (a) and the relative number of atoms on the particle surface (b)

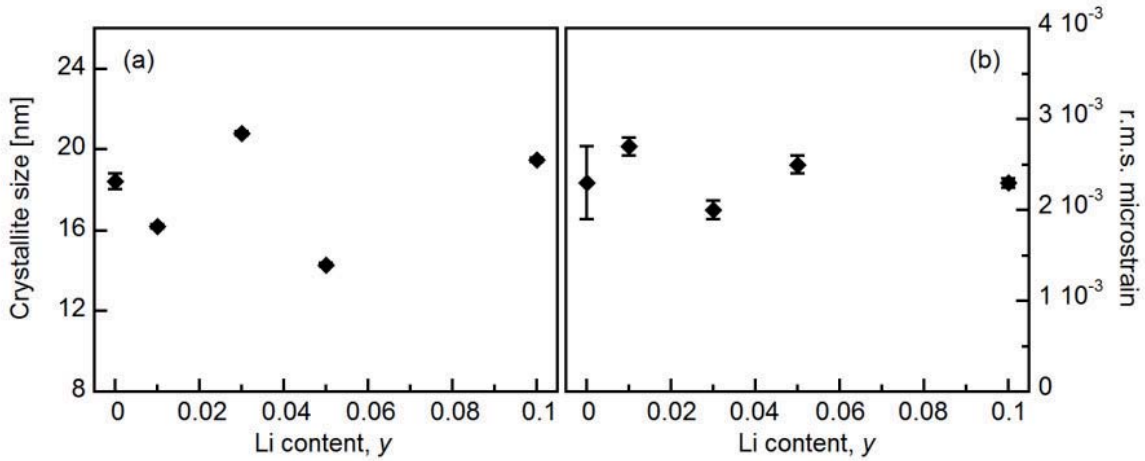


Fig. 4.51. Crystallite size (a) and microstrain (b) of $\text{Zn}_{0.95-y}\text{Co}_{0.05}\text{Li}_y\text{O}$ nanoparticles

with increasing crystallite size as it correlates linearly (Fig. 4.50b) with the relative number of atoms at the particle surface to the particle volume which is estimated by

$$\frac{N_{\text{surface}}}{N_{\text{volume}}} \approx 1 - \left(1 - \frac{c}{r}\right)^3 \quad (4.10)$$

where the lattice constant c is used to estimate the relaxation length (‘surface thickness’) and r is the radius of a sphere equivalent in volume to the average particle. Since the valence of Co and Zn in Co-doped ZnO is identical and the ionic radii for both are similar [Shannon 1976], the microstrain is varying little above Co contents $x = 0.05$. For samples with Li ($\text{Zn}_{0.95-y}\text{Co}_{0.05}\text{Li}_y\text{O}$) slight fluctuations in crystallite size are observed, and consequently in microstrain (Fig. 4.51).

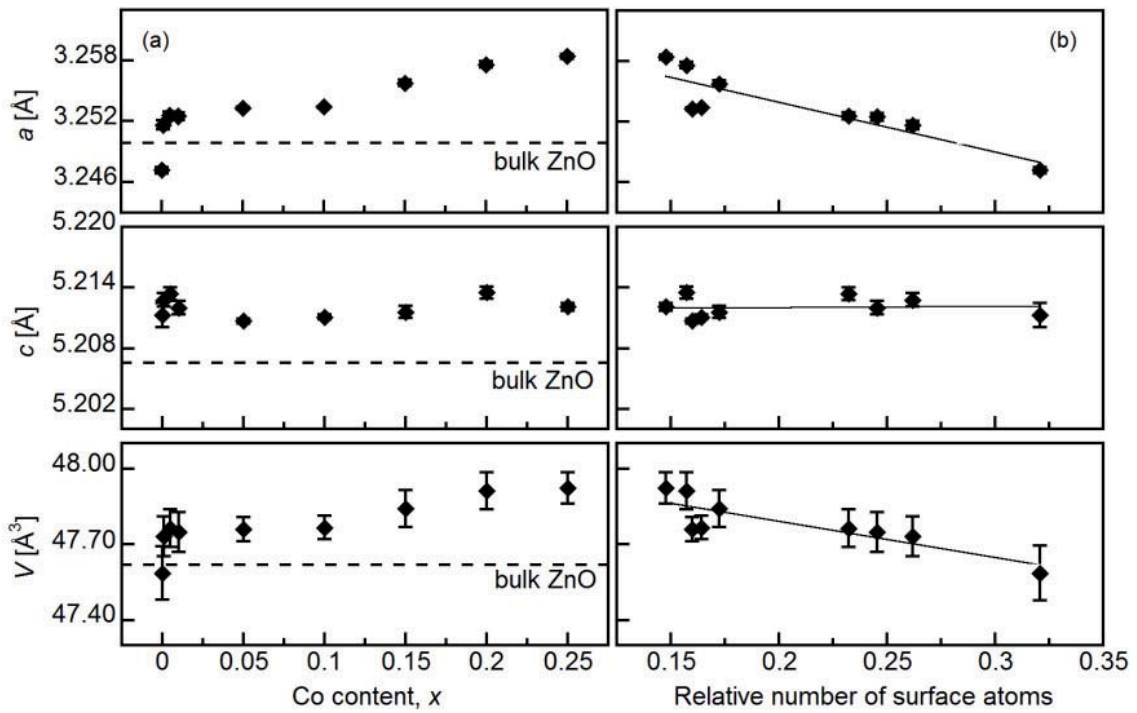


Fig. 4.52. Lattice parameters and unit cell volume of $\text{Zn}_{1-x}\text{Co}_x\text{O}$ nanoparticles as a function of Co content (a) and relative number of surface atoms (b)

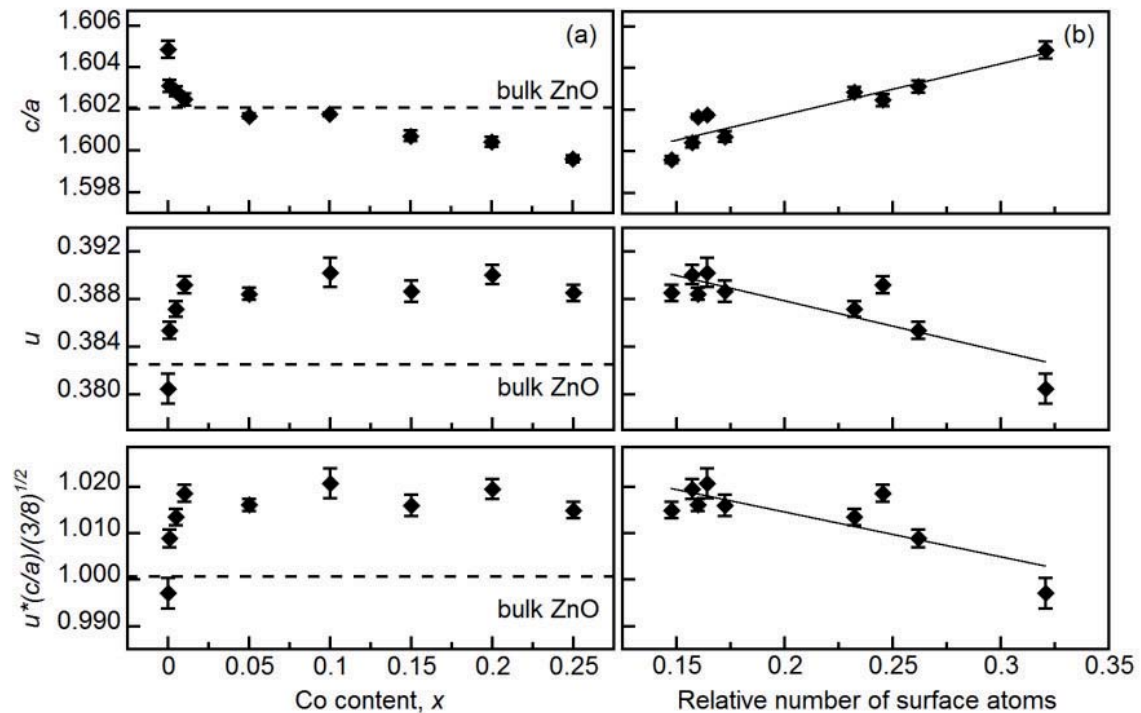


Fig. 4.53. Structural parameters of $\text{Zn}_{1-x}\text{Co}_x\text{O}$ nanoparticles determined from Rietveld refinement as a function of Co content (a) and as a function of relative number of surface atoms (b)

The lattice parameters of $\text{Zn}_{1-x}\text{Co}_x\text{O}$ nanoparticles obtained from Rietveld refinements are presented in Fig. 4.52a. It is found that Co substitution causes an elongation along the a -axis, while no significant change for the c -axis is observed. As a result the unit-cell volume increases and the c/a ratio decreases (Fig. 4.53a). A similar behavior is reported by Kolesnik et al. [Kolesnik et al. 2004]. Considering that the ionic radius of tetrahedrally coordinated Co^{2+} (0.58 Å) is only slightly smaller than Zn^{2+} (0.60 Å) [Shannon 1976], no changes in c - or a -direction are expected. Jin et al. [Jin et al. 2001] report similar observations concerning the c -axis in Co-doped films. The elongation along the a -axis up to $x = 0.005$ is therefore possibly a result of the lattice relaxation [Woltersdorf et al. 1981, Combe et al. 2009] due to a crystallite size effect which is correlated to the Co content (Fig. 4.49). This leads to a reduction of the relative number of surface atoms and consequently to lattice relaxation. Therefore, a linear correlation with the relative number of surface atoms is observed (Fig. 4.52b). Since the surface energies of ZnO are anisotropic (1.7 J/m² (0001), 0.9 J/m² ($\bar{1}\bar{1}00$)) [Kim et al. 2008] it can be expected that this effect varies with the crystallographic orientation. This may be the origin of the different trend for lattice constants a and c . For the Co content of $x = 0.25$ (Fig. 4.53a) the c/a ratio is decreasing below 1.6. The oxygen positional parameter in c -direction, u , describes the relative position of the anion to the cation sublattice in wurtzite [Kim et al. 2008] and $u(c/a)$ for an ideal wurtzite lattice would be 3/8 [Desgreniers 1998] which is observed for pure CVS ZnO nanocrystals and is close to the bulk value (Fig. 4.53a).

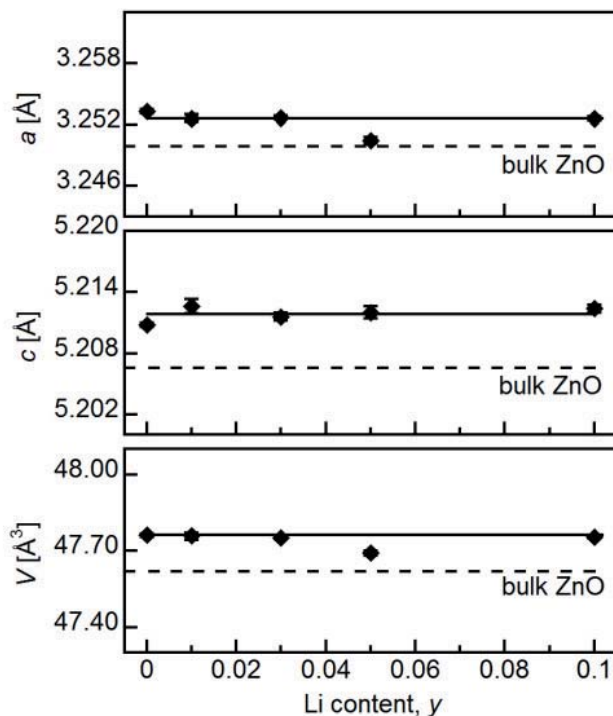


Fig. 4.54. Lattice parameters and unit cell volume of $\text{Zn}_{0.95-y}\text{Co}_{0.05}\text{Li}_y\text{O}$ nanoparticles as a function of Li content

Table 4.2. Change in lattice parameters and Zn–O bond length upon Li doping

Li content <i>y</i>	Change in lattice parameters [%]		Zn–O bond length [Å]
	<i>a</i>	<i>c</i>	
0	0	0	1.966(2)
0.01	0.02(1)	0.03(1)	1.964(4)
0.03	0.02(1)	0.02(1)	1.966(4)
0.05	0.09(1)	0.02(1)	1.968(3)
0.10	0.02(1)	0.038(1)	1.970(3)

The incorporation of Li into a wurtzite lattice of $\text{Zn}_{0.95}\text{Co}_{0.05}\text{O}$ nanoparticles, does not cause significant changes of the lattice parameters as well as in unit cell volume (Fig. 4.54, Table 4.2), which is expected considering similar atomic radii of Zn and Li in tetrahedral environment (0.60 and 0.59 Å, respectively). A theoretical study performed by Assadi et al. [Assadi et al. 2010] found that the length of Li–O (2.004 Å) almost perfectly matches with Zn–O (1.996 Å) bond length indicating that Li can be easily substitutionally incorporated into ZnO without large lattice distortion. The Zn–O bond length, l (as a function of Li content) has been calculated using the formula [Srinivasan et al. 2007]:

$$l = \left[\frac{a^3}{3} + \left(\frac{1}{2} - u \right)^2 \cdot c^2 \right]^{1/2} \quad (4.11)$$

where a and c are the lattice parameters, and u is the oxygen positional parameter in c -direction (all obtained from Rietveld refinement of XRD data). The calculated values are shown in Table 4.2. It can be seen that Zn–O bond lengths do not change upon Li doping indicating that Li is incorporated substitutionally into the wurtzite lattice.

4.3.3 Local Structure

A UV-Vis spectroscopy study of $\text{Zn}_{1-x}\text{Co}_x\text{O}$ nanoparticles (Fig. 4.55) revealed that Co is in a tetrahedral environment for all studied Co concentrations. The appearance of three absorption bands (triplets) at about 565 nm, 610 nm and 656 nm is a clear signature for Co^{2+} in tetrahedral coordination [Gaudon et al. 2007]. The addition of Li into $\text{Zn}_{0.95}\text{Co}_{0.05}\text{O}$ broadens peak at around 500 nm (Fig. 4.56) indicating a formation of defect sites (oxygen vacancies) upon Li doping [Adamopoulos et al. 2010].

In order to exclude possibility of existence of the other Co species (metallic Co, or its oxides) and further confirm the substitution of Zn with Co, element specific X-ray absorption spectroscopy (XAFS) was used for the detailed analysis of $\text{Zn}_{1-x}\text{Co}_x\text{O}$ nanoparticles. XAFS provides information about the distribution and location of Co in the wurtzite lattice complementary to X-ray diffraction which is not sensitive to segregation or the formation of very small precipitates of second

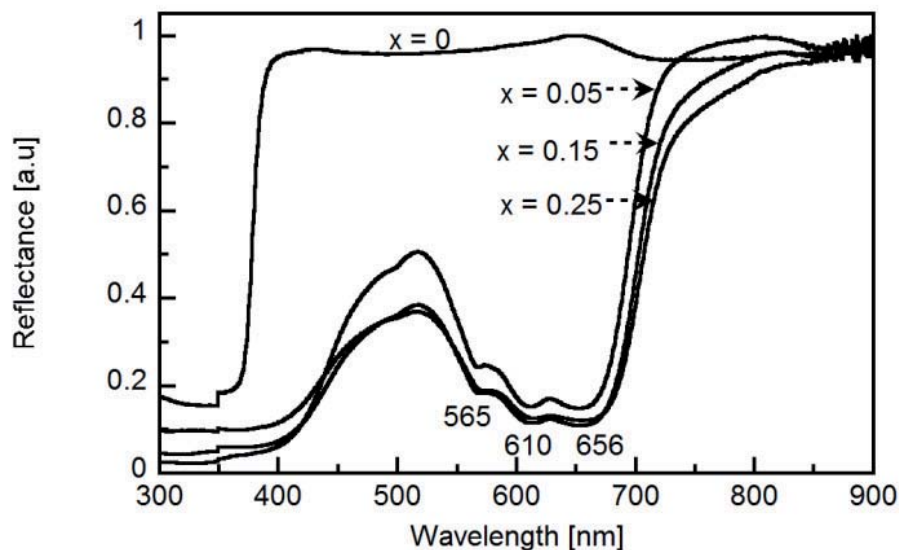


Fig. 4.55. UV-Vis spectra of $\text{Zn}_{1-x}\text{Co}_x\text{O}$ nanoparticles

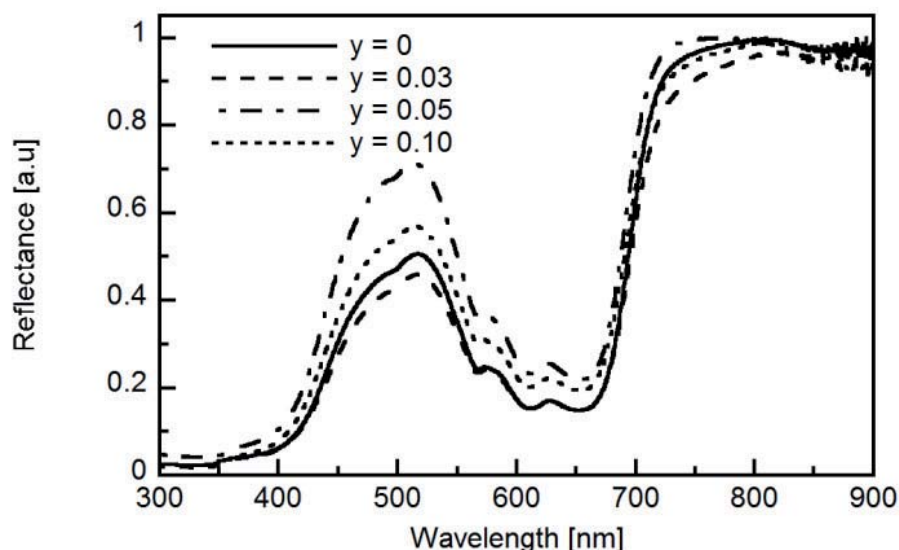


Fig. 4.56. UV-Vis spectra of $\text{Zn}_{0.95-y}\text{Co}_{0.05}\text{Li}_y\text{O}$ nanoparticles

phases especially at low dopant concentration. Figure 4.57 shows normalized Co and Zn K -edge XANES spectra of the $\text{Zn}_{1-x}\text{Co}_x\text{O}$ together with reference spectra of Co metal, CoO, and Co_3O_4 . Comparing the XANES spectra of $\text{Zn}_{1-x}\text{Co}_x\text{O}$ with the spectra of the CoO reference, reveals that the Co is present in the Co^{2+} valence state. The existence of Co metal and Co-oxides can be excluded using fingerprint methods due to the different spectral features of $\text{Zn}_{1-x}\text{Co}_x\text{O}$ as compared with that of Co-oxides. The small pre-edge peak at about 7708 eV (Fig. 4.57a) appears due to the transition of Co $1s$ electron to $4p$ - $3d$ hybridized states in tetrahedral symmetry [Sun et al. 2008]. The shoulder above the absorption edge in the Zn K -edge XANES spectra at 9680 eV (Fig. 4.57b) is related to scattering contributions from higher coordination shells [Liu et al. 2008].

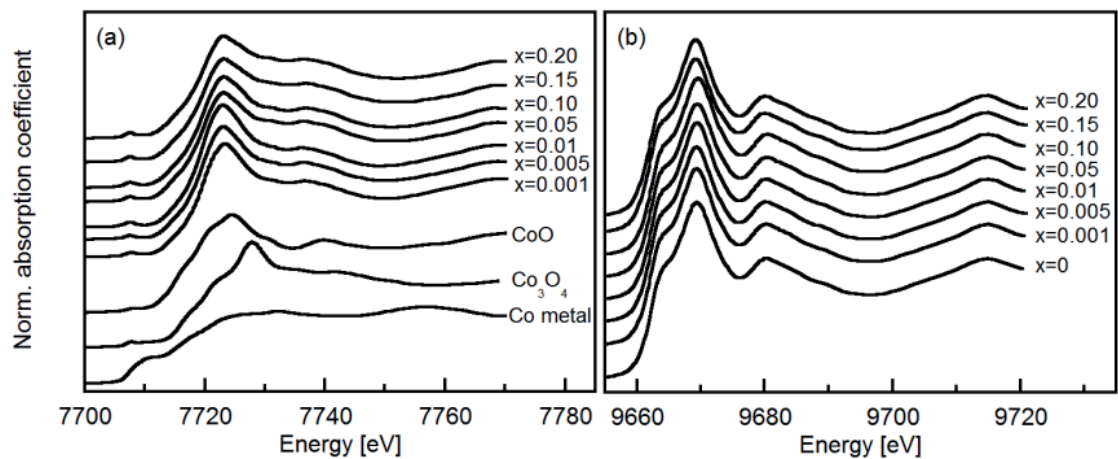


Fig. 4.57. Co *K*-edge XANES spectra of Zn_{1-x}Co_xO, CoO, Co₃O₄, Co metal (a) and Zn *K*-edge XANES spectra for Zn_{1-x}Co_xO (b)

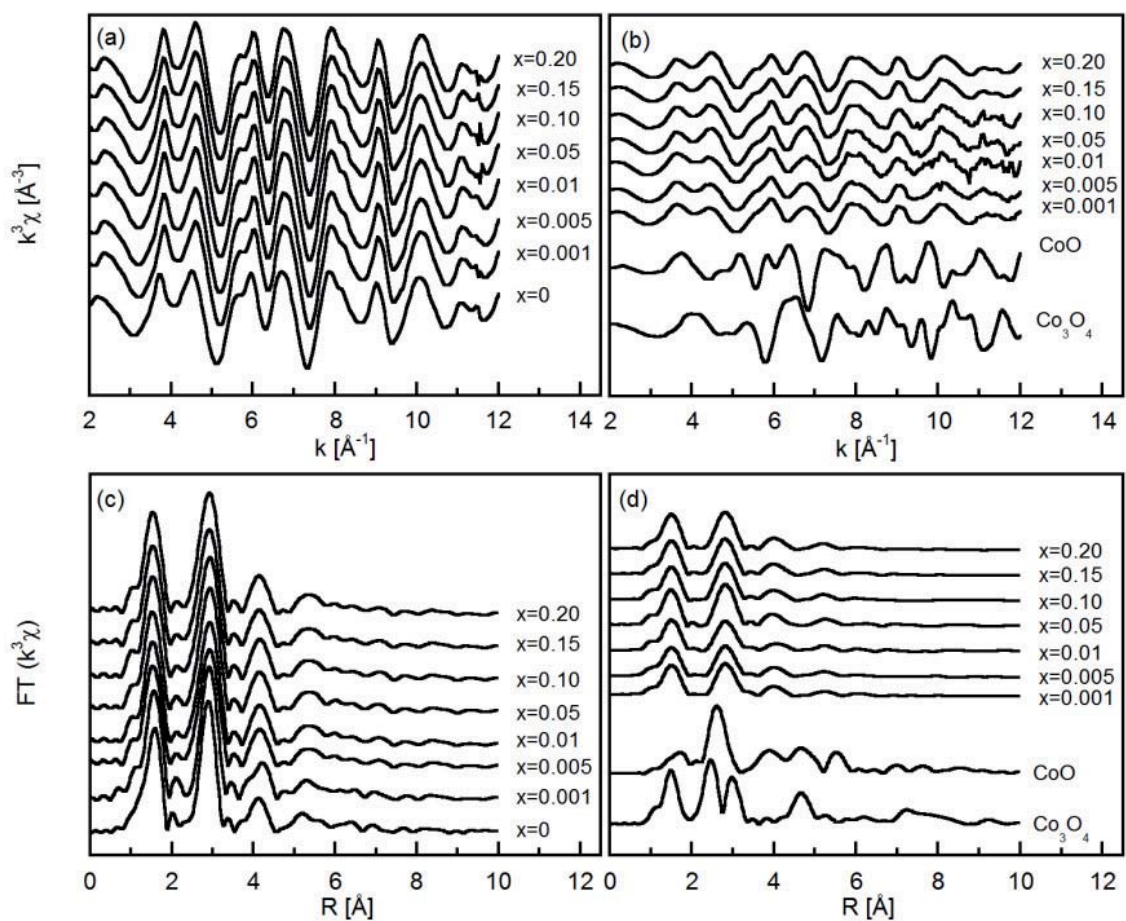


Fig. 4.58. The EXAFS spectra for Zn_{1-x}Co_xO on Zn *K*-edge (a) and Co *K*-edge (b) and corresponding radial structure function on Zn *K*-edge (c) and Co *K*-edge (d)

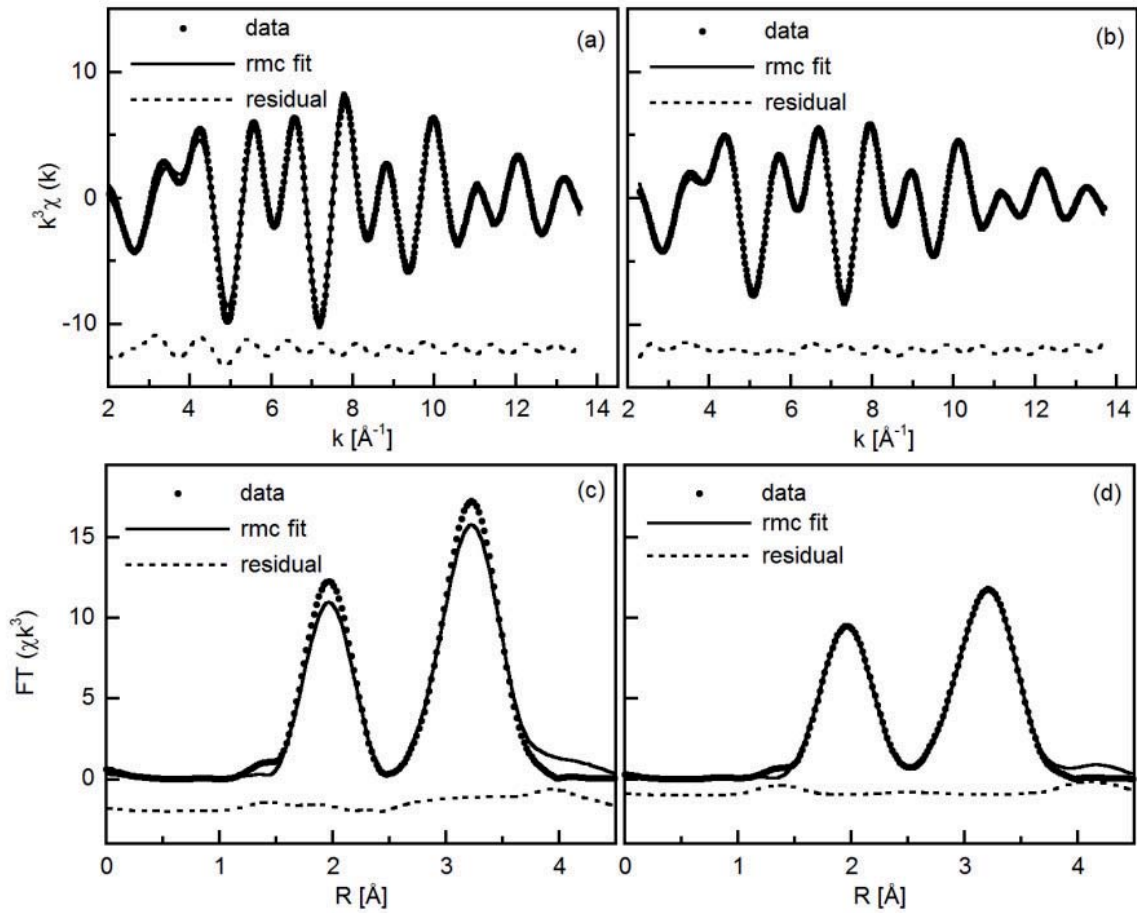


Fig. 4.59. RMC analysis of EXAFS spectra of $\text{Zn}_{0.80}\text{Co}_{0.20}\text{O}$ for Zn K -edge (a) and Co K -edge (b) and its phase corrected radial structure function on Zn K -edge (c) and Co K -edge (d).

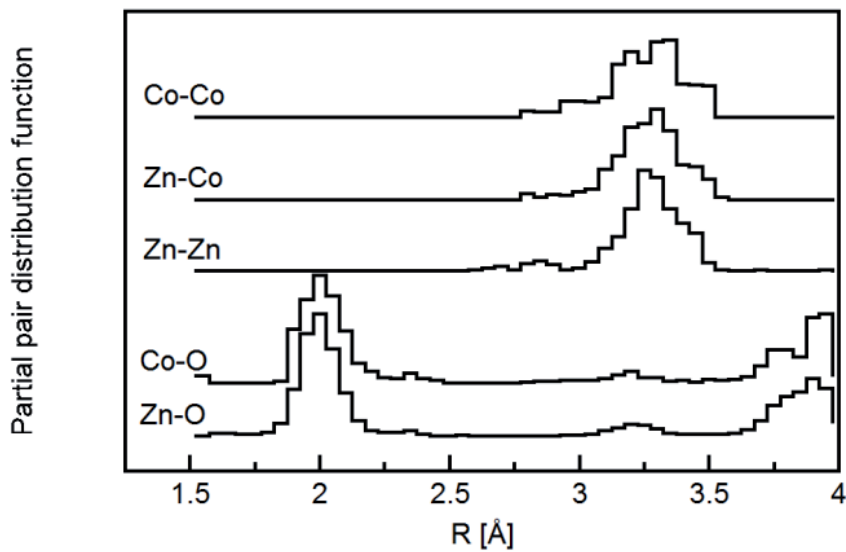


Fig. 4.60. Partial pair distribution functions for $\text{Zn}_{0.80}\text{Co}_{0.20}\text{O}$ derived from RMC

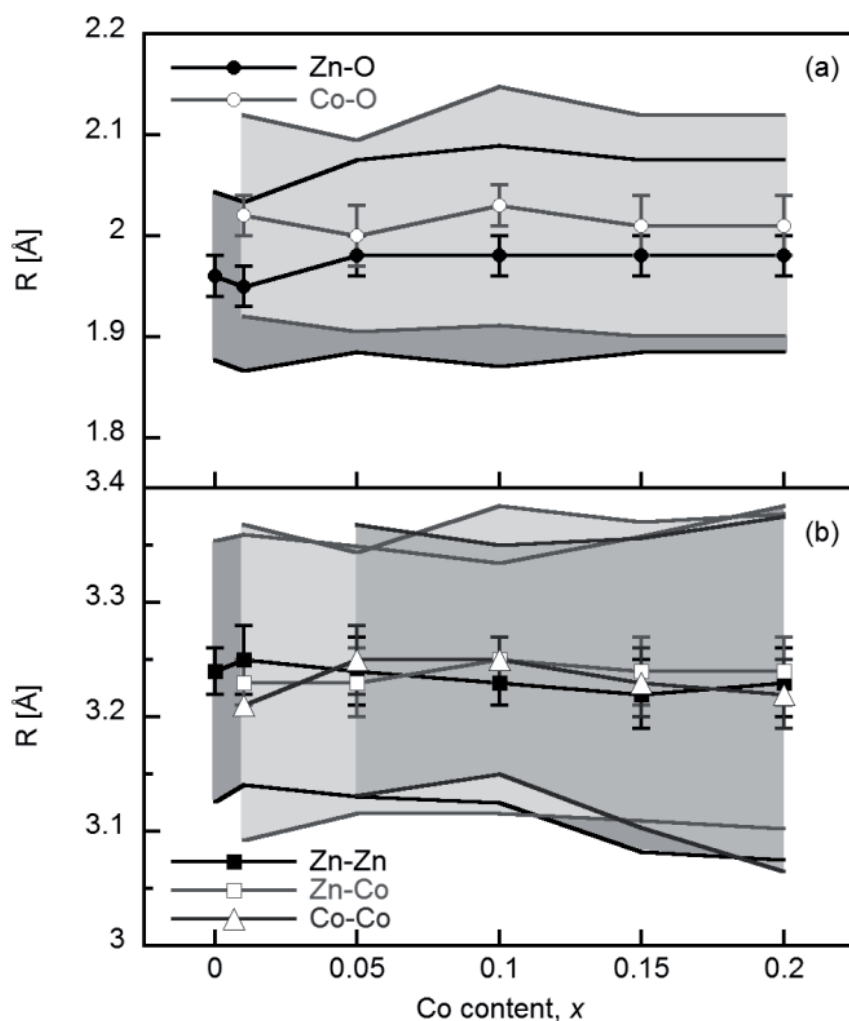


Fig. 4.61. Nearest (a) and next nearest (b) interatomic distances according to RMC data analysis as a function of Co content as determined from moment analysis of the corresponding partial pair distribution functions. The shaded areas represent the square root of the second moment ($R \pm p_2^{1/2}$ [\AA])

The Zn and Co K -edge EXAFS spectra for $\text{Zn}_{1-x}\text{Co}_x\text{O}$, as well as their Fourier transforms are shown in Fig. 4.58. From Fig. 4.58a and 4.58c, it can be seen that the spectra as well as the amplitude of the Fourier transforms for $\text{Zn}_{1-x}\text{Co}_x\text{O}$ are very close to that of pure ZnO indicating that Co is replacing Zn substitutionally. From the radial structure functions (no phase shift correction applied) of $\text{Zn}_{1-x}\text{Co}_x\text{O}$ (Fig. 4.58d) three peaks can be observed. The first peak at about 1.6 \AA is due to the Co–O coordination in the first shell, the second peak at about 2.5 \AA corresponds to the Zn(Co)–Zn coordination in the second shell, and the third at about 4 \AA arises from the third coordination shell comprising of nine oxygen atoms and multiple scattering. Positions and amplitude of the first and second peaks do not change significantly with increasing Co content.

Samples with $x \geq 0.01$ are analyzed using RMC (Fig. 59). The fits are in good agreement with the experimental data. The partial pair distribution functions deri-

Table 4.3. Results of EXAFS data analysis of $\text{Zn}_{1-x}\text{Co}_x\text{O}$ nanoparticles using *rmcxas* (N – the coordination number, R – the interatomic distance, p_2 – the second moment)

x (Co)	Shell	N	R [Å]	p_2 [10^{-3}Å^2]
0 (ZnO)	Zn–O	3.6(7)	1.96(2)	7(2)
	Zn–Zn	11(2)	3.24(2)	13(4)
0.01	Co–O	3.9(6)	2.02(2)	10(3)
	Co–Co	(0.06)	(3.21) ²	na
	Co–Zn	na ¹	na	na
	Zn–O	3.2(7)	1.95(2)	7(3)
	Zn–Co	0.12(2)	3.23(2)	19(5)
	Zn–Zn	9(2)	3.25(3)	12(4)
0.05	Co–O	4.0(9)	2.00(3)	9(5)
	Co–Co	0.38(8)	(3.25(3))	14(3)
	Co–Zn	na	na	na
	Zn–O	4.0(8)	1.98(2)	9(5)
	Zn–Co	0.7(1)	3.23(3)	13(4)
	Zn–Zn	11(3)	3.24(3)	12(5)
0.10	Co–O	4.0(6)	2.03(2)	14(5)
	Co–Co	1.1(2)	3.25(2)	10(3)
	Co–Zn	na	na	na
	Zn–O	3.8(7)	1.98(2)	12(6)
	Zn–Co	1.5(3)	3.23(2)	18(4)
	Zn–Zn	10(2)	3.23(2)	11(3)
0.15	Co–O	4.0(8)	2.01(3)	12(6)
	Co–Co	2.1(5)	3.23(3)	16(5)
	Co–Zn	na	na	na
	Zn–O	4.0(8)	1.98(2)	9(5)
	Zn–Co	2.0(4)	3.24(3)	17(6)
	Zn–Zn	10(2)	3.22(3)	19(9)
0.20	Co–O	4.0(8)	2.01(3)	12(6)
	Co–Co	2.6(5)	3.22(3)	24(8)
	Co–Zn	na	na	na
	Zn–O	4.0(8)	1.98(2)	9(5)
	Zn–Co	2.6(6)	3.24(3)	19(8)
	Zn–Zn	9(2)	3.23(3)	24(12)

ved from RMC analysis (Fig. 4.59) of the EXAFS spectra are shown in Fig. 4.60 for $\text{Zn}_{0.80}\text{Co}_{0.20}\text{O}$ as an example. The results of the RMC analysis (moment analysis of the partial pair distribution functions up to the second moment) are compiled in Table 4.3 for doped samples ($x \geq 0.01$) as well as pure ZnO and bulk reference samples (CoO and Co_3O_4). It can be seen (Table 4.3) that the interatomic distances of Co–O and Co–Zn in Co-doped ZnO samples are close to the Zn–O and Zn–Zn distances in pure ZnO in contrast to Liu et al. [Liu et al. 2008] who observed an

¹ not analyzed² the values in parentheses are only from one bin in the pair distribution function due to the low Co content

elongation of Co–O distances and a contraction of Co–Zn distances and explained it by a mismatch of Co^{2+} in the ZnO lattice. The partial pair distribution function (Fig. 4.60) for Co–Co, Co–Zn, and Zn–Zn overlap and are not split. This is evidence that Co^{2+} ions occupy tetrahedral Zn sites substitutionally in the ZnO wurtzite lattice for doping levels x below 0.20. Figure 4.61 displays the interatomic distances as a function of Co content as determined from the RMC analysis together with the second moment. The Co–O distances deviate systematically to marginally larger distances compared to Zn–O distances whereas the cationic distances overlap within the error bars. Both do not change as a function of Co content. Only the second moment increases slightly at higher Co contents which could be an indication for an onset of the phase transformation to rock salt structure at even higher Co contents or due to an increased static disorder.

4.3.4 Magnetic Properties

Figure 4.62 shows the temperature dependence of the magnetic susceptibility for $\text{Zn}_{1-x}\text{Co}_x\text{O}$ nanoparticles measured in an applied magnetic field of 200 Oe. Zero-field cooled and field cooled data display identical behavior over the entire temperature region indicating paramagnetic behavior. The susceptibility decreases rapidly up to 50 K for all samples. A linear behavior of the inverse susceptibility is clearly seen at elevated temperatures (150–320 K), Fig. 4.63. The linear fit by the Curie-Weiss law in this temperature region allows the determination of the Curie-Weiss temperatures, θ , and the effective magnetic moments, μ_{eff} . The effective magnetic moment (μ_{eff}) is derived using the equation [Culity and Graham 2009]:

$$\mu_{\text{eff}} = 2.83 \cdot \sqrt{C_M} \cdot \mu_B \quad (4.12)$$

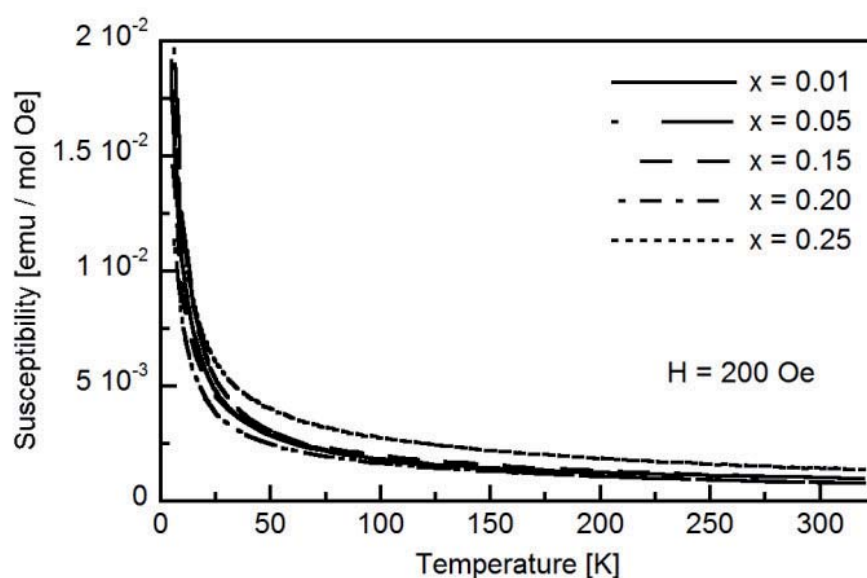


Fig. 4.62. Susceptibility of $\text{Zn}_{1-x}\text{Co}_x\text{O}$ nanoparticles as a function of temperature at 200 Oe

where C_M is the Curie constant per molecule [emu/mol Oe] obtained from the slope of inverse susceptibility vs. temperature curve above 150 K (see inset in Fig. 4.63 as an example), and μ_B is Bohr magneton. The large negative values of the Curie-Weiss temperatures (Fig. 4.64) indicate a strong antiferromagnetic coupling of Co atoms in $\text{Zn}_{1-x}\text{Co}_x\text{O}$ nanoparticles at lower temperatures. The resulting values of the effective magnetic moment of $2\mu_B$ (Fig. 4.65) are well below the expected value of $(3.87\mu_B)$ for tetrahedrally-coordinated high-spin Co^{2+} . According to Han et al. [Han et al. 2008] this is probably because not all the Co atoms are in the paramagnetic regime which indicates the existence of tiny amount

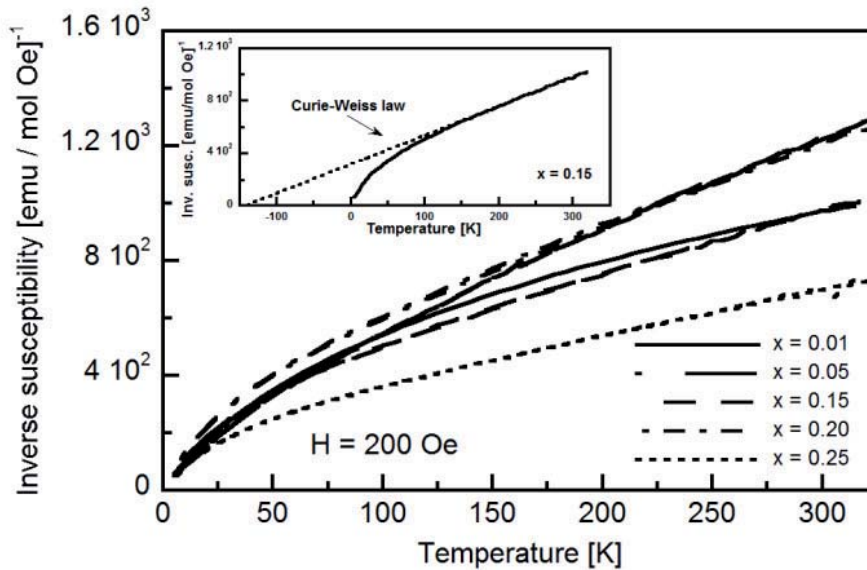


Fig. 4.63. Inverse susceptibility of $\text{Zn}_{1-x}\text{Co}_x\text{O}$ nanoparticles as a function of temperature at 200 Oe (inset: Curie-Weiss fit for $\text{Zn}_{0.85}\text{Co}_{0.15}\text{O}$ sample)

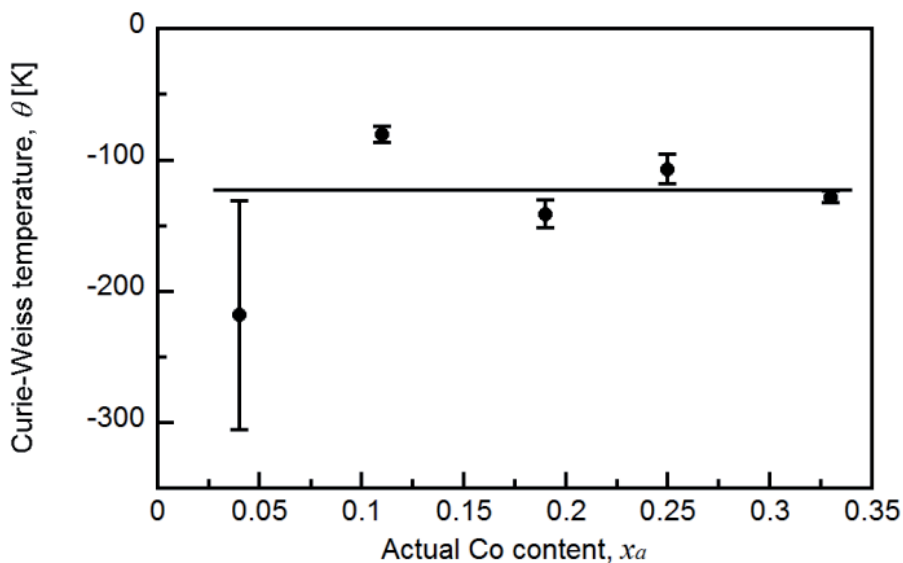


Fig. 4.64. Curie-Weiss temperature (obtained by applying Curie-Weiss law to the inverse susceptibility data at 200 Oe) as a function of actual Co content

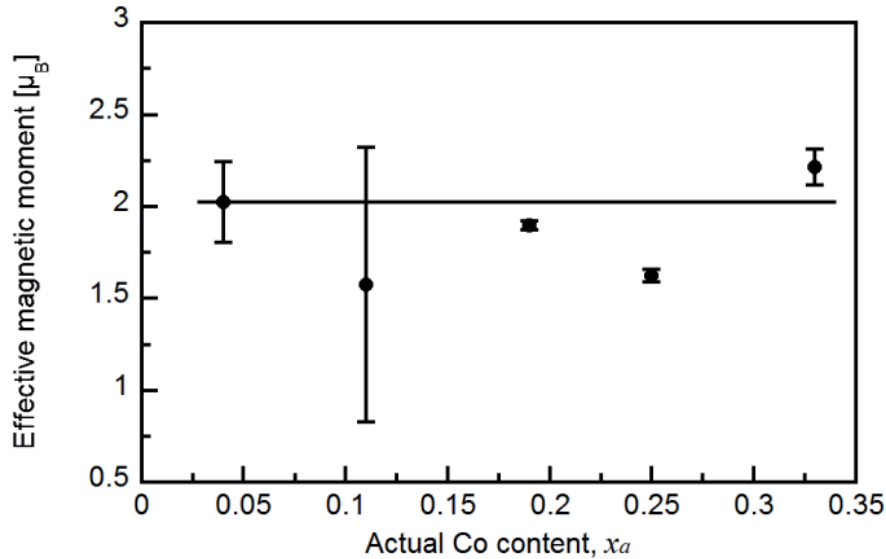


Fig. 4.65. Effective magnetic moment (Eq. 4.12) as a function of actual Co content

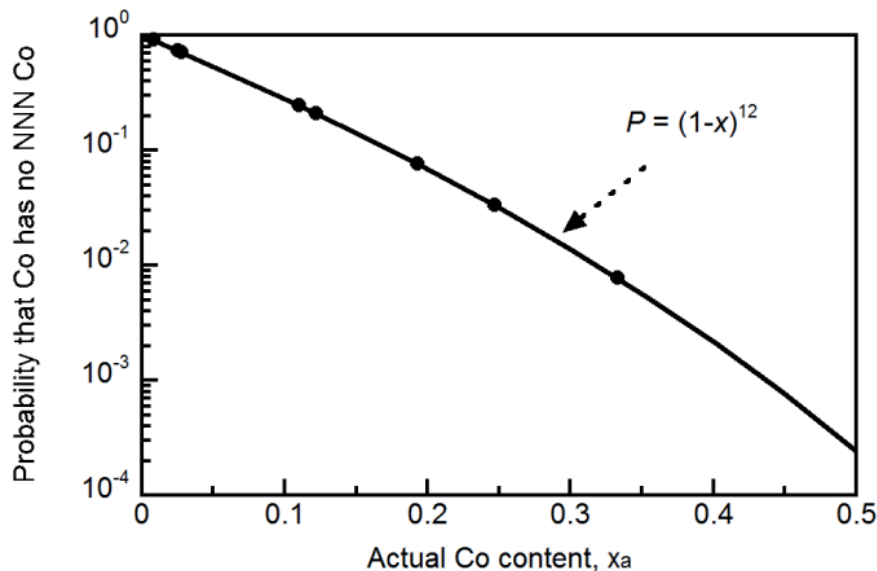


Fig. 4.66. Probability that Co has no Co for a next nearest neighbor (NNN) as a function of Co content in Co-doped nanoparticles

of an antiferromagnetic CoO phase. As the detailed structural study on $\text{Zn}_{1-x}\text{Co}_x\text{O}$ samples (see for example Fig. 4.57 and related discussion) excluded the existence of CoO in these samples, this explanation can be ruled out. Recently Lv et al. [Lv et al. 2008] reported similar results for single crystalline samples. The possibility of a antiferromagnetic coupling of nearest-neighbor Co spins has been reported by Yin et al. [Yin et al. 2006]. From the probability that Co has no Co as next nearest neighbor (NNN) calculated using the expression $P = (1-x)^{12}$ [Behringer 1958] and shown in Fig. 4.66 it can be seen that even at low Co content there is a low but finite probability that Co can have Co as a next nearest neighbor. With increasing the Co content, the probability is increasing which may explain the observed antiferromagnetic interactions in the studied samples.

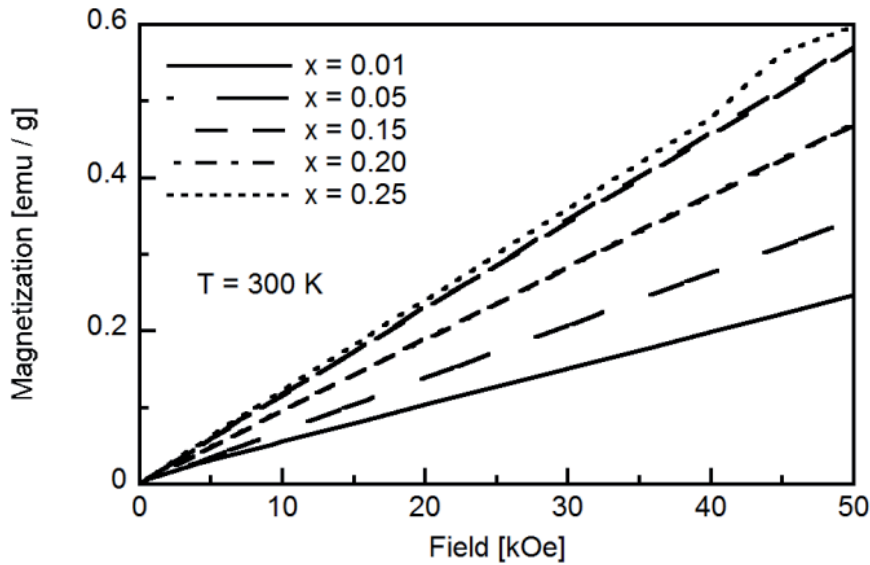


Fig. 4.67. Field-dependent magnetization of $\text{Zn}_{1-x}\text{Co}_x\text{O}$ nanoparticles at 300 K

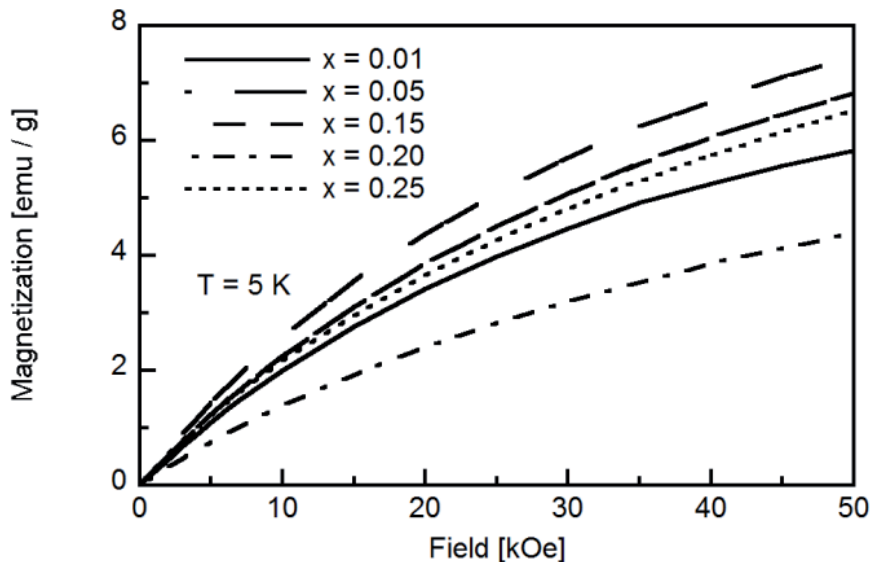


Fig. 4.68. Field-dependent magnetization of $\text{Zn}_{1-x}\text{Co}_x\text{O}$ nanoparticles at 5 K

The magnetization curves measured at 300 K and 5 K are presented in Figs. 4.67 and 4.68, respectively. No hysteresis was found even down to 5 K indicating the absence of intrinsic ferromagnetism in the studied samples. These curves are a typical feature of paramagnetic samples and have been observed for all studied cobalt concentrations. The magnetic moment at 50 kOe increases with increasing Co content at room temperature, while at 5 K it is decreasing (Fig. 4.69), indicating an antiferromagnetic interaction between Co ions. Measuring the magnetic-field dependence of magnetization at various temperatures (Fig. 4.70) it is found that Co atoms (sample $\text{Zn}_{0.85}\text{Co}_{0.15}\text{O}$) start to couple antiferromagnetically at temperatures below 19 K. Coey et al. [Coey et al. 2005] suggest that the concentration of magnetic cations should be below the cation nearest-neighbor percolation threshold ($x = 0.18$) in order to avoid antiferromagnetic or-

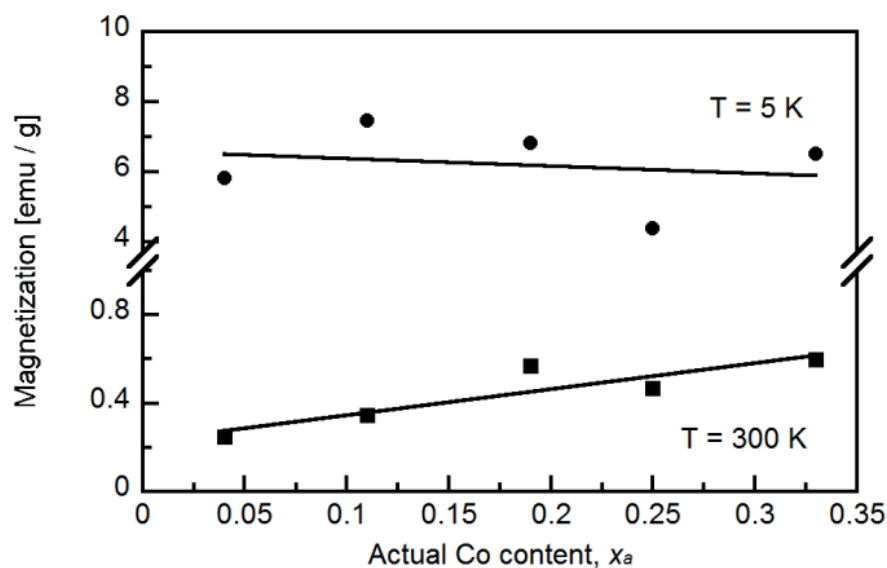


Fig. 4.69. Magnetization at 50 kOe extracted from the field-dependent magnetization data at 300 K and 5 K as a function of actual Co content

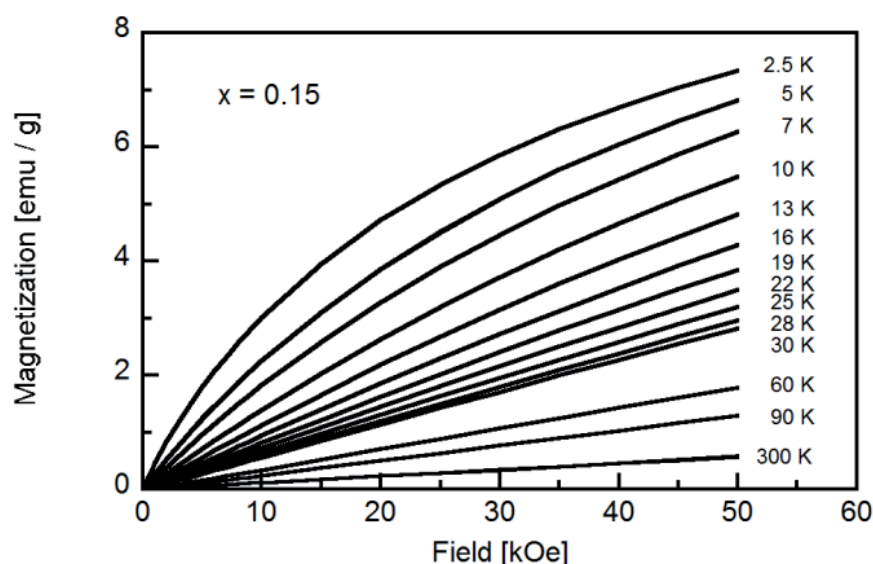


Fig. 4.70. Field-dependent magnetization for a sample with nominal Co content of $x = 0.15$ measured at different temperatures

dering in TM-doped ZnO. The absence of magnetic ordering in our samples, with Co content ($x = 0.01$ and 0.05) below the percolation threshold for cation-cation nearest-neighbor interaction, provides evidence that the magnetic interactions are dominated by the nearest-neighbor antiferromagnetic interactions, suggesting that the condition proposed by Coey et al. (mention above) is not sufficient to induce ferromagnetism in case of Co doped ZnO. Contrary to Coey et al. [Coey et al. 2005], Lee et al. [Lee et al. 2004] found a short range nature in both antiferromagnetic and ferromagnetic interactions, and suggest that a very high doping level of Co ions is required to achieve ferromagnetism, together with a sufficient supply of electron carriers. The absence of ferromagnetic ordering even in samples with

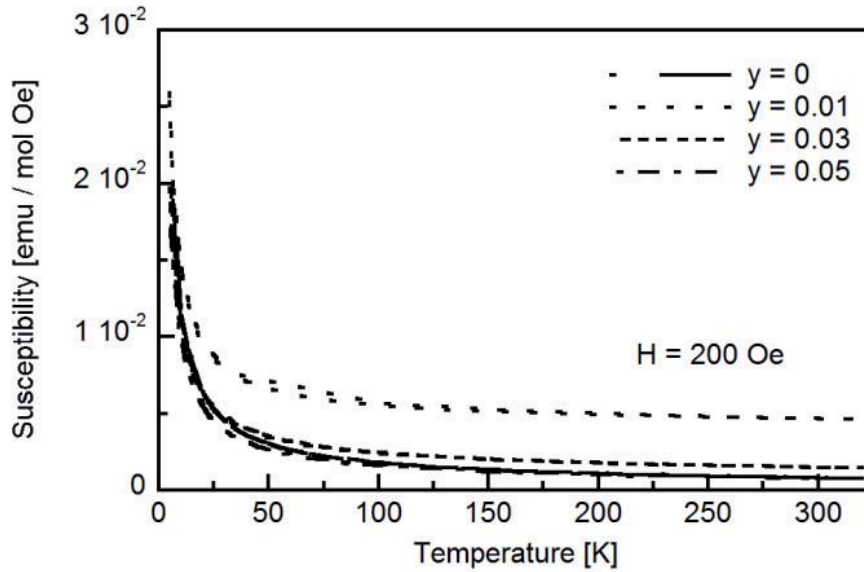


Fig. 4.71. Temperature dependence of the susceptibility of $\text{Zn}_{0.95-y}\text{Co}_{0.05}\text{Li}_y\text{O}$ nanoparticles

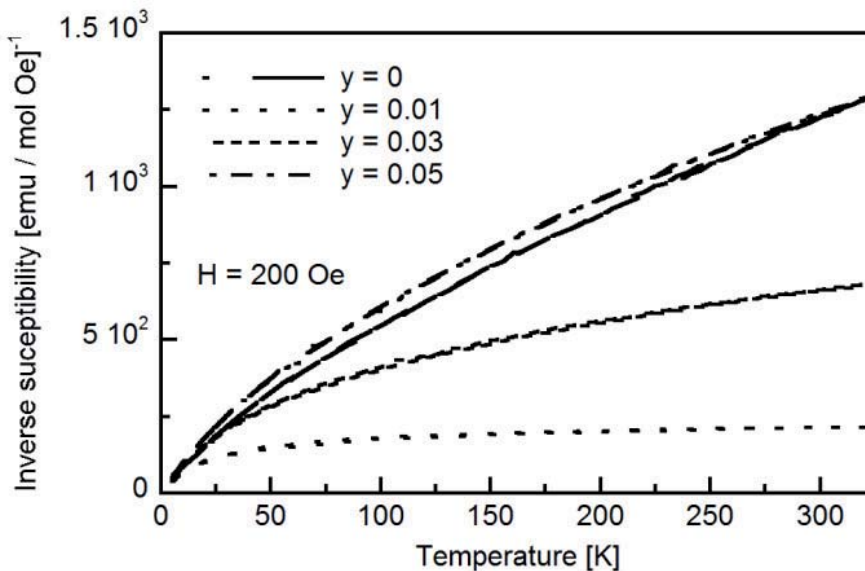


Fig. 4.72. Temperature dependence of the inverse susceptibility of $\text{Zn}_{0.95-y}\text{Co}_{0.05}\text{Li}_y\text{O}$ nanoparticles

high Co content ($x = 0.15\text{--}0.25$) leads to the conclusion that even high dopant concentrations are not sufficient to induce ferromagnetic ordering in Co-doped ZnO. A similar observation was reported by Kaspar et al. [Kaspar et al. 2008].

Temperature dependent magnetization measurements performed on Li-doped $\text{Zn}_{0.95}\text{Co}_{0.05}\text{O}$ nanoparticles ($\text{Zn}_{0.95-y}\text{Co}_{0.05}\text{Li}_y\text{O}$, $y = 0\text{--}0.05$) are presented in Figs. 4.71 and 4.72. The curves show a similar trend as it was observed for particles without Li (Figs. 4.61 and 4.62). Field-dependent magnetization data obtained at 300 K and 5 K (Figs. 4.73 and 4.74) show the absence of ferromagnetism similarly to nanoparticles containing no Li. Although, the ferromagnetism due to additional free charge carriers when Li is introduced in Co-doped ZnO nanopar-

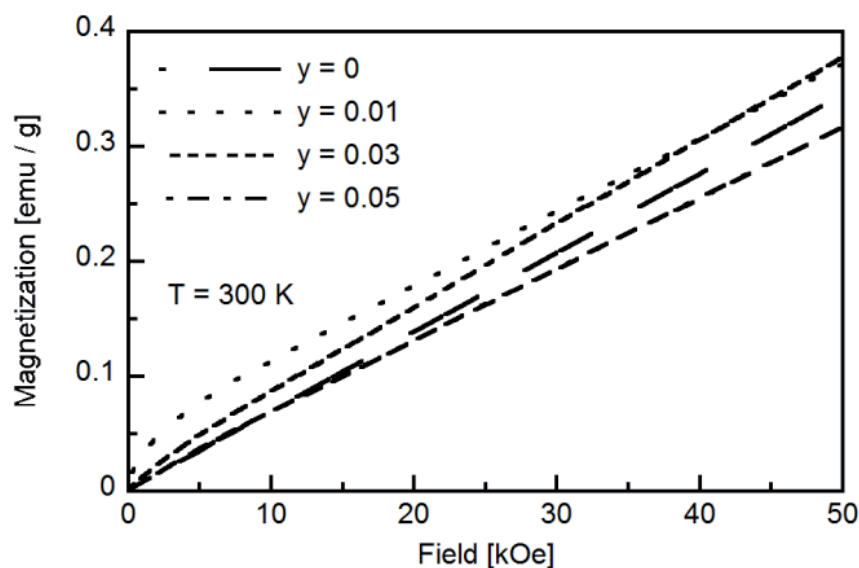


Fig. 4.73. Field-dependent magnetization of $\text{Zn}_{0.95-y}\text{Co}_{0.05}\text{Li}_y\text{O}$ nanoparticles at 300 K

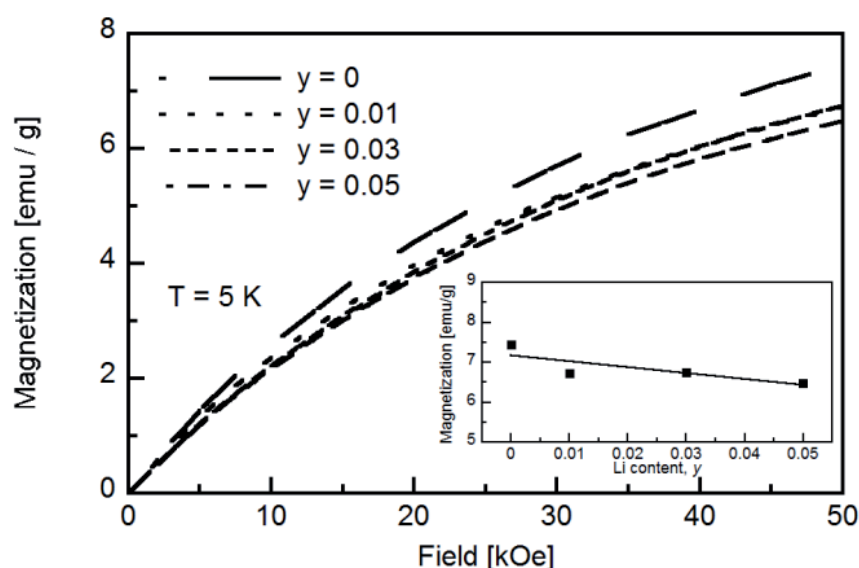


Fig. 4.74. Field-dependent magnetization of $\text{Zn}_{0.95-y}\text{Co}_{0.05}\text{Li}_y\text{O}$ nanoparticles at 5 K (inset: Magnetization as a function of Li content)

ticles was reported [Yi et al. 2010, Sluiter et al. 2005], the results presented here show that Li did not promote ferromagnetic coupling of Co^{2+} . On the contrary, the antiferromagnetic coupling becomes stronger. This observation is in agreement with the most recent theoretical calculation by Assadi et al. [Assadi et al. 2010]. Namely, Co ions in Co-doped ZnO couple AFM and oxygen vacancies, due to incorporation of Li, stabilize the antiferromagnetic coupling between Co ions. According to their study, the ferromagnetic phase stabilization can occur only in the presence of hydrogen impurities regardless of doping.

From the results presented here, the intrinsic ferromagnetism in ZnO nanoparticles cannot be induced neither by Co-doped nor by Co,Li-doped suggesting that most probably the ferromagnetism has an extrinsic origin, i.e. in second phases.

4.3.5 Conclusion

A high solubility of cobalt in ZnO is achieved using chemical vapor synthesis, as $\text{Zn}_{1-x}\text{Co}_x\text{O}$ nanoparticles for Co contents of up to $x_a = 0.33$ (according to chemical analysis) are of single wurtzite phase. The crystallographic structural parameters vary continuously with increasing Co content due to the increasing crystallite size. The cause for the increase of crystallite size is the enhanced evaporation rate of the precursor mixture due to a stronger absorption of the laser light by the Co precursor compared to the Zn precursor. Therefore, the observed subtle but significant variations of the structural parameters are due to the decreasing surface to volume ratio with increasing particle size.

Despite the fact that several conditions (low and high dopant content, codoping) for achieving the ferromagnetism in the semiconducting ZnO were fulfilled, no ferromagnetism or any other cooperative magnetism was observed. This leads to the conclusion that structural defects or phase segregation most probably play a significant role in achieving the ferromagnetism in TM-doped ZnO.

5 Conclusions

The systematic study conducted in this work showed that the characteristics of nanocrystalline particles produced by chemical vapor synthesis are sensitive to the time-temperature history in the gas phase of the reactor. High temperatures are necessary for a complete coalescence of the primary particles inside the agglomerates. Fast quenching at the end of the reactor is essential for the prevention of extensive formation of hard agglomerates. In chemical vapor synthesis, not only the particle size and degree of agglomeration can be controlled, but also the degree of crystallinity as well as the microstrain. A hot-wall reactor based on an induction furnace was constructed which provides a flexibility in designing different temperature profiles in order to optimize the characteristics of nanoparticles.

A novel method, pulsed precursor delivery using a laser flash evaporator, was developed to feed precursors into a CVS reactor. The pulsed precursor delivery showed so far only limited influence on the width of the particle size distribution, but a significant impact on the reduction of the particle size and the degree of agglomeration. The laser pulse repetition frequency had only little influence on particle size and the size distribution. On the other hand, it is possible to lower the particle number concentration and consequently to reduce the final particle size and the width of the particle size distribution by decreasing the laser duty cycle. The degree of agglomeration can be significantly reduced by using a lower duty cycle.

Detailed analysis of both crystallographic and local structure provides evidence that it is possible to prepare nanocrystalline ZnO particles by chemical vapor synthesis where Co is substituting Zn in the wurtzite lattice which is a key requirement for the development of dilute magnetic semiconductors based on Co-doped ZnO. The method of particle production plays a very important role in obtaining Co-doped ZnO powders of high homogeneity. Chemical vapor synthesis, as a nonequilibrium process where precursors are mixed on the molecular level in the gas phase, provides the possibility to prepare such samples. Laser flash evaporation can be successfully used to prepare solid solutions of CoO-ZnO with Co content up to 33 at. % without the formation of second phases. Even more complex systems ($\text{Zn}_{1-x-y}\text{Co}_x\text{Li}_y\text{O}$) can be prepared using this method with controlled powder stoichiometry.

6 References

- Adamopoulos, G., Bashir, A., Thomas, S., Gillin, W. P., Georgakopoulos, S., Shkunov, M., Baklar, M. A., Stingelin, N., Maher, R. C., Cohen, L. F., Bradley, D. D. C., and Anthopoulos, T. D., *Adv. Mater.*, **22** (2010) 4764.
- Aksenov, V. L., Kuzmin, A. Yu., Purans, J., and Tyutyunnikov, S. I., *Phys.Part. Nuclei*, **32** (2001) 1.
- Ankudinov, A. L., Ravel, B., Rehr, J. J., Albers, R. C., and Conradson, S. D., *Phys. Rev., B* **58** (1998) 7565.
- Assadi, M. H. N., Zhang, Y. B., and Li, S., *J. Phys.: Condens. Matter*, **22** (2010) 296004.
- Behan, A. J., Mokhtari, A., Blythe, H. J., Score, D., Xu, X.-H., Neal, J. R., Fox, A. M., and Gehring, G. A., *Phys. Rev. Lett.*, **100** (2008) 047206.
- Behringer, R. E., *J. Chem. Phys.*, **29** (1958) 537.
- Blasco, J., Bartolome, F., Garcia L. M., and Garcia, J., *J. Mater. Chem.*, **16** (2006) 2282.
- Bouloudenine, M., Viart, N., Colis, S., Kortus, J., and Dinia, A., *Appl. Phys. Lett.* **87** (2005) 052501.
- Brehm, J. U., Winterer, M., and Hahn, H. *J. Appl. Phys.*, **100** (2006) 064311.
- Cao, G., *Nanostructures and Nanomaterials – Synthesis, Properties and Applications*, Imperial college Press, London, **2004**.
- Chambers, S. A., Droubay, T. C., Wang, C. M., Rosso, K. M., Heald, S. M., Schwartz, D. A., Kittilstved, K. R., and Gamelin, D. R., *Mater. Today* **9** (2006) 28.
- Chappell, J. S., Ring, T. A., and Birchall, J. D., *J. Appl. Phys.*, **60** (1986) 383.
- Chen, X., and Mao, S. S., *Chem. Rev.*, **107** (2007) 2891.
- Chiang, Y.-M., Birnie, D., and Kingery, W. D., *Physical Ceramics – Principles for Ceramic Science and Engineering*, John Wiley & Sons, Inc., **1997**.
- Coey, J. M. D., Venkatesan, M., and Fitzgerald, C. B., *Nat. Mater.*, **4** (2005) 173.
- Combe, N., Chassaing, P. M., and Demangeot, F., *Phys. Rev. B*, **79** (2009) 045408.
- Cong, C. J.; Hong, J. H.; Liu, Q. Y.; Liao, L.; and Zhang, K. L., *Solid State Commun.* **2006**, *138*, 511.
- Cullity, B. D., and Graham, C. D., *Introduction to Magnetic Materials*, 2nd Ed., John Wiley & Sons, Hoboken, New Jersey, **2009**.
- Deka, S., Pasricha, R., and Joy, A. P., *Phys. Rev., B* **74** (2006) 033201.
- Deka, S., Pasricha, R., and Joy, P. A., *Chem, Mater.*, **16** (2004) 1168.
- Desgreniers, S. *Phys. Rev. B* **58** (1998) 14102.
- Dietl, T., Ohno, H., Matsukura, F., Cibert, J., and Ferrand, D., *Science*, **287** (2000), 1019.
- Dobbins, R. A., and Megarids, C. M., *Langmuir* **3** (1987) 254.
- Duan, L. B., Chu, W. G., Yu, J., Wang, Y. C., Zhang, L. N., Liu, G. Y., Liang, J. K., and Rao, G. H., *J. Magn. Magn. Mater.*, **320** (2008) 1573.
- Flagan, R. C., and Lunden, M. M., *Mat. Sci. and Eng., A* **204** (1995) 113.
- Friedlander, S. K., *Smoke, Dust, and Haze – Fundamentals of Aerosol Dynamics*, 2nd Ed., Oxford University Press, **2000**.

- Ganić, E. N., and Hicks, T. G., *McGraw-Hill's Engineering Companion*, McGraw-Hill Companies, Inc., USA, **2003**.
- Gaudon, M., Toulemonde, O., Demourgues, A., *Inorg. Chem.*, **46** (2007) 10996.
- Givord, D., "Magnetism in Nanomaterials" in *Nanomaterials and Nanochemistry*, Bréchnignac, C., Houdy, P., Lahmani, M., Springer, Berlin, **2006**.
- Gopal, P., and Spaldin, N. A., *Phys. Rev. B*, **74** (2006) 094418.
- Grass, R. N., Tsantilis, S., and Pratsinis, S. E., *AIChE Journal* **52** (2006) 1318.
- Gribb, A. A., and Banfield, J. F., *Amer. Mineral.*, **82** (1997) 717.
- Han, A. R., Hwang, S.-J., Zhao, Y., and Kwon, Y.-U., *J. Magn. Magn. Mater.*, **290** (2008) 168.
- Hanaor, D. A. H., and Sorrell, C. C., *J. Mater. Sci.*, **46** (2011) 855.
- Hinds, W. C. "Physical and Chemical Changes in the Particulate Phase" in *Aerosol Measurement*, Baron, P. A., Willeke, K., Eds., John Wiley & Sons: New York, **2001**.
- Holman, J. P., *Experimental Methods for Engineers*, McGraw-Hill, **2001**.
- Hornyak, G. L., Dutta, J., Tibbals, H. F., Rao, A. K., *Introduction to Nanoscience*, CRC Press, Boca Raton, USA, **2008**.
- Jayaram, V., Rajkumar, J., Rani, B. S., *J. Am. Ceram. Soc.*, **82** (1999) 473.
- Jin, W., Lee, I.-K., Kompch, A., Dörfler, U., and Winterer, M., *J. Eur. Ceram. Soc.* **27** (2007), 4333.
- Jin, Z., Fukumura, T., Kawasaki, M., Ando, K., Saito, H., Sekiguchi, T., Yoo, Y. Z., Murakami, M., Matsumoto, Y., Hasegawa, T., and Koinuma, H., *Appl. Phys. Lett.* **78** (2001) 3824.
- Jongen, N., Donnet, M., Bowen, P., Lemaitre, J., Hofmann, H., Schenk, R., Hofmann, C., Aoun-Habbache, M., Guillemet-Fritsch, S., Sarrias, J., Rousset, A., Viviani, M., Buscaglia, M. T., Buscaglia, V., Nanni, P., Testino, A., and Herguiejuela, J. R., *Chem. Eng. Techn.* **26** (2003) 303.
- Kammler, H. K., Mädler, L., and Pratsinis, S. E., *Chem. Eng. Techn.*, **24** (2001) 6.
- Kim, M., Hong, Y. J., Yoo, J., Yi, G.-C., Park, G.-S., Kong, K.-J., Chang, H., *Phys. Stat. Sol.* **2** (2008) 197.
- Kim, Y.-I., Page, K., Seshadri, R., *Appl. Phys. Lett.* **90** (2007) 101904.
- Kittel, C., *Introduction to Solid State Physics*, 5th ed., Wiley, **1976**.
- Kleiner, R., Koelle, D., Ludwig, F., and Clarke, J., *Proceedings of the IEEE*, **92** (2004) 1534.
- Kodas, T. T., and Friedlander, S. K., *AIChE J.*, **34** (1998) 551.
- Kodas, T. T., and Hampden-Smith, M., *Aerosol Processing of Materials*, Wiley-VCH, **1999**.
- Kolesnik, S., Dabrowski, B., and Mais, J., *J. Appl. Phys.* **95** (2004) 2582.
- Koningsberger, D. C., Mojet, B. L., Dorssen, G. E. van, and Ramaker, D. E., *Topics in Catalysis* **10** (2000) 143.
- Kruis, F. E., Krusters, K. A., Pratsinis, S. E., and Scarlett, B., *Aerosol Sci. Techn.*, **19** (1993) 514.
- Kuhn, H., and Försterling, H.-D., *Principles of Physical Chemistry – Understanding Molecules, Molecular Assemblies, Supramolecular Machines*, John Wiley & Sons, Chichester, UK, **2000**.
- Lakshmi, Y. K., Srinivas, K., Sreedhar, B., Raja, M. M., Vithal, M., and Reddy, P. V., *Mater. Chem. Phys.*, **113** (2009) 749.
- Lee, E.-C., and Chang, K. J., *Phys. Rev. B*, **69** (2004) 085205.
- Lee, H.-J., Jeong, S.-Y., Cho, C. R., and Park, C. H., *App. Phys. Lett.*, **81** (2002) 4020.

- Levenspiel, O., *Chemical Reaction Engineering*, 3rd ed., John Wiley & Sons, USA, **1999**.
- Liao, S.-C., Mayo, W. E., and Pae, K. D., *Acta Mater.*, **45** (1997) 4027.
- Liao, S.-C., Pae, K. D., and Mayo, W. E., *Nanostruct. Mater.*, **5** (1995) 319.
- Liu, T.; Xu, H.; Chin, W. S.; Yong, Z.; and Wee, A. T. S., *J. Phys. Chem. C*, **112** (2008) 3489.
- Lowell, S., Shields, J. E., Thomas, M. A., and Thommes, M., *Characterization of Porous Solids and Powders: Surface Area, Pore Size and Density*, Kluwer Academic Publishers, Dordrech, The Netherlands, **2004**.
- Lutterotti, L., and Scardi, P., *J. Appl. Crystallogr.*, **23** (1990) 246.
- Lv, P., Huang, F., Chu, W., Lin, Z., Chen, D., Li, W., Chen, D., and Wu, Z., *J. Phys.: Condens. Matter*, **20** (2008) 035206.
- Maira, A. J., Yeung, K. L., Lee, C. Y., Yue, P. L., and Chan, C. K., *J. Catal.*, **192** (2000) 185.
- Martinez, B., Sandiumenge, F., Balcells, L., Fontcuberta, J., Sibieude, F., and Monty, C., *J. Appl. Phys.*, **97** (2005) 10D311.
- McElfresh, M., *Fundamentals of Magnetism and Magnetic Measurement – Featuring Quantum Design’s Magnetic Property Measurement System*, Quantum Design, **1994**.
- Nakaso, K., Okuyama, K., Shimada, M., and Pratsinis, S. E., *Chem. Eng. Sci.*, **58** (2003) 3327.
- Nayak, S. K., Ogura, M., Hucht, A., Buschmann, S., Akai, H., and Entel, P., *Phys. Stat. Sol. (a)* **205** (2008) 1839.
- Newille, M., *Fundamentals of XAFS*, University of Chicago, IL, **2004**.
- Ney, A., Ollefs, K., Ye, S., Kammermeier, T., Ney, V., Kaspar, T. C., Chambers, S. A., Wilhelm, F., and Rogalev, A., *Phys. Rev. Lett.*, **100** (2008) 157201.
- Norton, D. P., Overberg, M. E., Pearton, S. J., Pruessner, K., Budai, J. D., Boatner, L. A., Chisholm, M. F., Lee, J. S., Khim, Z. G., Park, Y. D., and Wilson, R. G., *Appl. Phys. Lett.*, **83** (2003) 5488.
- O’Regan, B., and Grätzel, M., *Nature* **353** (1991) 737.
- Okuyama, K., Ushio, R., Kousaka, Y., Flagan, R. C., and Seinfeld, J. H., *AIChE J.*, **36** (1990) 409.
- Omega “Non-Contact Temperature Measurements” in *Transactions in Measurement and Control*, Vol. 1, Omega.com, **1998**.
- Owen, T., *Fundamentals of UV-Visible Spectroscopy*, Agilent Technologies, Germany, **2000**.
- Özgür, Ü. Alivov, Ya. I., Liu, C., Teke, A., Reshchikov, M. A., Doğan, S., Avrutin, V., Cho, S.-J., and Morkoç, H., *J. Appl. Phys.*, **98** (2005) 041301.
- Park, J. H., Kim, M. G., Jang, H. M., Ryu, S., and Kim, Y. M., *Appl. Phys. Lett.* **84** (2004) 1338.
- Pecharsky, V. K., and Zavalij, P.Y., *Fundamentals of Powder Diffraction and Structural Characterization of Materials*, Springer, **2009**.
- Pen, R. L., and Banfield, J. F., *Amer. Mineral.*, **83** (1998) 1077.
- Penner-Hahn, J. E., “X-ray Absorption Spectroscopy” in *Comprehensive Coordination Chemistry II*, Vol. 2, Editors: McCleverty, J. A., and Meyer, T. J., Elsevier, **2004**.
- Pereira, N. E., and Ni, X. W., *Chem. Eng. Sci.* **56** (2001) 735.
- Pratsinis, S. E., Vemury, S., *Powder Techn.*, **88** (1996) 267.
- Ranade, M. R., Navrotsky, A., Zhang, H. Z., Banfield, J. F., Elder, S. H., Zaban, A., Borse, P. H., Kulkarni, S. K., G. S. Doran, and H. J. Whitfield, *PNAS*, **99** (2001) 6476.

- Reimer, I., and Kohl, H., *Transmission Electron Microscopy - Physics of Image Formation*, 5th Ed., Springer, New York, **2008**.
- Rietveld, M. H., *J. Appl. Cryst.*, **2** (1969) 65.
- Risbud, A. S., Spaldin, N. A., Chen, Z. Q., Stemmer, S., and Seshadri, R. *Phys. Rev. B*, **68** (2003) 205202.
- Rodriguez, J. A. and Fernandez-Garcia, M., *Synthesis, Properties and Applications of Oxide Nanomaterials*, Wiley-Interscience, **2007**.
- Sandratskii, L. M., and Bruno, P., *Phys. Rev. B*, **73** (2006) 045203.
- Sato, K., and Katayama-Yoshida, H., *Physica E* **10** (2001) 251.
- Schaedler, T. A., Gandhi, A. S., Saito, M., Rühle, M., Gambino, R., and Levi, C. G. *J. Mater. Res.*, **12** (2006) 791.
- Schmidt-Mende, L., and MacManus-Driscoll, J. L., *Mat. Today* **10** (2007) 40.
- Shannon, R. D. *Acta Crystallogr., Sect. A*, **32** (1976) 751.
- Sharma, P., Gupta, A., Owens, F. J., Sharma, R., Ahuja, R., Osorio Guillen, J. M., Johansson, B., Gehring, G. A., and Rao, K. V., *Nat. Mater.*, **2** (2003) 673.
- Shriver, D., and Atkins, P., *Inorganic Chemistry*, 3rd. Ed., Freeman, New York, **1999**.
- Silva, J. R. G., *Interciencia* **19** (1997) 171.
- Sluiter, M. H. F., Kawazoe, Y., Sharma, P., Inoue, A., Raju, A. R., Rout, C., and Waghmare, U. V., *Phys. Rev. Lett.*, **94** (2005) 187204.
- Srinivasan, G., Kumar, R. T. R., and Kumar, G. J., *J. Sol-Gel Sci. Technol.*, **43** (2007) 171.
- Stern, E. A., "Theory of EXAFS" in *X-ray Absorption: Principles, Applications, Techniques of EXAFS, SEXAFS and XANES*, Koningsberger, D. C., and Prins, R., Eds., John Wiley, New York, **1988**.
- Straumal, B. B., Mazilkin, A. A., Protasova, S. G., Myatev, A. A., Straumal, P. B., Schütz, G., van Aken, P. A., Goering, E., and Baretzky, B., *Phys. Rev. B*, **79** (2009) 205206.
- Straumal, B. B., Mazilkin, A. A., Protasova, S. G., Myatev, A. A., Straumal, P. B., and Baretzky, B., *Acta Mater.*, **56** (2008) 6246.
- Straumal, B., Baretzky, B., Mazilkin, A., Protasova, S., Myatev, A., and Straumal, P., *J. Eur. Ceram. Soc.*, **29** (2009) 1963.
- Sun, Z., Yan, W., Zhang, G., Oyanagi, H., Wu, Z., Li, Q., Wu, W., Shi, T., Pan, Z., Xu, P., and Wei, S. *Phys. Rev. B*, **77** (2008) 245208.
- Ting, J.-M., and Lin, R. Y., *J. Mater. Sci.*, **30** (1995) 2382.
- Tsantilidis, S., and Pratsinis, S. E., *Langmuir* **20** (2004) 5933.
- Tsantilidis, S., Kammler, H. K., and Pratsinis, S. E., *Chem. Eng. Sci.*, **57** (2002) 2139.
- Tscharnauter, W., "Photon Correlation Spectroscopy in Particle Sizing" in *Encyclopedia of Analytical Chemistry*, Meyers, R. A., Ed., John Wiley & Sons, **2000**.
- Tsureka, S., and Yoshinaga, H., *Grain Boundary Controlled Properties of Fine Ceramics*, Ishizaki, K., Nihara, K., Isotani, M., and Ford, R., G., Eds., Elsevier, London, **1992**.
- Ueda, K., Tabata, H., and Kawai, T., *Appl. Phys. Lett.*, **79** (2001) 988.
- Vanvor, H., "Thermocouples" in *Sensors – A comprehensive Survey*, Göpel, W., Hesse, J., and Zemel, J. N., Eds., VCH, Weinheim, Germany, **1989**.
- Vayssieres, L., "On Aqueous Interfacial Thermodynamics and the Design of Metal-Oxide Nanostructures" in *Synthesis, Properties, and Applications of Oxide Nanomaterials*, Rodríguez J. A., and Fernández-Garcia, M., Eds., JohnWiley & Sons, Inc., **2007**.
- Vollath, D., *Nanomaterials: An Introduction to Synthesis, Properties and Application*, Wiley-VCH, Weinheim, Germany, **2008**.
- Winterer, M., *J. Appl. Phys.*, **88** (2000) 5635.
- Winterer, M., *J. Phys. IV* **7** (1997) C2–243.

- Winterer, M., *Nanocrystalline Ceramics - Synthesis and Structure*, Springer Verlag, Berlin, **2002**.
- Winterer, M., Srdic, V. V., Djenadic, R., Kompch, A., Weirich, T. E. *Rev. Sci. Instrum.*, **78** (2007) 123093.
- Woltersdorf, J., Nepijko, A. S., and Pippel, E., *Surf. Sci.* **106** (1981) 64.
- Yang, J. H., Zhao, L. Y., Ding, X., Yang, L. L., Zhang, Y. J., Y. X. Wang and H. L. Liu, *Mater. Sci. Eng., B* **162** (2009) 143.
- Yin, S., Xu, M. X., Yang, L., Liu, J. F., Rösner, Hahn, H. H., Gleiter, H., Schild, D., Doyle, S., Liu, T., Hu, T. D., Takayama-Muromachi, E., and Jiang, J. Z., *Phys. Rev. B*, **73** (2006) 224408.
- Young, R. A., *The Rietveld Method*, Oxford University Press, **1995**.
- Zhang, H., and Banfield, J., *J. Mater. Chem.*, **8** (1998) 2073.
- Zhang, J., Li, M., Feng, Z., Chen, J., and Li, C., *J. Phys. Chem. B* **110** (2006) 927.

7 Appendix

Table A. Measured wall temperatures for the ‘flat’ temperature profile configuration (Ch. 3)

l [m]	Wall temperatures [K]						
-0.20	300	300	300	300	300	300	300
0.095	841	1029	1203	1365	1518	1698	1829
0.175	870	1071	1236	1413	1633	1833	1978
0.255	879	1092	1285	1473	1679	1873	2023
0.295	873	1073	1283	1473	1673	1874	2023
	(873)	(1073)	(1273)	(1473)	(1673)	(1873)	(2023)
0.335	881	1083	1285	1473	1678	1873	2023
0.415	868	1070	1249	1423	1613	1833	1978
0.495	825	1003	1130	1310	1478	-	-
0.80	300	300	300	300	300	300	300

l – the reactor coordinate; Numbers in parentheses are maximum (target) wall temperatures

Table B. Measured wall temperatures for the ‘up’ temperature profile configuration (Ch. 3)

l [m]	T_{\max} [K] at $x = 0.45$ m	
-0.20	300	300
0.05	982	988
0.15	1062	1138
0.25	1250	1399
0.35	1440	1570
0.45	1473	1673
0.80	300	300

l – the reactor coordinate; At the positions of $x = -0.20$ m and $x = 0.80$ m the room temperatures (300 K) were assumed. In order to make data useable in the CVSSIN program, all reactor positions were shifted by 0.20 m, and the raw data (temperatures vs. position) were smoothed resulting in one hundred data points. Two new positions, necessary for interpolation, were added: $x = -0.05$ m and $x = 1.05$ m and at these positions 300 K are assumed. The ‘down’ temperature profiles were obtained by mirroring the ‘up’ temperature profiles.

Table C. Specific surface area and particle size of TiO₂ powders synthesized using the ‘flat’ temperature profile (Ch. 4)

Sample ID	Temperature [K]	Surf. area [m ² /g]	Crystallite/Particle size* [nm]			
			XRD	TEM	BET	PCS
RD2-33	873	120.6	1.7(0)	5.9(3)	12.8	55.6(6)
RD2-32	1073	289.6	3.4(1)	6.8(3)	5.3	31.8(3)
RD2-36	1273	187.5	5.9(1)	8.9(2)	8.2	28.2(2)
RD2-35	1473	166.1	8.5(1)	13.5(9)	9.3	28.0(3)
RD2-37	1673	158.4	8.9(1)	12.7(2)	9.7	27.2(3)
RD2-27	1873	116.6	10.5(2)	15.8(1)	13.2	31.3(3)
RD2-38	2023	188.9	9.8(2)	17.6(7)	8.2	30.2(3)

*All values for particle size are volume weighted except for those obtained from BET

Table D. Experimental conditions and most relevant experimental results for TiO₂ nanoparticles prepared using the pulsed precursor delivery (Ch. 4)

Sample ID	Laser parameters		Particle size, d [nm]			Geom. stand. dev., σ_g	
	f [kHz]	DC [%]	XRD	TEM	PCS	TEM	PCS
RD-164	1	20	-	5.3(2)	-	1.26(2)	-
RD-183	1	30	7.4(1)	8.4(2)	36.3(9)	1.23(2)	1.39(2)
RD-164	1	40	-	7.1(2)	-	1.29(2)	-
RD-184	1	50	6.7(1)	7.5(2)	33.1(8)	1.20(2)	1.37(2)
RD-164	1	60	-	8.4(2)	-	1.23(2)	-
RD-185	1	70	7.8(1)	8.5(2)	38.1(7)	1.22(2)	1.40(1)
RD-164	1	80	-	8.5(2)	-	1.21(1)	-
RD-186	1	90	8.0(1)	8.0(3)	42.1(7)	1.22(2)	1.39(1)
RD-164	1	100	-	9.2(2)	-	1.25(1)	-
RD2-39	0.2	20	5.6(1)	5.8(1)	22.5(2)	1.24(3)	1.36(1)
RD2-14	0.2	20	-	5.7(1)	-	1.30(3)	-
RD2-14	0.2	40	-	7.6(1)	-	1.23(1)	-
RD2-14	0.2	60	-	8.1(1)	-	1.26(1)	-
RD2-14	0.2	80	-	8.8(1)	-	1.27(1)	-
RD2-14	0.2	100	-	8.6(1)	-	1.25(1)	-
RD-152	0.05	50	-	10.0(2)	-	1.23(2)	-
RD-152	1	50	-	8.2(3)	-	1.23(2)	-
RD-152	3	50	-	8.8(2)	-	1.23(2)	-
RD-152	5	50	-	8.7(2)	-	1.24(2)	-
RD-152	25	50	-	8.9(5)	-	1.25(3)	-

The values for particle size obtained from XRD and PCS are volume weighted, while from TEM are number weighted

Table E. Results of the Rietveld refinement of $\text{Zn}_{1-x}\text{Co}_x\text{O}$ samples (only results for the wurtzite phase are shown) (Ch. 4)

Sample ID	x	d [nm]	ε	Lattice parameters [\AA]		$GofF$
				a	c	
RD-115	0	8.6(1)	0.0088(1)	3.2472(4)	5.211(1)	1.62
RD-93	0.001	10.8(0)	0.0046(1)	3.2517(4)	5.2128(7)	1.51
RD-91	0.005	12.3(0)	0.0041(1)	3.2526(3)	5.2134(6)	1.38
RD-89	0.01	11.6(0)	0.0041(1)	3.2525(4)	5.2120(7)	1.40
RD-90	0.05	18.4(1)	0.0024(0)	3.2532(3)	5.2107(2)	1.24
RD-74	0.10	17.9(2)	0.0028(1)	3.2534(1)	5.2111(6)	1.24
RD-97	0.15	17.0(1)	0.0022(1)	3.2558(3)	5.2116(6)	1.09
RD-106	0.20	18.8(1)	0.0020(0)	3.2576(3)	5.2135(6)	1.11
RD-110	0.25	20.0(1)	0.0023(0)	3.2584(2)	5.2121(4)	1.28
RD-112	0.30	23.2(0)	0.0022(1)	3.2572(2)	5.2098(4)	1.24
RD-111	0.50	14.3(1)	0.0019(1)	3.259(1)	5.214(3)	1.20

x – nominal Co content, d – crystallite size, ε – r.m.s. microstrain, $GofF$ – goodness of fit

Table F. Phase composition and lattice parameters obtained from the Rietveld refinement of $\text{Zn}_{1-x}\text{Co}_x\text{O}$ samples with Co content of $x = 0.30$ and 0.50 (Ch. 4)

Sample ID	x	Phase composition [vol.%]			Lattice parameter, a [\AA]	
		ZnO <i>P63mc</i>	CoO <i>Fm-3m</i>	Co ₃ O ₄ <i>Fd-3m</i>	CoO	Co ₃ O ₄
RD-112	0.30	97.5	2.5(3)	-	4.268(3)	-
RD-111	0.50	25	52(2)	23(2)	4.2704(7)	8.148(4)

List of Publications

1. Djenadic, R., Akgül, G., Attenkofer, K., and Winterer, M., “Chemical Vapor Synthesis and Structural Characterization Of Nanocrystalline $Zn_{1-x}Co_xO$ ($x = 0 - 0.50$) Particles By X-Ray Diffraction And X-Ray Absorption Spectroscopy”, *J. Phys. Chem. C*, **114** (2010) 9207.
2. Djenadic, R., Chowdhury, S. R., Spasova, M., Gondorf, A., Akyildiz, E., and Winterer, M., “Influence of Time-Temperature Profile on Powder Characteristics of Nanocrystalline Anatase (TiO_2) Produced by Chemical Vapor Synthesis”, *Mater. Res. Soc. Sump. Proc.*, **1056** (2008) 1056-HH08-07.
3. Winterer, M., Srdic, V., Djenadic, R., Komph, A., and Weirich, T., “Chemical Vapor Synthesis of Nanocrystalline Perovskites using Laser Flash Evaporation of Low Volatility Precursors”, *Rev. Sci. Instr.*, **78** (2007) 123903.

Curriculum Vitae

Personal Information

Full name: Ruzica Djenadic
Date of birth: December 31, 1976
Place of birth: Sabac, Serbia
Nationality: Serbian
E-mail: ruzica.djenadic@gmail.com

Education

09/2006 - present *Doctoral studies*
Faculty of Engineering, Nanoparticle Process Technology,
University Duisburg-Essen, Germany.

09/2003 - 03/2006 *Postgraduate studies (four semesters)*
Department of Materials Engineering, Faculty of Technology,
University of Novi Sad, Serbia.
Title of master thesis: “Low Temperature Wet-Chemical Syn-
thesis of Lead-Titanate Nanopowders”, supervisor Prof. Dr.
Vladimir V. Srdic

09/1995 - 06/2003 *Undergraduate studies (ten semesters)*
Department of Materials Engineering, Faculty of Technology,
University of Novi Sad, Serbia.
Title of diploma thesis: “Synthesis of Nanocrystalline Stron-
tium-Titanate Powders”, supervisor Prof. Dr. Vladimir V.
Srdic

Professional record

09/2006 – present Research Associate at the Faculty of Engineering, Nanopar-
ticle Process Technology, University Duisburg-Essen, Ger-
many

06/2003 – 09/2006 Research Assistant at the Department of Materials Engineer-
ing, Faculty of Technology, University of Novi Sad, Serbia
